Solution of sign and complex action problems with cluster algorithms

by

Jürgen Cox

Submitted to the Department of Physics
in partial fulfillment of the requirements for the degree of

Doctor of Philosophy

at the

MASSACHUSETTS INSTITUTE OF TECHNOLOGY

March 2001
[June 2001]

Author ..... Jürgen Cox .....
Department of Physics
March 7, 2001

Certified by ..... Uwe-Jens Wiese .....
U.-J. Wiese
Associate Professor of Physics
Thesis Supervisor

Accepted by ..... Thomas J. Greytak .....
Thomas J. Greytak
Associate Department Head for Education

Solution of sign and complex action problems with cluster algorithms

by

Jürgen Cox

Submitted to the Department of Physics
on March 7, 2001, in partial fulfillment of the
requirements for the degree of
Doctor of Philosophy

Abstract

Two kinds of models are considered which have a Boltzmann weight which is either not real or real but not positive and so standard Monte Carlo methods are not applicable. These sign or complex action problems are solved with the help of cluster algorithms. In each case improved estimators for the Boltzmann weight are constructed which are real and positive. The models considered belong to two classes: fermionic and non-fermionic models.

An example for a non-fermionic model is the Potts model approximation to QCD at non-zero baryon density. The three-dimensional three-state Potts model captures the qualitative features of this theory. It has a complex action and so the Boltzmann weight cannot be interpreted as a probability. The complex action problem is solved by using a cluster algorithm. The improved estimator for the complex phase of the Boltzmann factor is real and positive and is used for importance sampling. The first order deconfinement transition line is investigated and the universal behavior at its critical endpoint is studied.

An example for a fermionic model with a sign problem are staggered fermions with 2 flavors in 3+1 dimensions. Here the sign is connected to the permutation sign of fermion world lines and is of nonlocal nature. Cluster flips change the topology of the fermion world lines and they have a well defined effect on the permutation sign independent of the other clusters. The sign problem is solved by suppressing those clusters whose contribution to the partition function and observables of interest would be zero. We confirm that the universal critical behavior of the finite temperature chiral phase transition is the one of the three dimensional Ising model. We also study staggered fermions with one flavor in 2+1 dimensions and confirm that the chiral phase transition then belongs to the universality class of the two dimensional Ising model.

Thesis Supervisor: U.-J. Wiese
Title: Associate Professor of Physics

Acknowledgments

I would like to thank Uwe-Jens Wiese for supervising my thesis and thereby providing me with many insights into very interesting parts of physics. I also would like to thank Mark Alford, Shailesh Chandrasekharan and Kieran Holland for the very enjoyable collaborations on the topics presented in this thesis. Furthermore I thank Jürgen Berges, Jiří Jersák, Thomas Neuhaus and Hendryk Pfeiffer for collaborations on topics unrelated to this thesis. I also thank Oliver Baer, Victor Chudnovsky, Hildegard Cox, Frank Hafner, Fritz Lorenz, my parents, Boris Schlittgen, the sideband, T.A. and everybody who I forgot in this list for being supportive during my american years. Last but not least I thank Selma Zemmouri for her patience.

Contents

Chapter 1

Introduction

Nowadays, the solution to many important problems in physics is obtained numerically using computers. A well known example is nonperturbative quantum chromodynamics (QCD), the theory which is believed to describe the strong interactions [1]. The QCD Lagrangian looks very similar to its abelian counterpart quantum electrodynamics (QED), just that there are eight massless vector bosons — the gluons — instead of one photon and the fermions — the quarks — come in several flavors and three colors. Furthermore there is a direct coupling between the gluons, i.e. they are charged themselves in contrast to photons which are neutral. QED is capable of describing to a very high precision many physical phenomena involving only photons and electrons in agreement with experiment using perturbation theory. In sharp contrast, QCD only grudgingly gives away information about its infrared behavior, which is the flip side of asymptotic freedom. Non-perturbative studies like Monte Carlo simulations of the Euclidean QCD path integral on a space-time lattice (see section 2.2) are needed to gather reliable information about the long-distance physics predicted by QCD. Features like confinement and generation of a mass gap — which are easily obtainable in the strong coupling expansion of the pure gauge lattice theory [2] — can be verified to persist in the continuum limit with the help of Monte Carlo simulations [3, 4]. The static quark-antiquark potential is not Coulomb like as

a perturbative calculation might suggest, but linearly rising with distance, leading to the confinement of quarks into hadrons. The approximate chiral symmetry of the QCD Lagrangian is spontaneously broken in the vacuum. Monte Carlo simulations can reproduce all these features and more. One can study how chiral symmetry gets restored and how quarks and gluons become deconfined and form a plasma at high temperatures [5]. Also hadron masses [6] and meson decay matrix elements [7] can be calculated from first principles. One can check if physical concepts like the dual superconductor picture and monopole condensation are adequate [8] and one can examine the role played by instantons [9].

The situation changes when one is interested in QCD with a nonzero baryon density. The inappropriateness of perturbation theory carries over from the zero baryon density case. Unfortunately the possibility of standard Monte Carlo simulations also ceases to exist and at present no reliable first principles calculations are possible [10, 11]. Responsible for this dilemma is the complex action problem. At nonzero baryon density the Euclidean QCD path integral is not a sum of positive real contributions, but it results from messy cancellations of terms with all possible phases. Therefore the conventional importance sampling methods that make lattice QCD calculations so successful are not applicable any more.

We are trying to find algorithms that even work in the presence of a complex action problem. In this thesis I describe how the problem is solved completely in two toy models. The hope is, of course, to apply our new techniques to solve problems like QCD at nonzero baryon density or the unrelated but equally difficult problem of simulating models of strongly correlated electrons that are believed to capture the physics of high temperature superconductors [12, 13].

Meron cluster algorithms

As has already been stated above, non-perturbative dense QCD can presently not be studied from first principles because Monte Carlo simulations of lattice QCD with non-zero baryon chemical potential μ suffer from a severe complex action problem. The Boltzmann factor in the path integral can then not be interpreted as a probability and standard importance sampling methods fail. In particular, when the μ-dependent part of the Boltzmann factor is included in the measured observables, due to severe cancellations the required statistics is exponentially large in the space-time volume [10, 11]. The complex action problem prevents the numerical simulation of a large class of interesting physical systems including other field theories at non-zero chemical potential or non-zero θ-vacuum angle as well as some fermionic field theories with an odd number of flavors. A special case of the complex action problem is the so-called fermion sign problem which arises for fermionic path integrals formulated in a Fock state basis. The problem is due to paths that correspond to an odd permutation of fermion positions which contribute negatively to the path integral. There are numerous condensed matter systems ranging from the repulsive Hubbard model away from half-filling to antiferromagnetic quantum spin systems in an external magnetic field that cannot be simulated with standard Monte Carlo algorithms. We want to solve these sign or complex action problems with a special kind of cluster algorithm, that has been termed meron-cluster algorithm. Meron-cluster algorithms have been used to solve the sign or complex action problems in several of the cases mentioned above. For example, the first meron-cluster algorithm has led to a solution of the complex action problem in the 2-d $O(3)$ symmetric field theory at non-zero θ-vacuum angle [14]. In this model, some of the clusters are half-instantons, so they are called meron-clusters. The complex action problem also arises in the 2-d $O(3)$ model at non-zero chemical potential. When formulated as a D-theory [15, 16, 17, 18] — i.e. in terms of discrete variables that undergo dimensional reduction — the complex action problem has also been solved with a meron-cluster algorithm [19]. Recently,

the meron concept has been generalized to fermions [20]. Meron-cluster algorithms have led to a complete solution of the fermion sign problem in a variety of models including non-relativistic spinless fermions [20, 21], relativistic staggered fermions [22, 23, 24] (chapter 7) and some models in the Hubbard model family [19, 25].[1] A meron-cluster algorithm has also been used to solve the sign problem that arises for quantum antiferromagnets in an external magnetic field [26]. For a review of these recent developments see [27, 28].

In the conventional formulation of lattice QCD the quarks are represented by Grassmann fields. When the quarks are integrated out, they leave behind a fermion determinant that acts as a non-local effective action for the gluons. At zero chemical potential and for an even number of flavors, the fermion determinant is real and positive and can thus be interpreted as a probability for generating gluon field configurations. Despite the fact that standard importance sampling techniques apply, the non-local nature of the effective gluon action makes lattice QCD simulations with dynamical fermions very time consuming. With a non-zero chemical potential for the baryon number, the fermion determinant becomes complex and standard importance sampling techniques fail completely [10, 11]. This is the reason why non-perturbative QCD at non-zero baryon density can presently not be studied from first principles.

It is natural to ask if a meron-cluster algorithm could be used to solve the complex action problem in QCD. When one integrates out light quarks, one obtains a non-local effective action for the gluons and it appears unlikely that the meron concept will apply. On the other hand, when one describes the quarks in a Fock state basis, the complex action problem is still present, in the form of a fermion sign problem. Our hope is that this problem will eventually be solved by a meron-cluster algorithm applied to the D-theory formulation of QCD [15, 16, 17, 18], since the quark and gluon degrees of freedom are then discrete and should be easier to handle. In this thesis, two simpler problems are adressed first, which are described in the following.

[1] The models investigated so far only show s-wave superconductivity.

The first model we discuss is the 3-d 3 state Potts model approximation to QCD with very heavy quarks at finite baryon density. It is a purely bosonic model which has a complex action problem. The second model focuses on a very different feature of the problem. It is a purely fermionic model with a four fermion interaction. It has a severe sign problem as well due to the Pauli exclusion principle which assigns configurations of fermion world lines positive or negative weights depending on their topology. The complex action problem in QCD can be thought of as a combination of the two complex action/sign problems that are here solved seperately in the two toy models.

Potts model approximation to dense QCD

We first consider QCD in the limit of very heavy quarks with a large chemical potential. These can be integrated out, introducing Polyakov loops into the effective gluon action. When quarks are integrated out at non-zero chemical potential μ we expect a complex action, and in this case it arises because a Polyakov loop Φ and its charge conjugate Φ^* get different weights when $\mu \neq 0$.

Polyakov loops are only non-local in the Euclidean time direction, so this effective gluon action is more manageable than the one that arises for a general fermion determinant. Indeed, Blum, Hetrick and Toussaint have simulated the theory in this form on lattices of moderate size where the complex action problem is less severe [29]. Recently, Engels, Kaczmarek, Karsch and Laermann have studied QCD with heavy quarks at fixed baryon number. Again, for moderate baryon density and moderate volumes the complex action problem is not too severe and simulations are possible [30]. Ultimately one would like to be able to solve the complex action problem for this gluon action completely. At the moment, we still cannot apply a meron-cluster algorithm to solve the problem, because the construction of efficient cluster algorithms for non-Abelian gauge theories seems to be impossible for Wilson's formulation of

lattice field theory. Here we will simplify the problem further by replacing the gauge dynamics by that of the $\mathbf{Z}(3)$ Potts model representing the Polyakov loops [31, 32]. We have found a cluster algorithm that solves this complex action problem in the Potts model approximation to QCD.

Chiral phase transitions in staggered fermion models

Next we consider the purely fermionic aspect of the sign problem. The numerical simulation of lattice fermions is a notoriously difficult problem which is the major stumbling block in solving QCD and other fermionic field theories. The standard method is to integrate out the fermions and to simulate the resulting bosonic problem with a non-local action. In several cases of physical interest — for example, for QCD with an odd number of flavors or with non-zero chemical potential — the bosonic Boltzmann factor may become negative or even complex and thus cannot be interpreted as a probability. When the sign or the complex phase of the Boltzmann factor is included in measured observables, the numerical simulation suffers from severe cancellations resulting in a sign problem. The standard fermion algorithms are incapable of exploring such models. As a consequence, QCD is usually simulated with an even number of flavors and at zero chemical potential. Even in the absence of a sign problem, the simulation of fermions is difficult. For example, lattice QCD simulations suffer from critical slowing down when one approaches the chiral limit in which the quarks become massless. In particular, this makes it difficult to identify the universality class of the finite temperature QCD chiral phase transition.

Even in the simpler models with four-fermion interactions that are considered here, the identification of the finite temperature critical behavior is a non-trivial issue [33]. A model with N fermion flavors shows mean-field behavior in the $N = \infty$ limit. On the other hand, at finite N one finds the non-trivial critical behavior that one

expects based on dimensional reduction and standard universality arguments. For example, in [34] it has been verified that the chiral phase transition in a $(2+1)$-d four-fermion model with $N = 4$ and $\mathbf{Z}(2)$ chiral symmetry is in the universality class of the 2-d Ising model. Due to the fermion sign problem, standard fermion simulation methods often do not work in models with a too small number of flavors.

We apply the meron-cluster technique [20] for solving the sign problem to a (3+1)-d model of staggered fermions using the Hamiltonian formulation. The model has $N = 2$ flavors and a $\mathbf{Z}(2)$ chiral symmetry that is spontaneously broken at low temperatures. The fermion determinant can be negative in this model. Hence, due to the sign problem standard fermion algorithms fail in this case. Our algorithm is the only numerical method available to simulate this model. In this method we do not integrate out the fermions but describe them in a Fock state basis. The resulting bosonic model of fermion occupation numbers interacts locally, but has a non-local fermion permutation sign resulting from the Pauli exclusion principle. Standard numerical methods would suffer from severe cancellations of positive and negative contributions to the partition function. Like other cluster methods, our algorithm decomposes a configuration of fermion occupation numbers into clusters which can be flipped independently. Under a cluster flip an occupied site becomes empty and vice versa. The main idea of the meron-cluster algorithm is to construct the clusters such that they affect the fermion sign independent of each other when they are flipped. In addition, it must always be possible to flip the clusters into a reference configuration with a positive sign. A cluster whose flip changes the fermion sign is referred to as a meron because it can be viewed as a half-instanton. If a configuration contains a meron-cluster, its contribution to the partition function is canceled by the contribution of the configuration that one obtains when the meron-cluster is flipped. The observables that we consider get non-zero contributions from the zero- and two-meron sectors only. Our algorithm ensures that configurations with more than two merons are never generated, which leads to an exponential gain

in statistics and to a complete solution of the sign problem.

Like other cluster algorithms the meron algorithm substantially reduces critical slowing down. This allows us to work directly in the chiral limit. As a result, we can study the nature of the chiral phase transition in great detail. The $\mathbf{Z}(2)$ chiral symmetry is spontaneously broken at low temperatures and gets restored in the high-temperature phase. As expected, the system close to the finite temperature critical point is in the universality class of the 3-d Ising model. We verify this in a high-precision finite-size scaling investigation of the chiral susceptibility.

We also apply the meron-cluster algorithm to the same staggered fermion model in 2+1 dimensions with $N = 1$ flavor. It has a severe sign problem too and cannot be explored using standard algorithms. More complicated observables than in the (3+1) dimensional case are constructed that require the exploration of the four-meron sector. We find that the $\mathbf{Z}(2)$ chiral symmetry of this model is spontaneously broken at low temperatures and that the finite-temperature chiral phase transition is in the universality class of the 2-d Ising model, as expected from dimensional reduction arguments.

Outline

In chapter 2, I describe the most important physical example, that motivates our search for a solution of complex action problems — finite density QCD — in more detail. The present understanding of the temperature density phase diagram is summarized. Then the formulation on a space-time lattice is introduced and it is pointed out that its Monte Carlo simulations are plagued by the complex action problem. Chapters 3 to 6 deal with the Potts model approximation to dense QCD. In chapter 3 the limit of heavy quarks is considered and its relation to the 3-d 3 state Potts model is elucidated. The Potts model approximation still has a complex action problem. In chapter 4 the complex action problem of the Potts model approximation to finite

density QCD is solved by a cluster algorithm. Improved estimators for physical quantities are constructed. Chapter 5 contains the derivation of the flux representation of the Potts model and a description of a Metropolis algorithm to simulate it. A comparison of the Metropolis algorithm for the flux model and the cluster algorithm for the original Potts model shows that the latter is more efficient. In chapter 6, we present the physical results concerning the critical endpoint E in the phase diagram of the Potts model. Using finite-size scaling techniques, we are able to determine the position of the critical endpoint of the deconfinement phase transition to high accuracy. Our results are consistent with the expected universal 3-d Ising behavior. In chapter 7, a different aspect of the complex action problem is considered. We study a purely fermionic model of staggered fermions which suffers from a severe sign problem. Here the sign problem is connected to a permutation sign of the fermion world lines and is of nonlocal nature. It is again solved by a meron cluster algorithm. We perform simulations of the 3+1 dimensional models and confirm that the universal critical behavior of the finite temperature chiral phase transition is 3-d-Ising like. We also study the same model in 2+1 dimensions and again it is confirmed by numerical simulations that the chiral phase transition is in the universality class of the 2-d Ising model. Hence in both cases the scenario that universal properties are determined by the dimensionally reduced scalar field theory for the order parameter, are confirmed. Finally, chapter 8 contains a summary and conclusions. Much of the content of this thesis has been published in [22, 19, 23, 35].

Chapter 2

QCD at finite temperature and baryon density

QCD under extreme conditions, like high temperatures and baryon densities has applications in cosmology [36, 37], astrophysics of neutron stars [38, 39], and heavy ion collisions [40]. While the cosmological interest focuses on high temperatures and rather low densities, the other two examples can be located in the intermediate to high baryon density regime. In a Euclidean formulation a non-zero temperature leads to a finite Euclidean time extent, which is proportional to the inverse temperature $\beta = 1/T$. A finite baryon density is conveniently implemented with the help of a chemical potential μ for baryon number. The thermodynamics of QCD in thermal and chemical equilibrium is determined by the grand canonical partition function

$$Z_{\mathrm{QCD}}(T,\mu) = \int \mathcal{D}\bar{\psi}\,\mathcal{D}\psi\,\mathcal{D}A_a^\mu\,\exp\left(-\int_0^\beta \mathrm{d}\tau \int \mathrm{d}^3x\,(\mathcal{L}_{\mathrm{QCD}} - \mu\sum_f \bar{\psi}_f\gamma^0\psi_f)\right) \quad (2.1)$$

(see e.g. [41]). Here $\mathcal{L}_{\mathrm{QCD}}$ is the Euclidean version of the QCD Lagrangian

$$\mathcal{L}_{\mathrm{QCD}} = \sum_f \bar{\Psi}_f(\not{D} + m_f)\Psi_f + \frac{1}{4}F^a_{\mu\nu}F_a^{\mu\nu}, \quad (2.2)$$

where

$$F_a^{\mu\nu} = \partial^\mu A_a^\nu - \partial^\nu A_a^\mu - g f_{abc} A_b^\mu A_c^\nu \quad \text{and} \quad \not{D} = \gamma_\mu(\partial^\mu + ig\lambda_a A_a^\mu). \tag{2.3}$$

For the path integral to make sense in a continuous space-time one would have to fix the gauge and introduce Faddeev-Popov ghost degrees of freedom [42]. As the lattice formulation, which will be the focus of this thesis, does need neither gauge fixing nor ghosts, these concepts will not be introduced here. The lattice formulation is discussed in more detail in section 2.2. There it will be seen that for $\mu \neq 0$ the partition function (2.1) can not be simulated with standard importance sampling techniques. As perturbative treatment is reliable only in extreme limiting cases of very high temperature or very high densities, this implies that with today's methods there is no way to gather reliable information about QCD at finite density from first principles.

Of course the lack of first principles methods at nonzero μ does not stop physicists from thinking about how matter might behave under these conditions. (For a recent review of the current understanding of QCD at large baryon density see [43].) The consideration of toy models and semi-rigorous arguments at asymptotically large densities have already led to a detailed picture of how the phase diagram in the μ-T-plane might look like. One expectation is the existence of at least one kind of new phase at high densities and low temperatures where the $SU(3)$ color gauge symmetry is either partially or completely spontaneously broken. This phenomenon has been termed color superconductivity. Furthermore, a phase with a novel kind of chiral symmetry breaking might exist at high densities, where color and flavor degrees of freedom are spontaneously locked together. However this phase could be analytically connected to the low density phase. A first principles confirmation of the existence of these new phases and of the topology of the phase diagram can only come from lattice simulations. Also there is no other way to systematically calculate the exact positions of the transition lines and critical points or to check the universality hypotheses at critical or tricritical points in the phase diagram. That is why it is vitally important

to find ways to overcome the complex action problem.

In the next section the current understanding of the phase diagram is summarized. Then the lattice formulation is briefly described and the presence of a complex action problem is pointed out. Finally some comments on the standard dimensional reduction arguments for finite temperature phase transitions are made.

2.1 The conjectured phase diagram

First, we consider the case of zero baryon density. At low temperatures, the physics is dominated by the vacuum properties of QCD. Quarks and gluons are confined into hadrons and the approximate chiral symmetry is spontaneously broken. At a temperature of about 150 MeV qualitative changes are expected to take place. Quarks and gluons are no longer confined into hadrons but can be excited independently. Also the approximate chiral symmetry gets restored. Both these changes in the properties of matter — despite the fact that they might be quite drastic — are most likely no phase transitions in nature.

It is interesting to consider the quark masses as variables and not to fix them to their actual values. Only the three lightest quarks have to be considered, since the others are too heavy to contribute significantly to the dynamics. The u- and d-quark masses are assumed to be equal to each other. The following limiting cases are especially interesting:

- $m_{ud} = m_s = 0$

  There is an $SU(3)_L \times SU(3)_R$ chiral symmetry and a $U(1)_B$ symmetry related to baryon number conservation. At low temperatures this symmetry is spontaneously broken to the subgroup $SU(3)_{L=R} \times U(1)_B$. There has to be a phase transition between the low temperature phase with broken chiral symmetry and the high temperature with restored chiral symmetry, since the chiral condensate is an order parameter, being zero in the high temperature phase and nonzero

in the low temperature phase.

- $m_{ud} = 0$, $m_s > 0$

  The chiral symmetry group is only $SU(2)_L \times SU(2)_R$. In addition to $U(1)_B$ there is $U(1)_S$ related to strangeness conservation. The chiral symmetry group is again spontaneously broken to the diagonal subgroup $SU(2)_{L=R}$ at low temperatures. Again the two phases have to be separated by a phase transition.

- $m_{ud} = m_s = \infty$

  This is as if there were no fermions. There is no chiral symmetry, but there is a $\mathbb{Z}(3)$ center symmetry. The pure Yang-Mills action at finite temperature is invariant under gauge transformations that are periodic in Euclidean time up to an element of the center $\mathbb{Z}(3)$ of the gauge group $SU(3)$. This center symmetry is spontaneously broken at high temperatures. An order parameter for the breaking of the center symmetry is the Polyakov loop expectation value

$$\langle \Phi \rangle = \langle \mathrm{Tr}[\mathcal{P} \exp(-\int_0^\beta dt\ A_4(\vec{x}, t))] \rangle. \tag{2.4}$$

For each value of m_{ud} and m_s one can now ask if the transition at nonzero temperature (but zero chemical potential) is first order, second order, or just a crossover, i.e. not really a phase transition but a rapid but analytic change of properties. This question is answered in figure 2-1. Let us first consider the upper left corner, where $m_{ud} = 0$ and $m_s = \infty$. There has to be a phase transition, since the chiral condensate is an order parameter distinguishing between the phases. The order of the phase transition and, its universality class in the case of a second order transition can be estimated by the argument presented in [45]. Universal properties of a finite temperature phase transition can be calculated in a dimensionally reduced (i.e. 3-dimensional) σ model with the same global symmetries. The transition region is dominated by the longitudinal and transverse fluctuations of the order parameter. Being bosonic, they have zero modes in their finite temperature Matsubara decom-

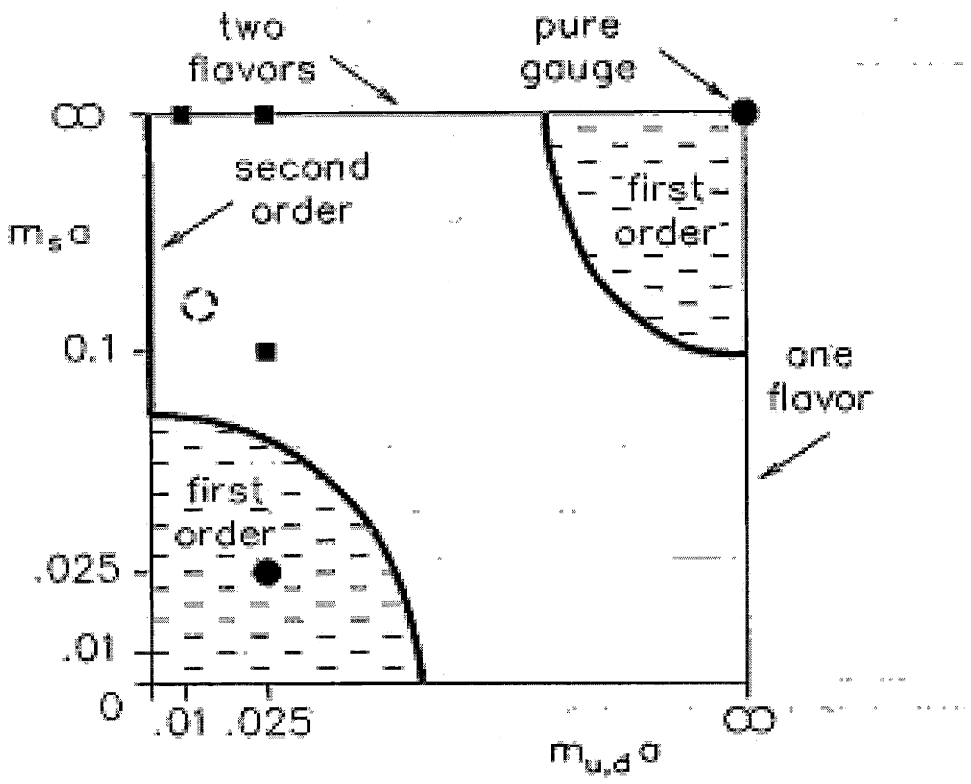

Figure 2-1: *Presence and absence of the finite-temperature QCD phase transition as a function of m_{ud} and m_s. The physical point, indicated roughly by the dashed circle, is suspected to lie in the region of no transition. From [44].*

position. These zero modes are the only relevant degrees of freedom in the scaling region and at low energies the higher Matsubara modes decouple. Therefore the finite temperature phase transition of a (3+1)-dimensional theory is described by a 3-dimensional scalar theory with the same global symmetries. In the case considered the symmetry breaking pattern is $O(4) = SU(2)_L \times SU(2)_R \longrightarrow SU(2)_{L=R} = O(3)$, which is identical with the symmetry breaking pattern of the $O(4)$ σ model. Hence, if the the finite temperature phase transition is second order, it is expected to be in the 3-d $O(4)$ universality class. Lattice simulations of QCD with two flavors [59] are consistent with a second order transition and 3-d $O(4)$ critical behaviour, however more precise numerical studies are necessary to reach a satisfactory level of confidence

and to determine the critical exponents with sufficient precision.

Now let us consider the lower left corner in figure 2-1, where all three quarks are massless. According to the discussion above, one should consult here the 3-d σ model with the symmetry breaking pattern $SU(3)_L \times SU(3)_R \longrightarrow SU(3)_{L=R}$. It turns out that this model has a first order phase transition [45] and therefore we expect the finite temperature phase transition of QCD in this case to be first order, too. Since the transition is expected to be first order for $m_s = 0$ and second order for $m_s = \infty$, the order of the transition should change in between. The first order region extends into the $m_{ud} > 0$ region while the second order $O(4)$ transition exists only for $m_{ud} = 0$.

Now we focus on the upper right corner of figure 2-1, i.e. pure gauge theory. Here the symmetry that gets spontaneously broken at the finite temperature phase transition is the $Z(3)$ center of the $SU(3)$ gauge group, which signals the absence or presence of confinement. Applying the same arguments as before, the finite temperature phase transition of QCD should be described by the 3-d 3-state Potts model [46], which has a first order transition [82]. Indeed, these expectations have been confirmed by QCD simulations of the pure $SU(3)$ gauge theory [47, 48, 49].

In reality, the quark masses are not equal to any of the special cases considered above. The u- and d-quark masses are nearly but not exactly zero and the s-quark mass is on the scale of Λ_{QCD}, i.e. neither light nor heavy. Due to the nonzeroness of the quark masses, there is no rigorous distinction between the regions of intact and spontaneously broken chiral symmetry. On the other hand, the presence of light quarks, which can break the confining string between two test charges, implies the absence of an order parameter for confinement. Therefore, for realistic quark masses there does not have to be a transition at all but there could be just a smooth crossover. This is most likely what happens. The physical point in figure 2-1 (indicated roughly by the dashed circle) lies most likely in the region of no transition [44].

What happens at nonzero baryon density depends even more on the number of quark flavors and their masses. To understand what happens for realistic quark

masses it is again instructive to first consider some "unrealistic" limiting cases. As the u and d quarks are light compared to the fundamental QCD scale Λ_{QCD}, it is a good first approximation to set $m_u = m_d = 0$. The strange quark mass is unfortunately on the order of Λ_{QCD} and it is not a priori clear if nature behaves as if there were two or rather three light flavors. To get a better understanding of the subject we consider some special cases. First we consider two massless quarks and the strange quark being infinitely heavy. Then we take into account the small nonzero masses of the u and d quarks but leave the strange quark infinite. Then the strange quark mass is lowered.

$m_{ud} = 0,\ m_s = \infty$ (Fig. 2-2 a)

As the u and d quarks are assumed to be massless, there is a chiral phase transition and not merely a crossover at $\mu = 0$. As discussed before, it is believed to be of second order and in the universality class of the three dimensional $O(4)$ model [45, 50, 51]. The transition continues into the phase diagram for $\mu > 0$ and at a tricritical point it changes from second to first order [52]. At large μ and low temperatures is the color superconducting phase (2SC) [53, 54, 55, 56]. Here, the $SU(3)$ color gauge symmetry is spontaneously broken to an $SU(2)$ subgroup, giving mass to five of the eight gluons by the Higgs mechanism. No global symmetries are spontaneously broken in this phase. In particular the $SU(2)_L \times SU(2)_R$ chiral symmetry is intact as well as the $U(1)$ baryon number symmetry.

$m_{ud} \neq 0,\ m_s = \infty$ (Fig. 2-2 b)

The u and d quarks are not really massless but only very light. As a consequence, the chiral transition at $\mu = 0$ is merely a crossover, which is consistent with current lattice simulations [5, 57, 58, 59]. Thus, the phase diagram looks more like in Fig. 2-2 b. The second order transition line disappears and the tricritical point is replaced by a critical endpoint.

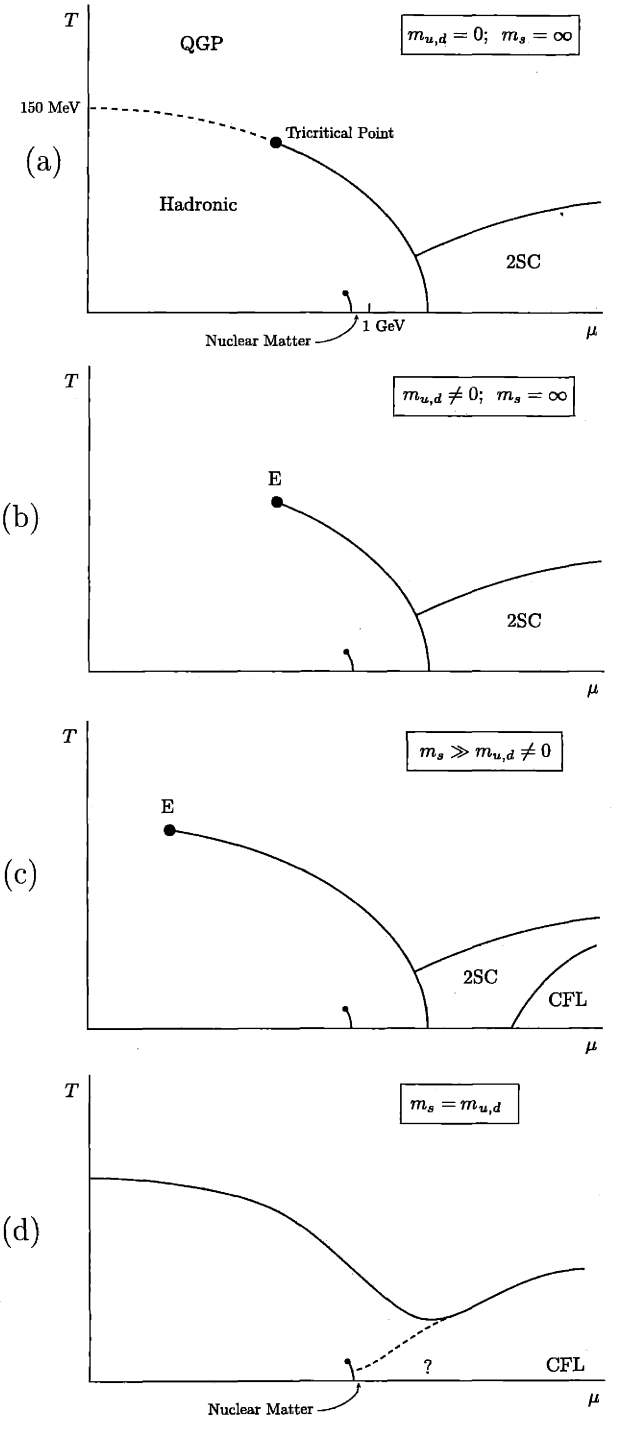

Figure 2-2: *QCD phase diagram for four different values of the quark masses. From [43].*

$m_s \gg m_{ud} \neq 0$ (Fig. 2-2 c)

If the s quark mass is lowered towards a realistic value, a new superconducting phase with color-flavor locking (CFL) [60] emerges at sufficiently high densities. If the three quark flavors were massless, then in the CFL phase the symmetry group $SU(3)_{\text{color}} \times SU(3)_{\text{L}} \times SU(3)_{\text{R}} \times U(1)_{\text{B}}$ is spontaneously broken to the global subgroup $SU(3)_{\text{color+L+R}} \times Z_2$. So the gauge symmetry is completely broken, giving all eight gluons a mass and also chiral symmetry is broken. In addition to that also the baryon number symmetry is broken to a discrete subgroup Z_2. If $\mu \gg m_s$, the quarks appear light enough so that a transition to the CFL phase can occur.

$m_s = m_{ud}$ (Fig. 2-2 d)

Finally, if the strange quark mass is lowered even further to the order of the u and d quark masses, then the region of CFL and the baryonic phase might be analytically connected. Furthermore, the transition at $\mu = 0$ is first order.

$m_s = m_{ud} = \infty$

This is the case studied in chapters 3 to 6. As explained before, at zero chemical potential the Z(3) center symmetry properties determine the nature of the phase transition and the 3-d 3 state Potts model describes the physics very well. The deconfining transition at nonzero temperature is first order. The phase diagram at nonzero chemical potential is shown in figure 3-1. The first order deconfining transition continues into the region of $\mu > 0$ and terminates in a critical endpoint. The position and critical properties of this point are determined in the Potts model approximation in chapter 6.

Nature's quark masses

Fig. 2-2 b to d are a sequence of decreasing strange quark masses. Starting from an infinitely heavy strange quark and decreasing the mass moves the endpoint E further to the left until it arrives at some critical mass value at the T axis. Also the CFL phase begins to emerge and finally completely displaces the 2SC phase at low enough strange quark mass. Nature is somewhere between b and d and there is a slight preference among experts for c being the real phase diagram. An improvement of lattice techniques is urgently needed to get a definite answer to that question.

2.2 Lattice formulation

A very important framework for the understanding of gauge theories is their lattice formulation [2, 61, 62, 63]. It is especially important for QCD, because of the strong coupling. Lattice gauge theory is a regularization scheme that replaces the continuous space-time by a regular lattice, most conveniently a hyper-cubic lattice with a lattice spacing a.

Gauge symmetry

While Lorentz symmetry gets broken by this regularization and gets restored only in the continuum limit, gauge symmetry is exactly preserved. However, the gauge group on the lattice is in some sense smaller than in the continuum, since gauge transformations are only done on a discrete set of lattice points. On a finite lattice with N points the QCD gauge group is therefore the finite dimensional Lie group $SU(3)^N$, while in the continuum the gauge group would be something like $SU(3)^{\text{uncountable infinity}}$.

The quark fields ψ_x live on the sites of the lattice, while the basic gauge degrees of freedom are the parallel transporters $U_{x,\mu} \in SU(3)$ on the links between two neighboring lattice sites with coordinates x and $x + a\hat{\mu}$. A local gauge transformation Λ_x is an $SU(3)$ transformation matrix defined on each lattice point x and it acts on

the fermion and gauge field like

$$\psi_x \longrightarrow \psi'_x = \Lambda_x \psi_x, \tag{2.5}$$

$$\bar{\psi}_x \longrightarrow \bar{\psi}'_x = \bar{\psi}_x \Lambda_x^{-1}, \tag{2.6}$$

$$U_{x,\mu} \longrightarrow U'_{x,\mu} = \Lambda_x U_{x,\mu} \Lambda^{-1}_{x+a\hat{\mu}}. \tag{2.7}$$

The link variables $U_{x,\mu}$ have the same transformation property as a Wilson line in the continuum formulation, i.e. it gets multiplied by the gauge function at the ends of the link. That implies that the trace of a product of link variables along a closed path of links is a gauge invariant object. The shortest closed paths on the lattice are the plaquettes consisting of four links forming a square. The parallel transporter along such a plaquette $p = (x, \mu, \nu)$

$$U_p = U_{x,\mu} U_{x+a\hat{\mu},nu} U^{-1}_{x+a\hat{\nu},mu} U^{-1}_{x,\nu} \tag{2.8}$$

is used in the Wilson action for the gauge field. It is given by the sum over all plaquettes p of the real part of the trace of U_p

$$S_g[U] = \sum_p \beta \left(1 - \frac{1}{3} \mathrm{ReTr} U_p\right). \tag{2.9}$$

Among other pleasant features, it becomes equal to the continuum Yang-Mills action in the classical continuum limit of the action with $\beta = 6/g^2$. The universality hypothesis implies that there are many other lattice actions that one could choose for the gauge fields without changing the continuum limit, as long as it is in some sense local and has the same symmetry properties. Equation (2.9) is just the simplest possible choice. There is a lot of research effort focussed on the question how one can get closer to the continuum limit without increasing the computing effort much but just choosing the lattice action in a clever way [64, 65, 66, 67].

Wilson fermions

The lattice regularization of fermions is unfortunately not as straightforward as it is for gauge or scalar fields. A simple discretization of the continuum fermion action leads to the doubling problem [68]. Instead of only one fermion flavor one has 15 additional doublers after naive discretization. They can be associated with the 16 corners of the Brillouin zone of Euclidean four-momentum space. There are two standard ways to deal with this problem which go under the names of Wilson fermions and staggered fermions. In the case of Wilson fermions [69] one adds a term to the action that gives higher masses to the fermion doublers, so that they completely decouple in the continuum limit. Unfortunately, to achieve that one has to explicitly break chiral symmetry, which has to be restored by a fine tuning procedure. In principle one could reduce the number of flavors to one with this method. Nevertheless, in order to use standard importance sampling methods one needs an even number of degenerate flavors to insure that after integrating out the fermions the effective gluon action is nonnegative.

Staggered fermions

Another way to deal with the fermion doubling problem is the staggered fermion method [70, 71, 72]. Here the extra fermions are interpreted as physical flavors. The replication can be reduced from 16 to 4 by assigning only a single fermion field component instead of four to every lattice site. The action has the particularly simple form

$$\frac{1}{2}\sum_{x,\mu}\eta_{x,\mu}(\bar{\chi}_x\chi_{x+a\hat{\mu}}-\bar{\chi}_x\chi_{x-a\hat{\mu}})+m\sum_x\bar{\chi}_x\chi_x, \tag{2.10}$$

where the Grassmann field χ has only one component instead of four. Staggered fermions have the pleasant feature that for $m = 0$ they have a $U(1) \times U(1)$ chiral symmetry even at nonzero lattice spacing which makes them very suitable for toy models of chiral symmetry breaking. A disadvantage is that in the Euclidean for-

mulation it describes four degenerate flavors in the continuum limit. As we will see in chapter 7, in the Hamiltonian formulation the minimal number of flavors in the continuum limit is two. However, when reformulated as a path integral, there is a sign problem as the Boltzmann weight is not positive definite. We are able to solve this sign problem with a meron-cluster algorithm and simulate the finite temperature chiral phase transition in a Gross-Neveu model with staggered fermions, as will be described in chapter 7.

Chiral symmetry on the lattice

The two implementations of fermions on a lattice described above have some shortcomings concerning chiral symmetry. While for Wilson fermions, chiral symmetry is completely broken at nonzero lattice spacing, for staggered fermions there is at least a $U(1) \times U(1)$ subgroup of the $SU(4) \times SU(4) \times U(1)$ chiral symmetry of the continuum theory intact at nonzero lattice spacing. This does not mean that chiral symmetry is fundamentally incompatible with a lattice regularization. In fact, recent research has proved this old belief wrong [73]. One way to have chiral symmetry on a lattice is to introduce a fictitious fifth dimension. The chiral fermions live on domain walls in this fifth direction. Another way to insure chiral symmetry is to impose the so-called Ginsparg-Wilson relation on the Dirac operator. Both of these methods have a significant computational overhead compared to simple Wilson or staggered fermions, which make them still somewhat impractical for actual calculations. But they show that there is no fundamental incompatibility between chiral symmetry and lattice regularization.

The sign problem in lattice QCD

The path integral on a Euclidean space-time lattice is

$$Z = \int \mathcal{D}\bar{\Psi}\,\mathcal{D}\Psi\,\mathcal{D}U\, e^{-S_f[\bar{\Psi},\Psi,U]-S_g[U]} \tag{2.11}$$

$$= \int \mathcal{D}U\ \det M[U] e^{-S_g[U]}. \tag{2.12}$$

To be specific we represent quarks with Wilson fermions

$$S_f = \sum_x \bar{\Psi} M \Psi, \quad M = \gamma^\mu D_\mu + rD^2 + m + \mu\gamma_0, \tag{2.13}$$

and $S_g[U]$ is the usual plaquette action for the gauge field. Monte Carlo simulations are usually done with the expression (2.12) where fermions are integrated out and a nonlocal effective action for the gluon field remains. To use conventional importance sampling techniques, it is necessary for the integrand to be nonnegative, so that it can be interpreted as a probability. So the fermion determinant $\det M$ must be nonnegative for any gauge configuration. One way to insure this is to have an even number of degenerate fermion flavors and to have $\det M \in \mathbb{R}$. It turns out that the fermion determinant is guaranteed to be real only if $\mu = 0$. That means at nonzero μ there is a complex action problem and the QCD partition function can not be simulated with standard Monte Carlo methods. (For a more detailed discussion of the general nature of the complex action problem see section 4.1.) If staggered fermions were used, even four degenerate flavors would be needed to ensure the positiveness of the Boltzmann weight. In summary, for the QCD partition function to be tractable with standard importance sampling methods, the following conditions have to be fulfilled:

- $\mu = 0$
- an even number of degenerate flavors if Wilson fermions are used

- a multiple of four degenerate flavors if staggered fermions are used.

Obviously these restrictions have to be overcome if realistic quark masses should be used or if one is interested in a finite baryon density. In this thesis these restrictions will be lifted for two vastly simplified versions of QCD. First we solve the complex action problem in a Potts model approximation to QCD at nonzero baryon density with very heavy quarks (see chapter 4). Then we solve the sign problem in a a toy model with only quarks, namely staggered fermions with two flavors (see chapter 7).

2.3 Remarks on dimensional reduction

In the discussion of the QCD phase diagram at finite temperature and baryon density, one often uses dimensional reduction arguments to predict properties of phase transitions. One infers universal properties of a finite temperature phase transition from the dimensionally reduced scalar field theory for the order parameter field [45]. While it is often hard to predict the order of a phase transition from such arguments [45], the universality hypothesis implies that if the transition is second order, the universal properties of the finite temperature phase transition and the dimensionally reduced theory for the order parameter should coincide. This standard scenario had been challenged recently [74] by an observation in the large N limit of the the Gross-Neveu model in (2+1) dimensions, which is studied in this thesis with $N = 1$ flavors. It has been found that the phase transition in the large N limit is second order, but that the critical exponents are not 2-d Ising like, as would be predicted by the standard dimensional reduction scenario, but that they are mean field like. This odd behaviour seems to exist only for $N = \infty$ but for any finite N the standard scenario is recovered [33]. Therefore this counterexample could be attributed to the peculiarity of the large N limit. For example in QCD in two dimensions in the limit of infinitely many colors, even the Mermin-Wagner theorem can be violated.

The history of the supposedly simple (2+1) dimensional Gross-Neveu model also

shows how inefficient standard fermion algorithms are. While the behavior for $N \to \infty$ can be obtained analytically, for finite N one relies on Monte Carlo simulations. In the first numerical studies with a standard hybrid Monte Carlo algorithm for the fermions, it was concluded that the leading large N behaviour is probably valid at least up to N as small as 4 [75]. (Smaller N could not be simulated due to the sign problem.) Only in later large scale studies [33] it was possible to find Ising-behaviour for finite N and account the leading large N behaviour to a narrowing of the Ginsburg region in the large N limit. In the studies using a meron cluster algorithm, whose results are presented in chapter 7 we find the Ising behaviour for the model with $N = 1$ flavor with only modest computing effort.

Chapter 3

The Potts model approximation to dense QCD

We consider QCD with static quarks coupled to a large chemical potential. This leaves us with an $SU(3)$ Yang-Mills theory with a complex action containing the Polyakov loop. Close to the deconfinement phase transition the qualitative features of this theory, in particular its $\mathbf{Z}(3)$ symmetry properties, are captured by the 3-d 3-state Potts model. In chapter 4, we solve the complex action problem in the Potts model by using a cluster algorithm. The improved estimator for the μ-dependent part of the Boltzmann factor is real and positive and is used for importance sampling. In chapter 6, we localize the critical endpoint of the first order deconfinement phase transition line and find consistency with universal 3-d Ising behavior. We also calculate the static quark-quark, quark-anti-quark, and anti-quark-anti-quark potentials which show screening as expected for a system with non-zero baryon density.

The 3-d $\mathbf{Z}(3)$-symmetric Potts model has often been used as an approximation to QCD with static quarks. In particular, the phase transition to a broken $\mathbf{Z}(3)$ symmetry phase at high temperature corresponds to the first order deconfining phase transition in QCD. As has been noted by Condella and DeTar, a term that corresponds to a chemical potential can also be included in the Potts model, explicitly

breaking the $\mathbf{Z}(3)$ symmetry [76]. As the coefficient of this term grows, the first order deconfinement phase transition persists but it becomes weaker and ultimately disappears in a critical endpoint. This point is expected to be in the universality class of the 3-d Ising model. In this thesis this expectation will be confirmed with numerical simulations.

In principle, one can imagine deriving an effective 3-d 3-state Potts model directly from QCD by integrating out all degrees of freedom except for the $\mathbf{Z}(3)$ phase of the Polyakov loop. However, the resulting Potts model action would be very complicated and cannot be derived in practice, except in the strong coupling limit. Here we approximate QCD with heavy quarks by a 3-d $\mathbf{Z}(3)$-symmetric Potts model with a standard nearest-neighbor interaction. Universal features like the nature of the critical endpoint of the deconfinement phase transition are correctly reproduced in this approximation. Figure 3-1 contains the phase diagram of the 3-d 3-state Potts model in the (h, κ)-plane. The parameter h represents $\exp(\beta(\mu - M))$ in QCD with quarks of mass M at chemical potential μ. We study the limit $M, \mu \to \infty$ for any given $\mu - M$. Large h corresponds to $\mu > M$ and small h to $\mu < M$. Because $\mu - M \ll M, \mu$ we are always, for any h, in the immediate neighborhood of the onset of non-zero density for the heavy quarks. This means that it does not matter whether they are fermions or bosons, since they never move. The difference would only become apparent above the onset, where either a Fermi surface or a degenerate Bose gas would occur, and our order of limits is such that we never get that far from the onset. The parameter κ is the standard Potts model coupling, which corresponds roughly to the temperature $T = 1/\beta$. The ordinary first-order deconfinement phase transition at $h = 0$ (point T in Figure 3-1) extends into a line of first order transitions that terminates in the critical endpoint E. This endpoint occurs at such a low value of h that the complex action problem is not very severe there, and we found that the most efficient way to locate and study it was to employ a reweighted Metropolis algorithm, which can in this case be applied at volumes large enough to show the

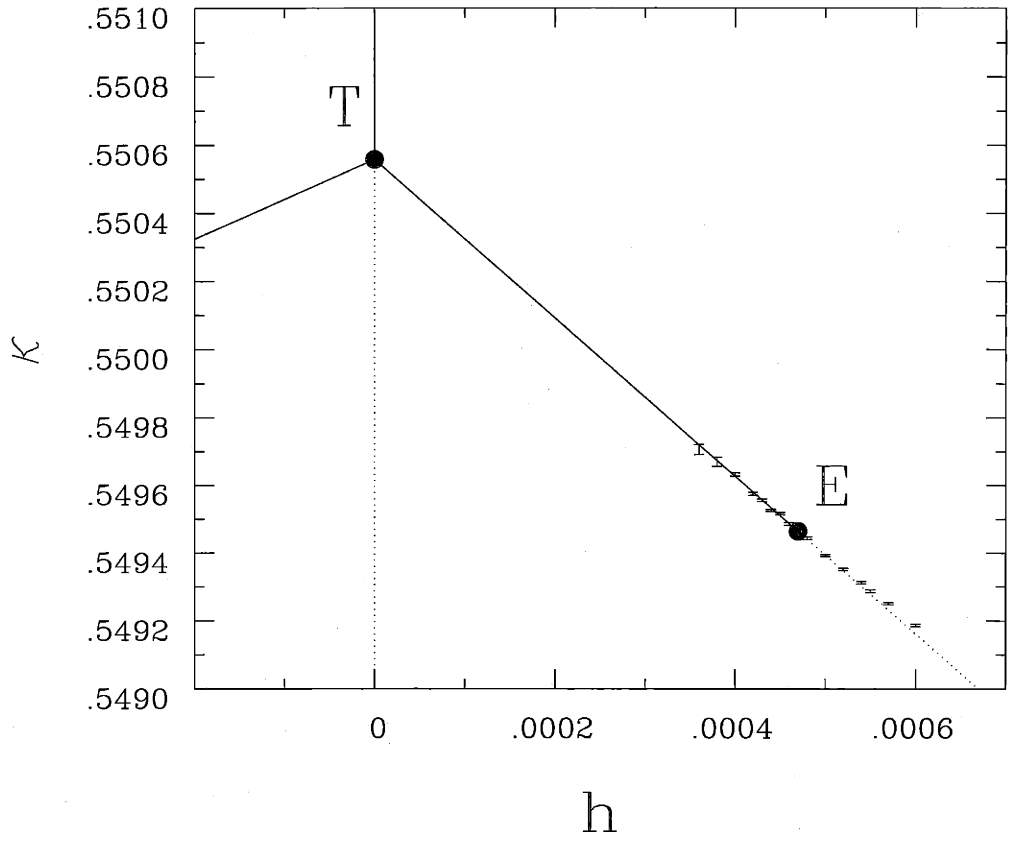

Figure 3-1: *The phase diagram of the* $\mathbf{Z}(3)$ *Potts model in the* (h, κ)*-plane. The ordinary deconfinement phase transition at* $T = (0, 0.550565(10))$ *is a triple point from which a line of first order phase transitions emerges. This line terminates in the critical endpoint* $E = (0.000470(2), 0.549463(13))$ *and continues only as a crossover.*

critical behavior. Similar methods were used recently by Karsch and Stickan [77] in a version of the 3-d 3-state Potts model where the action is real, and the endpoint was found to have the critical exponents of the 3-d Ising model. We find that in the Potts model with complex action the endpoint has the same critical properties. Furthermore its position is barely shifted in comparison to the model with real action. We do not limit our attention to the endpoint, but develop a method that solves the complex action problem everywhere in the phase diagram.

We also calculate the potentials between static quarks and anti-quarks in the Potts model approximation to QCD. In the confined phase at $\mu = 0$ the static quark-anti-

quark potential is linearly rising with the distance as a manifestation of confinement. For the same reason the quark-quark and anti-quark-anti-quark potentials are infinite at all distances. In the deconfined phase the quark-anti-quark potential reaches a plateau at twice the (now finite) free energy of a quark. Similarly, the quark-quark and anti-quark-anti-quark potentials are no longer infinite. It should be noted that quark-quark and anti-quark-anti-quark potentials are usually not calculated in lattice simulations. This is because—as a consequence of the $\mathbf{Z}(3)$ Gauss law—quark or anti-quark pairs cannot exist in a finite spatial volume with periodic boundary conditions [78]. Interestingly, this changes for $\mu \neq 0$ because then there are compensating background charges in the medium that can absorb the $\mathbf{Z}(3)$ flux of an external quark. Since the chemical potential explicitly breaks the $\mathbf{Z}(3)$ symmetry, there is no longer a clear distinction between confinement and deconfinement for $\mu \neq 0$. This manifests itself in the phase diagram by the fact that confined and deconfined phases are analytically connected. Figure 3-2 shows the quark-anti-quark, quark-quark and anti-quark-anti-quark potentials on the confined side (a) and on the deconfined side (b) of the crossover. Note that at $\mu \neq 0$ even in the confined phase the quark-anti-quark potential now reaches a plateau. The plateau height corresponds to the sum of the free energies F_Q of an external quark and $F_{\bar{Q}}$ of an external anti-quark. For $\mu > 0$ quarks are favored in the medium while anti-quarks are suppressed. As a consequence, the free energy of an external static quark is larger than that of an external static anti-quark. While an external static anti-quark can bind with a single background quark from the medium and form a meson, an external static quark needs two quarks from the medium to form a baryon. Indeed, on the confined side of the transition F_Q is clearly larger than $F_{\bar{Q}}$, while on the deconfined side F_Q and $F_{\bar{Q}}$ are more or less the same. We have normalized the potentials such that at zero distance a static quark-anti-quark pair has zero energy. In the Potts model, two quarks at zero distance are indistinguishable from a single anti-quark, and similarly, two anti-quarks on top of each other behave like a single quark. Hence, at zero distance the

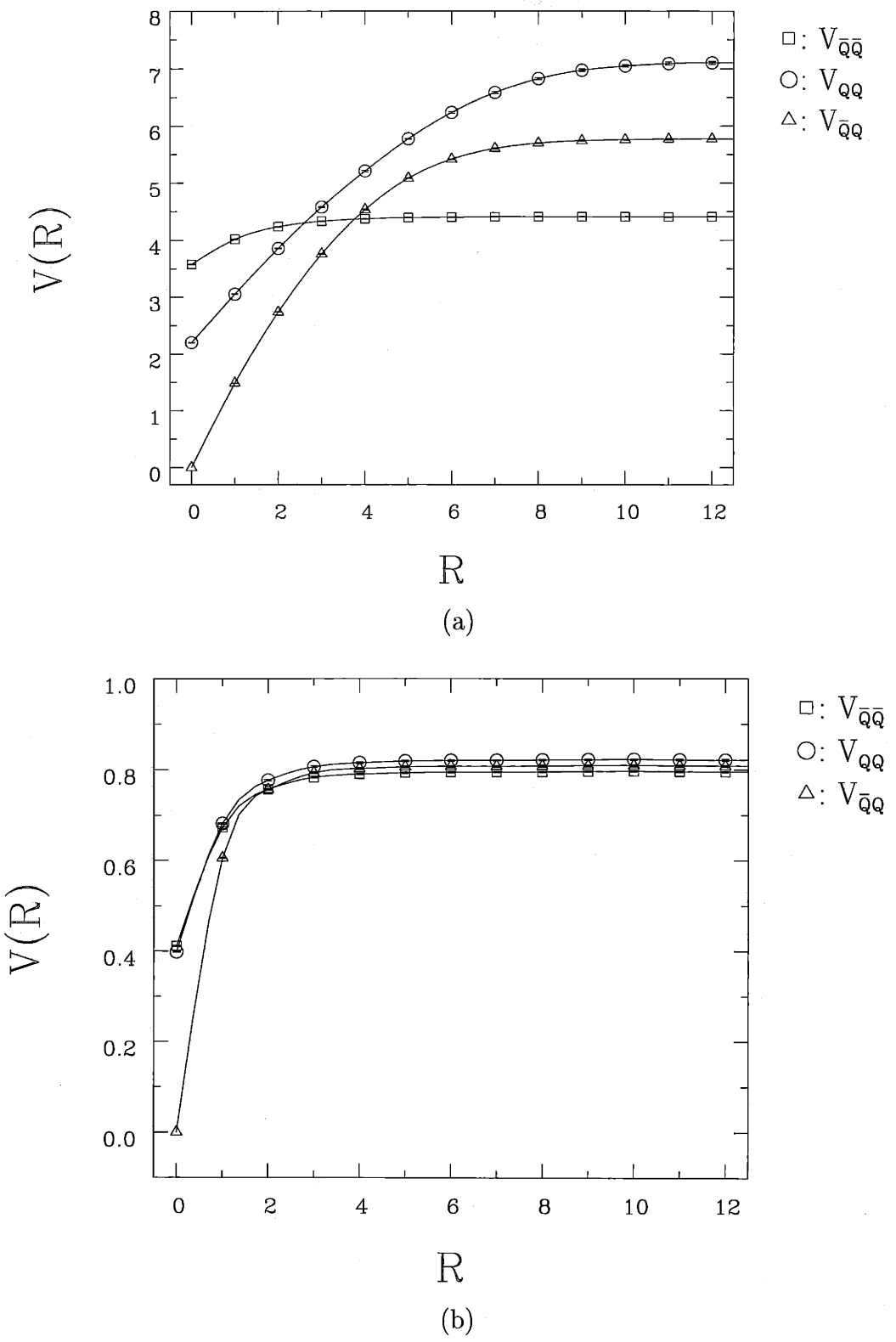

Figure 3-2: *The static quark-anti-quark, quark-quark and anti-quark-anti-quark potentials (a) on the confined side (at $h = 0.01$, $\kappa = 0.50$) and (b) on the deconfined side (at $h = 0.01$ and $\kappa = 0.56$) of the crossover.*

quark-quark potential $V_{QQ}(0)$ agrees with the free energy of a single anti-quark $F_{\bar{Q}}$ and the anti-quark-anti-quark potential obeys $V_{\bar{Q}\bar{Q}}(0) = F_Q$. At asymptotic distances the potentials $V_{Q\bar{Q}}(\infty)$, $V_{QQ}(\infty)$ and $V_{\bar{Q}\bar{Q}}(\infty)$ take the values $F_Q + F_{\bar{Q}}$, $2F_Q$ and $2F_{\bar{Q}}$, respectively. This behavior is consistent with our numerical data shown in figure 3-2.

In the absence of a chemical potential, the Potts model can be simulated with the original Swendsen-Wang cluster algorithm [79]. When a chemical potential is introduced, the Potts model suffers from the complex action problem and standard importance sampling methods including the cluster algorithm fail. In chapter 4, we construct an improved estimator for the μ-dependent part of the Boltzmann factor by averaging analytically over all configurations related to each other by cluster flips. In contrast to the original Boltzmann factor, the improved estimator is real and positive and can be used for importance sampling. This solves the complex action problem completely.

Although the Potts model inherits the complex action problem from QCD, it can be transformed into a "flux model" that has no complex action problem [76]. The flux model has been simulated in [76] and the disappearance of the first order deconfining phase transition at large chemical potential has been observed numerically. These results may give encouragement to the hope that QCD itself could be transformed into a model without a complex action problem. In this thesis we show that, at least for the Potts model, it is more efficient to leave it in its usual form and solve the complex action problem with our cluster algorithm than to transform it into a flux model and use conventional Metropolis methods.

Section 3.1 contains a derivation of the effective gluon action resulting from static quarks with large chemical potential as well as its Potts model approximation. In chapter 4 we describe the cluster algorithm that solves the complex action problem. Chapter 5 contains the derivation of the flux representation of the Potts model and a description of a Metropolis algorithm to simulate it. A comparison of the Metropolis algorithm for the flux model and the cluster algorithm for the original Potts model

shows that the latter is more efficient. In chapter 6 we present the physical results concerning the critical endpoint E. Using finite-size scaling techniques, we are able to determine the position of the critical endpoint of the deconfinement phase transition to high accuracy. Our results are consistent with the expected universal 3-d Ising behavior.

3.1 QCD with heavy quarks and the 3-d 3-state Potts model

The partition function for a pure $SU(3)$ Yang-Mills theory is given by

$$Z = \int \mathcal{D}A \ \exp(-S[A]), \tag{3.1}$$

where

$$S[A] = \int_0^\beta dt \int d^3x \ \frac{1}{2g^2} \mathrm{Tr}[F_{\mu\nu}F_{\mu\nu}], \tag{3.2}$$

is the Euclidean action for the gluons and β is the inverse temperature. The action is invariant under gauge transformations

$$g(\vec{x}, 0) = g(\vec{x}, \beta)z, \tag{3.3}$$

that are periodic in Euclidean time up to an element z of the center $\mathbf{Z}(3)$ of the non-Abelian gauge group. In the presence of a single external heavy quark of bare mass M at an undetermined position $\vec{x}$ the partition function turns into

$$Z_Q = \int \mathcal{D}A \ \Phi[A] \exp(-S[A]) \exp(-\beta M), \tag{3.4}$$

where

$$\Phi[A] = \int d^3x \ \mathrm{Tr}[\mathcal{P} \exp(-\int_0^\beta dt \ A_4(\vec{x}, t))], \tag{3.5}$$

is the spatial integral of the Polyakov loop. Ultimately, the mass M will be sent to infinity. Note that while the center transformation of eq.(3.3) leaves the pure gluon action $S[{}^g A] = S[A]$ invariant, the Polyakov loop transforms into

$$\Phi[{}^g A] = z\Phi[A]. \tag{3.6}$$

This shows that in the presence of the external quark, the $\mathbf{Z}(3)$ symmetry is explicitly broken. The partition function for a system of gluons in the presence of a single heavy anti-quark is given by

$$Z_{\bar{Q}} = \int \mathcal{D}A \; \Phi[A]^* \exp(-S[A]) \exp(-\beta M), \tag{3.7}$$

where $*$ denotes complex conjugation. Let us now consider a system of gluons in a background of n static quarks and $\bar{n}$ static anti-quarks. The partition function then takes the form

$$Z_{n,\bar{n}} = \int \mathcal{D}A \; \frac{1}{n!}\Phi[A]^n \frac{1}{\bar{n}!}(\Phi[A]^*)^{\bar{n}} \exp(-S[A]) \exp(-\beta M(n+\bar{n})). \tag{3.8}$$

The factors $1/n!$ and $1/\bar{n}!$ appear because quarks are indistinguishable, as are anti-quarks. Introducing the quark chemical potential μ that couples to $(n-\bar{n})$, i.e. three times the baryon number, we obtain the grand canonical partition function

$$\begin{aligned} Z(\mu) &= \sum_{n,\bar{n}} Z_{n,\bar{n}} \exp(\beta\mu(n-\bar{n})) \\ &= \sum_{n,\bar{n}} \int \mathcal{D}A \; \frac{1}{n!}\Phi[A]^n \frac{1}{\bar{n}!}(\Phi[A]^*)^{\bar{n}} \exp(-S[A] - \beta n(M-\mu) - \beta\bar{n}(M+\mu)) \\ &= \int \mathcal{D}A \; \exp(-S[A] + \exp(-\beta(M-\mu))\Phi[A] + \exp(-\beta(M+\mu))\Phi[A]^*). \end{aligned} \tag{3.9}$$

As expected, the presence of quarks and anti-quarks leads to an explicit breaking of the $\mathbf{Z}(3)$ center symmetry. Furthermore, in the presence of a non-zero chemical potential the effective action for the gluons is complex. Note that in the $SU(2)$ case the action remains real because then the Polyakov loop itself is real, i.e. $\Phi[A]^* = \Phi[A]$. The action becomes real even in the $SU(3)$ case if μ is purely imaginary. Furthermore, one can see that the chemical potential explicitly breaks the charge conjugation symmetry that replaces $\Phi[A]$ by $\Phi[A]^*$. In fact, under charge conjugation the action turns into its complex conjugate. We have assumed that the quarks are static. Hence, to be consistent we must consider the limit $M \to \infty$. In order to obtain a non-trivial result, we simultaneously take the limit $\mu \to \infty$ such that $M - \mu$ remains finite. The partition function then simplifies to

$$Z(\mu) = \int \mathcal{D}A \ \exp(-S[A] + \exp(-\beta(M-\mu))\Phi[A]). \tag{3.10}$$

As discussed in [29] and [30], a similar result can be obtained by simplifying the full QCD quark determinant in the static quark limit. In general the determinant would contain all Wilson loops, but because M is large most of them are suppressed. The only ones that survive are those for which the enhancement due to the chemical potential compensates for the suppression due to the mass. These are the Polyakov loops that progress in a straight line from Euclidean time $t = 0$ to $t = \beta$ at some position $\vec{x}$. In the loop expansion of the quark determinant, each of these has a weight $\exp(-\beta(M-\mu))$.

Up to this point we have treated QCD consistently in the static quark limit. The resulting effective action for the gluons is complex and we presently don't know how to simulate it efficiently. For that reason we now replace the gluon system by a simple 3-d lattice 3-state Potts model. The Potts spins $\Phi_x \in \mathbf{Z}(3)$ replace the original

Polyakov loop variables and the partition function turns into

$$Z(h) = \int \mathcal{D}\Phi \ \exp(-S[\Phi] + h\sum_x \Phi_x), \tag{3.11}$$

where h replaces $\exp(-\beta(M-\mu))$. Note that the Potts model action is still complex. In principle, one can imagine integrating out all QCD degrees of freedom except for the $\mathbf{Z}(3)$ phase of the Polyakov loop and thus derive an effective Potts model action directly from QCD. In practice this is impossible, except in the strong coupling limit. For simplicity, we therefore replace the pure gluon action $S[A]$ by a standard nearest-neighbor Potts model interaction

$$S[\Phi] = -\kappa \sum_{x,i} \delta_{\Phi_x, \Phi_{x+i}}. \tag{3.12}$$

The coupling constant κ is not related in a simple way to the parameters of QCD. Still, a large value of κ corresponds qualitatively to the high-temperature deconfined phase, while small κ values correspond to the confined phase. As mentioned in the introduction, the Potts model also retains the general features of the QCD phase diagram. At $h = 0$ (M infinite, μ finite) there is a first-order phase transition as a function of κ, between the disordered (confined) phase that respects the $\mathbf{Z}(3)$ symmetry and the ordered (deconfined) phase that spontaneously breaks it. An order parameter for this transition is $\langle\Phi\rangle$. As h rises from zero, the chemical potential term explicitly breaks the $\mathbf{Z}(3)$ symmetry, the phase transition weakens, and then ends at a critical point. Correspondingly, in heavy-quark QCD the quarks begin to contribute to the partition function when μ gets close to M, and there is no longer an order parameter for deconfinement. The deconfining phase transition terminates at a critical endpoint.

Chapter 4

Cluster algorithm solution of the complex action problem

In this chapter we first discuss the general nature of the complex action problem and then discuss the cluster algorithm that solves this problem for the Potts model. We also construct improved estimators for various physical quantities.

4.1 The general nature of the complex action problem

When the action is complex the resulting Boltzmann factor cannot be interpreted as a probability and hence standard importance sampling techniques fail. When one uses just the absolute value of the Boltzmann factor for importance sampling and includes its complex phase in measured observables O, expectation values take the form

$$\begin{aligned} \langle O \rangle &= \frac{1}{Z} \int \mathcal{D}\Phi \; O[\Phi] \exp(-S[\Phi] + h \sum_x \Phi_x) \\ &= \frac{\langle O \exp(ih \sum_x \mathrm{Im}\Phi_x) \rangle_R}{\langle \exp(ih \sum_x \mathrm{Im}\Phi_x) \rangle_R}. \end{aligned} \tag{4.1}$$

The subscript R refers to a modified ensemble with a real action described by the partition function

$$Z_R = \int \mathcal{D}\Phi \ \exp(-S[\Phi] + h\sum_x \mathrm{Re}\Phi). \tag{4.2}$$

By definition we have

$$\begin{aligned} \langle \exp(ih\sum_x \mathrm{Im}\Phi_x)\rangle_R &= \frac{1}{Z_R}\int \mathcal{D}\Phi \ \exp(ih\sum_x \mathrm{Im}\Phi_x)\exp(-S[\Phi] + h\sum_x \mathrm{Re}\Phi) \\ &= \frac{Z}{Z_R} \approx \exp(-V(f - f_R)), \end{aligned} \tag{4.3}$$

where f and f_R are the free energy densities of the original complex and the modified real action systems, respectively, and V is the spatial volume. Hence, the denominator in eq.(4.1) becomes exponentially small as one increases the volume. The same is true for the numerator, because $\langle O\rangle$ itself is not exponentially large in V.

Although, in principle, simulating the modified ensemble is correct, in practice this method fails for large volumes. The reason is that observables are obtained as ratios of exponentially small numerators and denominators which are themselves averages of quantities of order one. This leads to very severe cancellations and requires an exponentially large statistics in order to obtain accurate results. To see this, we estimate the relative statistical error in the determination of the average phase of the Boltzmann factor $\exp(ih\sum_x \mathrm{Im}\Phi_x)$. Since $\langle \exp(ih\sum_x \mathrm{Im}\Phi_x)\rangle_R = Z/Z_R$ the average itself is real. When one generates N statistically independent field configurations in a Monte Carlo simulation, the resulting error to signal ratio is given by

$$\begin{aligned} \frac{\Delta \exp(ih\sum_x \mathrm{Im}\Phi_x)}{\langle \exp(ih\sum_x \mathrm{Im}\Phi_x)\rangle_R} &= \frac{\sqrt{\langle |\exp(ih\sum_x \mathrm{Im}\Phi_x) - \langle \exp(ih\sum_x \mathrm{Im}\Phi_x)\rangle_R|^2\rangle_R}}{\sqrt{N}\langle \exp(ih\sum_x \mathrm{Im}\Phi_x)\rangle_R} \\ &= \frac{\sqrt{1 - \langle \exp(ih\sum_x \mathrm{Im}\Phi_x)\rangle_R^2}}{\sqrt{N}\langle \exp(ih\sum_x \mathrm{Im}\Phi_x)\rangle_R} \approx \frac{\exp(V(f - f_R))}{\sqrt{N}}. \end{aligned} \tag{4.4}$$

For large V we have used $\langle \exp(ih\sum_x \mathrm{Im}\Phi_x)\rangle_R \ll 1$ as implied by eq.(4.3). Consequently, in order to obtain an acceptable error to signal ratio one must generate at

least $N \approx \exp(2V(f - f_R))$ configurations. For large volumes this is impossible in practice.

4.2 The cluster algorithm for the Potts model

Let us now outline the ideas that underlie the cluster algorithm that we use to solve the complex action problem. It is based on the original Swendsen-Wang cluster algorithm [79] for the Potts model without chemical potential. In fact, in the limit $h = 0$ our algorithm reduces to that algorithm. The Swendsen-Wang cluster algorithm decomposes the lattice into independent clusters of connected sites. Each spin belongs to exactly one cluster and all spins within a cluster are assigned the same random $\mathbf{Z}(3)$ element. In this section, we construct an improved estimator for the h-dependent part $\exp(h\sum_x \Phi_x)$ of the Boltzmann factor by analytically averaging it over all configurations related to each other by cluster flips. Although, for an individual configuration $\exp(h\sum_x \Phi_x)$ is in general complex, its improved estimator is always real and positive and can thus be used for importance sampling. This completely solves the complex action problem.

Let us first describe the original Swendsen-Wang algorithm for $h = 0$. In this method one introduces variables $b = 0, 1$ for each bond connecting neighboring lattice sites x and $y = x + \hat{i}$ and one writes the nearest neighbor Boltzmann factor as

$$\exp(\kappa\delta_{\Phi_x,\Phi_y}) = \sum_{b=0,1} [\delta_{b,1}\delta_{\Phi_x,\Phi_y}(e^\kappa - 1) + \delta_{b,0}]. \tag{4.5}$$

In the enlarged configuration space of spin and bond variables, the bond variables impose constraints between the spin variables. When a bond is put (i.e. when $b = 1$), the spin Boltzmann factor is $\delta_{\Phi_x,\Phi_y}(e^\kappa - 1)$ and hence the spin variables Φ_x and Φ_y at the two ends of the bond must be identical. On the other hand, when the bond is not put ($b = 0$), the spin Boltzmann factor is 1 and thus the variables Φ_x and Φ_y

fluctuate independently. The spin variables, in turn, determine the probability to put a bond. When the spins Φ_x and Φ_y are different, the bond Boltzmann factor is $\delta_{b,0}$ and thus the bond is not put. On the other hand, when Φ_x and Φ_y are the same, the bond Boltzmann factor is $[\delta_{b,1}(e^{\kappa}-1)+\delta_{b,0}]$. Consequently, a bond between parallel spins is put with probability $p = 1-e^{-\kappa}$. Note that for $\kappa = 0$ no bonds are put, while for $\kappa = \infty$ parallel spins are always connected by a bond.

The Swendsen-Wang cluster algorithm updates bond and spin variables in alternating order. First, for a given spin configuration, bonds are put with probability p between parallel neighboring spins. No bonds are put between non-parallel spins. Then the spins are updated according to the constraints represented by the resulting bond configuration. Spins connected by bonds must remain parallel, while spins not connected by bonds fluctuate independently. Hence, to update the spins, one must identify clusters, i.e. sets of spins that are connected by bonds. All spins in a cluster are parallel and are assigned the same random $\mathbf{Z}(3)$ element in the spin update. All spins belong to exactly one cluster. It should be noted that a cluster may consist of a single spin. A configuration consisting of N_C clusters can be viewed as a member of a sub-ensemble of 3^{N_C} equally probable configurations which result by assigning $\mathbf{Z}(3)$ elements to the various clusters in all possible ways. As was already pointed out by Swendsen and Wang, one can construct improved estimators for various physical quantities by averaging analytically over all 3^{N_C} configurations in a sub-ensemble. Since the number of clusters is proportional to the volume, this effectively increases the statistics by a factor that is exponentially large in V.

Let us construct an improved estimator for the h-dependent part $\exp(h\sum_x \Phi_x)$ of the Boltzmann factor. Although for an individual configuration this term is in general complex, its average over a sub-ensemble of 3^{N_C} configurations is always real and positive. This results from the following observations. The h-dependent part of

the Boltzmann factor is a product of cluster contributions

$$\exp(h\sum_x \Phi_x) = \prod_C \exp(h\sum_{x\in C} \Phi_x). \tag{4.6}$$

Since the clusters are independent, the sub-ensemble average is a product

$$\langle \exp(h\sum_x \Phi_x)\rangle_{3^{N_C}} = \prod_C \langle \exp(h\sum_{x\in C} \Phi_x)\rangle_3, \tag{4.7}$$

of 3-state averages for the individual clusters

$$\begin{aligned} \langle \exp(h\sum_{x\in C} \Phi_x)\rangle_3 &= \frac{1}{3}\sum_{\Phi\in \mathbf{Z}(3)} \exp(h|C|\Phi) \\ &= \frac{1}{3}[\exp(h|C|) + 2\exp(-h|C|/2)\cos(\sqrt{3}h|C|/2)] \\ &= W(C), \end{aligned} \tag{4.8}$$

which defines a weight $W(C)$ for each cluster. We have used the fact that all spins Φ_x in a given cluster C take the same value $\Phi \in \mathbf{Z}(3)$ so that $\sum_{x\in C} \Phi_x = |C|\Phi$ where $|C| = \sum_{x\in C} 1$ is the cluster size. It is easy to show that the expression in eq.(4.8) is always positive and can hence be used for importance sampling. This is crucial for a complete solution of the complex action problem.

For a given bond configuration one can integrate out the spin variables and one obtains

$$\begin{aligned} Z &= \int \mathcal{D}b\ (e^\kappa - 1)^{N_b}\ 3^{N_C} \prod_C W(C) \\ &= \int \mathcal{D}b\ (e^\kappa - 1)^{N_b} \prod_C [\exp(h|C|) + 2\exp(-h|C|/2)\cos(\sqrt{3}h|C|/2)]. \end{aligned} \tag{4.9}$$

Here N_b is the number of bonds that are put (i.e. have $b = 1$). The factor 3^{N_C} represents the number of allowed spin configurations for a given bond configuration and the factors $W(C)$ come from the improved estimator. The effective action for the

bond variables depends only on the sizes $|C|$ of the clusters corresponding to a given bond configuration. Note that the factor $1/3$ per cluster in eq.(4.8) cancels against the factor 3^{N_C}.

Our algorithm directly updates the partition function of eq.(4.9), i.e. it only operates on the bond variables while the spins are already integrated out analytically.[1] The bond variables that define the clusters are updated with a local algorithm. A bond whose value does not affect the cluster sizes is put with probability $p = 1 - e^{-\kappa}$. This happens when the two sites at its ends belong to the same cluster because they are connected indirectly through other bonds. A bond whose value affects the cluster sizes is put with a probability that depends on the sizes of the corresponding clusters. When the bond is not put ($b = 0$), its endpoints x and y belong to two different clusters C_1 and C_2 of sizes $|C_1|$ and $|C_2|$ and the corresponding Boltzmann weight is $3^2 W(C_1)W(C_2)$. On the other hand, when the bond is put ($b = 1$), its endpoints belong to the combined cluster $C_1 \cup C_2$ of size $|C_1| + |C_2|$. In that case, the Boltzmann weight is $3W(C_1 \cup C_2)(e^{\kappa} - 1)$. Hence, the bond is put with probability

$$q = \frac{W(C_1 \cup C_2)(e^{\kappa} - 1)}{3W(C_1)W(C_2) + W(C_1 \cup C_2)(e^{\kappa} - 1)}. \tag{4.10}$$

4.3 Improved estimators for physical quantities

In order to measure physical observables, it is crucial to construct improved estimators for them as well. Here we construct improved estimators for the Polyakov loop Φ_x, its charge conjugate Φ_x^*, as well as for the correlators $\Phi_x \Phi_y^*$, $\Phi_x \Phi_y$ and $\Phi_x^* \Phi_y^*$. The expectation values

$$\langle \Phi_x \rangle = \exp(-\beta F_Q), \ \langle \Phi_x^* \rangle = \exp(-\beta F_{\bar{Q}}), \tag{4.11}$$

[1] B. Scarlet was first to realize that the spin variables need not even be simulated.

determine the free energies F_Q of a quark and $F_{\bar{Q}}$ of an anti-quark. The Polyakov loop correlators determine the quark-anti-quark potential $V_{Q\bar{Q}}(x-y)$, the quark-quark potential $V_{QQ}(x-y)$ and the anti-quark-anti-quark potential $V_{\bar{Q}\bar{Q}}(x-y)$ via

$$\begin{aligned}
\exp(-\beta V_{Q\bar{Q}}(x-y)) &= \langle \Phi_x \Phi_y^* \rangle, \\
\exp(-\beta V_{QQ}(x-y)) &= \langle \Phi_x \Phi_y \rangle, \\
\exp(-\beta V_{\bar{Q}\bar{Q}}(x-y)) &= \langle \Phi_x^* \Phi_y^* \rangle.
\end{aligned} \tag{4.12}$$

The improved estimator for the Polyakov loop is given by the sub-ensemble average

$$\langle \Phi_x \exp(h \sum_z \Phi_z) \rangle_{3^{N_C}} = \frac{1}{3} \sum_{\Phi \in \mathbf{Z}(3)} \Phi \exp(h|C_x|\Phi) \prod_{C \neq C_x} W(C), \tag{4.13}$$

where C_x is the cluster that contains the point x. Hence, we obtain

$$\langle \Phi_x \rangle = \frac{1}{Z(h)} \int \mathcal{D}b \, \frac{1}{3W(C_x)} \sum_{\Phi \in \mathbf{Z}(3)} \Phi \exp(h|C_x|\Phi)(e^{\kappa}-1)^{N_b} \, 3^{N_C} \prod_C W(C), \tag{4.14}$$

i.e. after integrating out the spin variables, the Polyakov loop is represented by

$$\Phi_x = \frac{1}{3W(C_x)} \sum_{\Phi \in \mathbf{Z}(3)} \Phi \exp(h|C_x|\Phi). \tag{4.15}$$

Similarly, the operator representing the charge conjugate Polyakov loop is

$$\Phi_x^* = \frac{1}{3W(C_x)} \sum_{\Phi \in \mathbf{Z}(3)} \Phi^* \exp(h|C_x|\Phi). \tag{4.16}$$

The improved estimator for the Polyakov loop correlator $\Phi_x \Phi_y^*$ is given by the sub-ensemble average

$$\langle \Phi_x \Phi_y^* \exp(h \sum_z \Phi_z) \rangle_{3^{N_C}} = \frac{1}{3} \sum_{\Phi \in \mathbf{Z}(3)} \Phi \exp(h|C_x|\Phi) \, \frac{1}{3} \sum_{\Phi^* \in \mathbf{Z}(3)} \Phi^* \exp(h|C_y|\Phi)$$

$$\times \prod_{C \neq C_x, C_y} W(C), \tag{4.17}$$

if the points x and y belong to two different clusters C_x and C_y. If the points x and y belong to the same cluster (i.e. if $C_x = C_y$), the improved estimator is simply given by

$$\langle \Phi_x \Phi_y^* \exp(h \sum_z \Phi_z) \rangle_{3^{N_C}} = \prod_C W(C), \tag{4.18}$$

because then $\Phi_x \Phi_y^* = 1$. Hence, the operator representing the correlator is

$$\begin{aligned} \Phi_x \Phi_y^* &= \frac{1}{9W(C_x)W(C_y)} \sum_{\Phi \in \mathbf{Z}(3)} \Phi \exp(h|C_x|\Phi) \sum_{\Phi \in \mathbf{Z}(3)} \Phi^* \exp(h|C_y|\Phi), \text{ if } C_x \neq C_y, \\ \Phi_x \Phi_y^* &= 1, \text{ if } C_x = C_y. \end{aligned} \tag{4.19}$$

Similarly, we have

$$\begin{aligned} \Phi_x \Phi_y &= \frac{1}{9W(C_x)W(C_y)} \sum_{\Phi \in \mathbf{Z}(3)} \Phi \exp(h|C_x|\Phi) \sum_{\Phi \in \mathbf{Z}(3)} \Phi \exp(h|C_y|\Phi), \text{ if } C_x \neq C_y, \\ \Phi_x \Phi_y &= \frac{1}{3W(C_x)} \sum_{\Phi \in \mathbf{Z}(3)} \Phi^2 \exp(h|C_x|\Phi), \text{ if } C_x = C_y, \\ \Phi_x^* \Phi_y^* &= \frac{1}{9W(C_x)W(C_y)} \sum_{\Phi \in \mathbf{Z}(3)} \Phi^* \exp(h|C_x|\Phi) \sum_{\Phi \in \mathbf{Z}(3)} \Phi^* \exp(h|C_y|\Phi), \text{ if } C_x \neq C_y, \\ \Phi_x^* \Phi_y^* &= \frac{1}{3W(C_x)} \sum_{\Phi \in \mathbf{Z}(3)} (\Phi^*)^2 \exp(h|C_x|\Phi), \text{ if } C_x = C_y. \end{aligned} \tag{4.20}$$

4.4 Severity of the complex action problem

In order to estimate the severity of the complex action problem, we like to determine the expectation value of the complex phase of the Boltzmann factor in the modified real action ensemble

$$\langle \exp(ih \sum_x \mathrm{Im}\Phi_x) \rangle_R = \frac{Z}{Z_R}. \tag{4.21}$$

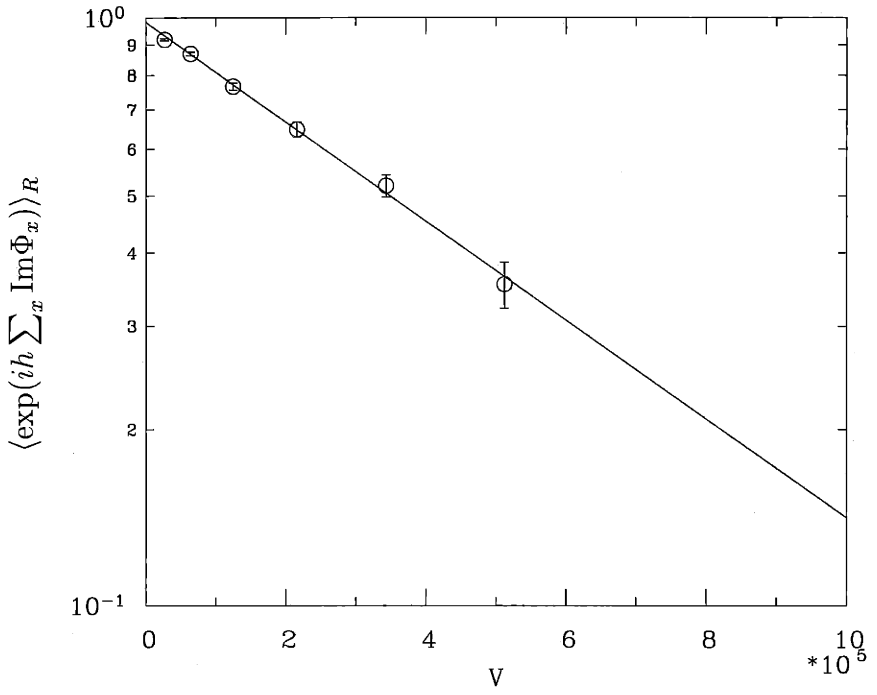

Figure 4-1: *The expectation value of the phase factor as a function of the volume at the critical endpoint E.*

Rather than implementing this directly in a simulation that uses the absolute value of the Boltzmann factor for importance sampling, one can measure Z_R/Z with the cluster algorithm. In fact, an improved estimator for this quantity is given by $\prod_C W_R(C)/W(C)$, where

$$W_R(C) = \langle \exp(h \sum_{x \in C} \mathrm{Re}\Phi_x) \rangle_3 = \frac{1}{3}[\exp(h|C|) + 2\exp(-h|C|/2)], \tag{4.22}$$

is the weight that replaces $W(C)$ in the real action ensemble. Alternatively, one can construct a cluster algorithm that simulates the real action ensemble. In that case, one needs to measure $\prod_C W(C)/W_R(C)$ in order to obtain Z/Z_R.

Figure 4-1 shows $\langle \exp(ih \sum_x \mathrm{Im}\Phi_x) \rangle_R$ as a function of the volume $V = L^3$ at the critical endpoint of the transition line (point E in figure 3-1). Indeed, one finds an exponentially small signal, as expected from eq.(4.3). Defining a scale parameter L_0

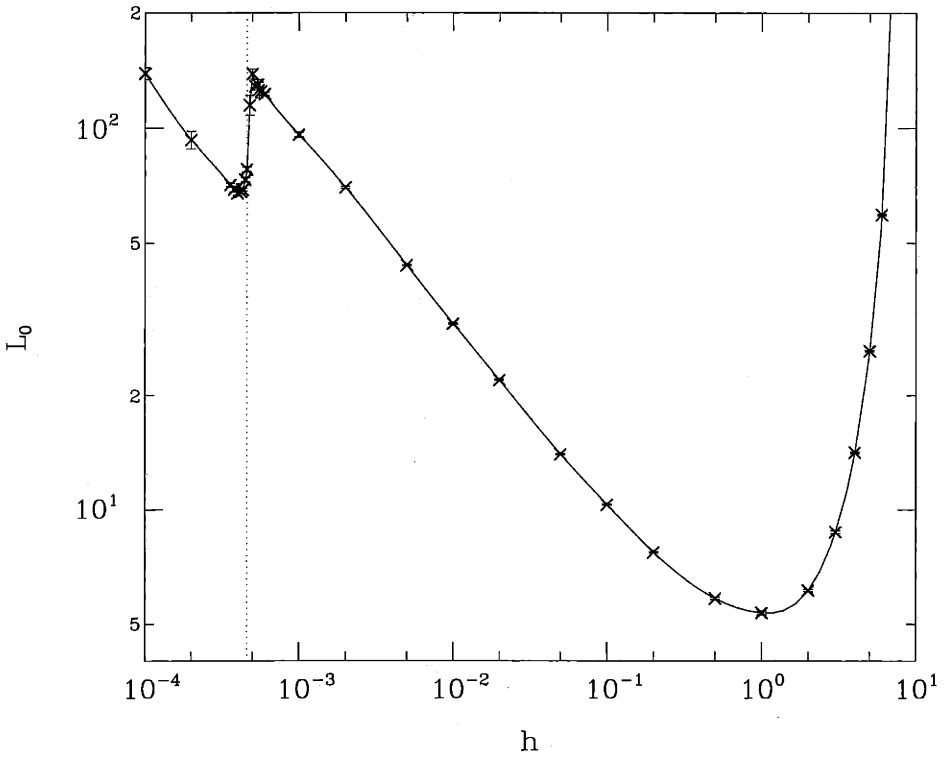

Figure 4-2: *The scale parameter L_0 related to the severity of the complex action problem as a function of h at $\kappa = 0.5495$. The solid line is a spline to guide the eye. The phase transition takes place at the dotted vertical line.*

that measures the severity of the complex action problem by

$$\langle \exp(ih \sum_x \mathrm{Im}\Phi_x) \rangle_R \propto \exp\left(-\frac{L^3}{L_0^3}\right) \tag{4.23}$$

we get $L_0 \approx 80$ at the endpoint E. This means that the complex action problem at the endpoint is extremely mild. In fact, in practice it is not a problem at all up to volumes as big as 100^3. Since the current computer hardware restricts the system size to a couple of million degrees of freedom, one can also study the point E with an algorithm that does not solve the complex action problem. On very large lattices the meron-cluster algorithm will become superior also at the point E since its computational effort is polynomial in the system size as opposed to exponential

for the reweighted Metropolis algorithm.

It should be noted that the complex action problem is most severe for intermediate values of h. While it is obvious that there is no complex action problem at $h = 0$, it is perhaps less obvious that there is also no problem for large h. This is because

$$\frac{W_R(C)}{W(C)} = \frac{\exp(h|C|) + 2\exp(-h|C|/2)}{\exp(h|C|) + 2\exp(-h|C|/2)\cos(\sqrt{3}h|C|/2)} \tag{4.24}$$

approaches 1 in the limit $h \to \infty$ so that $\langle \exp(ih\sum_x \mathrm{Im}\Phi_x)_R \rangle_R = Z_R/Z \to 1$. Figure 4-2 shows the complex action problem scale parameter L_0 as a function of h for fixed $\kappa = 0.5495$. It has a minimum at $h \approx 1$ meaning that the complex action problem is most severe in that region. Defining the "practical complex action problem" as being present when $\langle \exp(ih\sum_x \mathrm{Im}\Phi_x) \rangle_R < 0.01$ on a 100^3 lattice (i.e. $L_0 < 60$) we see that at $\kappa = 0.5495$ there is no practical complex action problem for $h < 0.003$ as well as for $h > 6$. A more physical definition of a practical complex action problem would compare L_0 with the correlation length ξ but we have not measured the correlation length.

Chapter 5

Flux representation of the Potts model

In this chapter we map the Potts model to an equivalent flux model that does not suffer from the complex action problem. Then we describe a Metropolis algorithm to update the flux model and compare its efficiency with the cluster algorithm.

5.1 Mapping the Potts model to a flux model

As pointed out in [76] the Potts model can be rewritten as a flux model that does not suffer from the complex action problem. As we have seen, the complex action problem can also be solved in the cluster formulation. Hence, the question arises if the flux or the cluster formulation leads to more efficient numerical simulations. Let us first match the flux model to the original Potts model. The flux model is formulated in terms of "electric" charges $Q_x \in \{0, \pm 1\}$ defined on the lattice sites x and electric flux variables $E_{x,i} \in \{0, \pm 1\}$ living on the links. The charge and flux variables are related by the $\mathbf{Z}(3)$ Gauss law constraint

$$Q_x = \sum_i (E_{x,i} - E_{x-\hat{i},i}) \text{mod } 3. \tag{5.1}$$

The action of the flux model takes the form

$$S[E,Q] = \frac{g^2}{2}\sum_{x,i} E_{x,i}^2 + \beta \sum_x (MQ_x^2 - \mu Q_x). \tag{5.2}$$

The mass M and the chemical potential μ of the $\mathbf{Z}(3)$ charges are not directly related to the mass and chemical potential of quarks in QCD (which we also denoted by M and μ in section 2) but qualitatively they play the same role. The partition function of the flux model takes the form

$$Z = \prod_x \sum_{Q_x \in \{0,\pm 1\}} \prod_{x,i} \sum_{E_{x,i} \in \{0,\pm 1\}} \prod_x \delta_x \exp(-S[E,Q]). \tag{5.3}$$

The δ-function δ_x imposes the Gauss law of eq.(5.1) at the point x and can be written as

$$\delta_x = \frac{1}{3} \sum_{\Phi_x \in \mathbf{Z}(3)} \Phi_x^{Q_x - \sum_i (E_{x,i} - E_{x-\hat{i},i})}. \tag{5.4}$$

Inserting this as well as eq.(5.2) for the action in eq.(5.3) one can integrate out the $E_{x,i}$ and Q_x variables. The result of the $E_{x,i}$ integration is

$$\sum_{E_{x,i} \in \{0,\pm 1\}} (\Phi_x^* \Phi_{x+\hat{i}})^{E_{x,i}} \exp\left(-\frac{g^2}{2} E_{x,i}^2\right) = 1 + 2\exp\left(-\frac{g^2}{2}\right) \mathrm{Re}(\Phi_x^* \Phi_{x+\hat{i}}). \tag{5.5}$$

In the Potts model (up to an overall factor) the corresponding term is $\exp(\kappa \delta_{\Phi_x, \Phi_{x+\hat{i}}})$. Thus, the flux model matches the Potts model if

$$\exp(\kappa) = \frac{1 + 2\exp(-g^2/2)}{1 - \exp(-g^2/2)}. \tag{5.6}$$

Note that the $g \to 0$ limit of the flux model corresponds to the $\kappa \to \infty$ limit of the Potts model. When one integrates out the charges Q_x one obtains

$$\sum_{Q_x \in \{0,\pm 1\}} \Phi_x^{Q_x} \exp(-MQ_x^2 - \mu Q_x) = 1 + \exp(-\beta(M-\mu))\Phi_x + \exp(-\beta(M+\mu))\Phi_x^*. \tag{5.7}$$

In the original Potts model (up to an overall factor A) the corresponding term is $\exp(h\Phi_x)$. Hence, the flux model matches the Potts model if

$$\begin{aligned}
\frac{1}{3}\sum_{\Phi\in\mathbf{Z}(3)} \exp(h\Phi) &= A, \\
\frac{1}{3}\sum_{\Phi\in\mathbf{Z}(3)} \Phi\exp(h\Phi) &= A\exp(-\beta(M+\mu)), \\
\frac{1}{3}\sum_{\Phi\in\mathbf{Z}(3)} \Phi^*\exp(h\Phi) &= A\exp(-\beta(M-\mu)).
\end{aligned} \tag{5.8}$$

These relations can be used to determine the parameters $\exp(-\beta(M-\mu))$ and $\exp(-\beta(M+\mu))$ of the flux model in terms of the Potts model parameter h.

5.2 Metropolis algorithm for the flux model and comparison with the cluster algorithm

As first described in [76], the flux model can be updated with a simple Metropolis algorithm. One basic move in the algorithm creates or annihilates a nearest-neighbor charge-anti-charge pair across a given link. The other basic move creates or annihilates an electric flux loop around an elementary plaquette. These basic moves are proposed on every link and plaquette and are accepted or rejected in a Metropolis step. We have implemented both the Metropolis algorithm for the flux model and the cluster algorithm for the Potts model and we have verified that physical observables obtained with the two algorithms agree with each other.

The question arises which of the two algorithms is more efficient. The Metropolis algorithm is expected to suffer from critical slowing down at the endpoint of the first order phase transition with a dynamical critical exponent $z \approx 2$. Cluster algorithms are known to drastically reduce critical slowing down, in some cases even to $z \approx 0$. However, our cluster algorithm cannot eliminate critical slowing down completely

because the decision to put a bond is more time-consuming than the one in the Swendsen-Wang algorithm. For example, when a bond is removed, one must check if an old cluster decomposes into two new clusters. To minimize the computational effort, we simultaneously grow two clusters from the two ends of the bond. Once they touch each other, we know that the old cluster did not decay. Still, in the less likely event that the old cluster does decay, one must completely grow the smaller of the two clusters in order to decide if the bond can be deleted. Here we do not attempt to determine the dynamical critical exponent z of our cluster algorithm at the critical endpoint.

An even more severe super-critical slowing down is expected close to the first order phase transition line. Along that line, the deconfined phase coexists with the confined phase, and the Monte Carlo simulation must tunnel between the two phases. In order to tunnel between the confined and the deconfined phase, a local algorithm must go through configurations containing both phases simultaneously. Since the interface that separates the two phases has non-zero interface tension, such configurations are exponentially suppressed. Hence, close to a first order phase transition, a local algorithm like the Metropolis algorithm necessarily suffers from exponential slowing down. This super-critical slowing down is even more severe than the power-law critical slowing down at a second order phase transition. Hence, we expect that the Metropolis algorithm for the flux model is not very well suited to study the first order phase transition line. In some cases, cluster algorithms can even eliminate super-critical slowing down. For example, in the broken phase of the Potts model three distinct deconfined phases coexist with each other. The Swendsen-Wang algorithm can efficiently tunnel from one deconfined phase to another because it assigns the same random $\mathbf{Z}(3)$ element to all spins in a cluster in a non-local spin update. Still, even the Swendsen-Wang algorithm suffers from super-critical slowing down at the first order phase transition that separates the confined from the deconfined phase. Although cluster flips can naturally lead to tunneling between distinct decon-

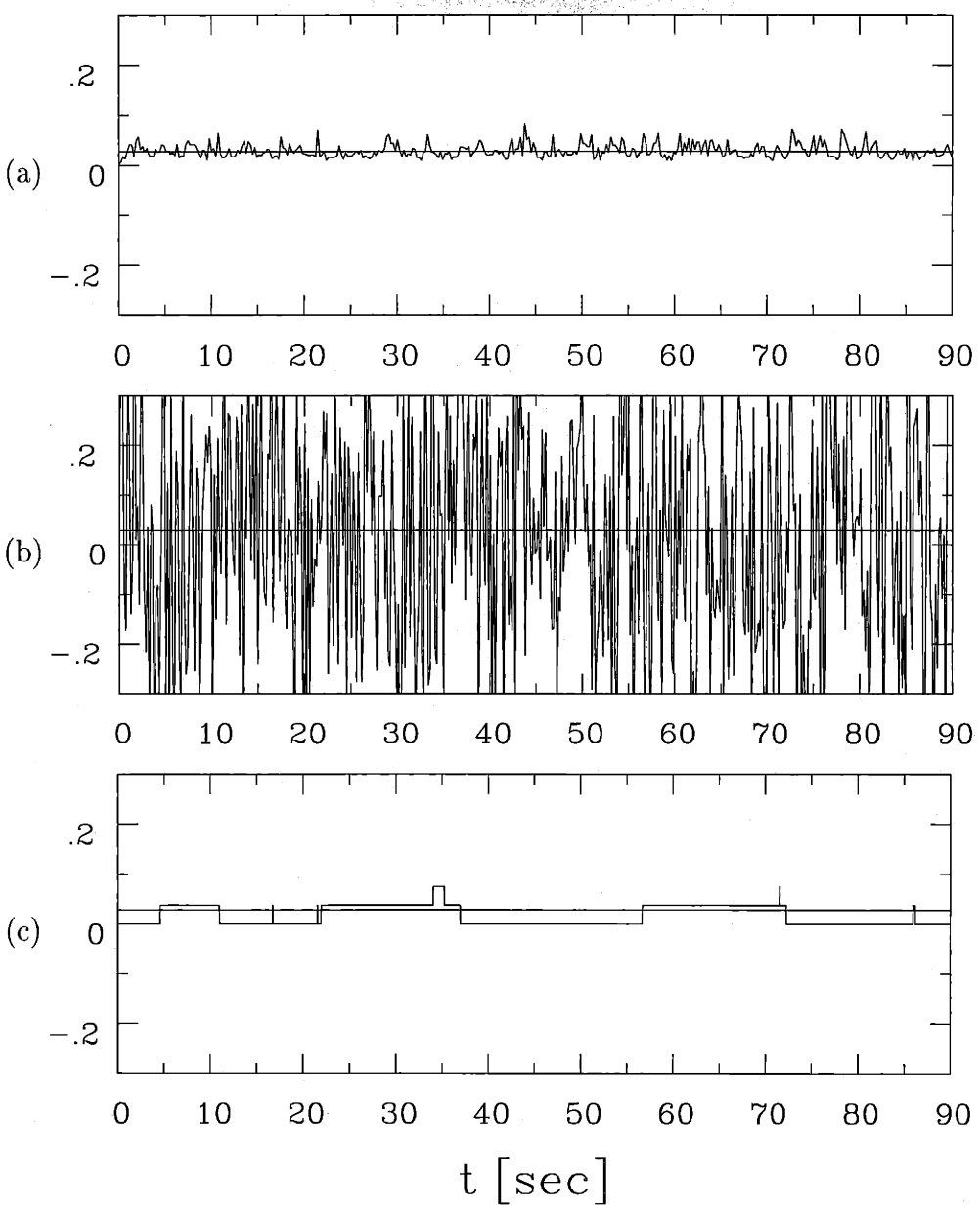

Figure 5-1: *The computer time history of the Polyakov loop Φ (a) for the cluster algorithm for the Potts model using the improved estimator for Φ, (b) for the Metropolis algorithm for the Potts model using Φ directly, and (c) for the Metropolis algorithm for the flux model on a 20^3 lattice at $(h, \kappa) = (0.01, 0.5)$. The horizontal straight line denotes the expectation value. The Metropolis algorithm for the flux model has a much longer autocorrelation time than the other two algorithms. In the case of the Metropolis algorithm for the Potts model the complex action problem manifests itself by large fluctuations around the expectation value.*

fined phases, they do not lead directly from a deconfined to the confined phase. To cure this problem, Rummukainen [80] has combined the cluster algorithm with the multi-canonical methods of Berg and Neuhaus [81] which can reduce the exponential super-critical slowing down to a power-law behavior. Although this may well be possible, we have not yet attempted to combine our algorithm with multi-canonical methods. Hence, we expect that our cluster algorithm still suffers from super-critical slowing down close to the deconfinement phase transition.

We have compared the efficiency of the Metropolis algorithm for the flux model, the cluster algorithm for the complex action Potts model, and the reweighted Metropolis algorithm for the complex action Potts model at several points in the phase diagram. In figure 5-1 we compare the computer time histories of the Polyakov loop for the three algorithms mentioned above at $(h, \kappa) = (0.01, 0.5)$ which is in the confined region of the phase diagram. Obviously, the flux model Metropolis algorithm decorrelates a lot worse than the other two algorithms. The flux algorithm performs even worse when one approaches the first order transition line. The reweighted Metropolis algorithm for the Potts model suffers from the complex action problem. What is plotted is the time evolution of $\mathrm{Re}[\sum_x \Phi_x \exp(ih \sum_x \mathrm{Im}\Phi_x)]/V\langle \exp(ih \sum_x \mathrm{Im}\Phi_x)\rangle_R$. Its statistical fluctuations are much larger than the expectation value which is a manifestation of the complex action problem.

Chapter 6

Universality class of the critical endpoint

In this chapter we present the results of our numerical simulations at the critical endpoint. The complex action problem turned out to be very weak in the vicinity of the critical endpoint (see subsection 4.4). Therefore it is possible to use a simple reweighted Metropolis algorithm even though that does not solve the complex action problem. It is usable up to sufficiently large lattices so that critical exponents can be extracted from a finite size scaling analysis. Of course, on even larger lattices the meron-cluster algorithm will eventually be superior to the reweighted Metropolis algorithm. But since at the endpoint E the complex action problem sets in only at volumes $\gtrsim 100^3$, simulations at E are not limited by the complex action problem but by the ability to simulate large lattices on today's computers.

Figure 3-1 shows the phase diagram of the model defined by equation (3.11). For $h = 0$ our model reduces to the standard 3-d 3-state Potts model which has been studied extensively in Monte Carlo simulations [82]. The model is known to have a weak first order phase transition. The value of the coupling κ where the phase transition occurs (point T in figure 3-1) has been determined with high precision. In [82], the phase transition was found to occur at $\kappa_T = 0.550565(10)$. Above this

value the $\mathbf{Z}(3)$ symmetry is spontaneously broken, i.e. for $\kappa > \kappa_T$ three distinct deconfined phases coexist. When we switch on the parameter h, the $\mathbf{Z}(3)$ symmetry gets explicitly broken. Positive values of h favor the deconfined phase with a real value of $\langle\Phi\rangle$. Hence, the line $\kappa > \kappa_T$ at $h = 0$ is a line of first order phase transitions which cannot terminate in the deconfinement transition at the point T. In fact, T is a triple point because two other first order transition lines emerge from it. For $h > 0$ a line of first order transitions extends into the (h, κ)-plane and terminates in a critical endpoint (E in figure 3-1). Negative values of h favor the two deconfined phases with complex values of $\langle\Phi\rangle$. Negative h are unphysical in the QCD interpretation of the Potts model because h represents $\exp(-\beta(M - \mu))$ in QCD. Still, the Potts model at $h < 0$ makes perfect sense as a statistical mechanics system (unrelated to QCD) and it has another first order transition line emerging from the point T. Interestingly, with our method the complex action problem can only be solved for $h \geq 0$ since otherwise the improved estimator of eq.(4.8) is not necessarily positive. It should be noted that for $h < 0$ also the flux model suffers from the complex action problem.

The line of first order phase transitions $\kappa_t(h)$ is determined by the condition that the free energy densities of the confined and deconfined phases are equal, i.e.

$$f_c(h, \kappa_t(h)) = f_d(h, \kappa_t(h)). \tag{6.1}$$

Close to the point $T = (0, \kappa_T)$ the free energy density of the confined phase is given by

$$f_c(h, \kappa) = f_{c,T} + e_{c,T}(\kappa - \kappa_T), \tag{6.2}$$

where $f_{c,T} = f_c(0, \kappa_T)$ and $e_{c,T} = df_c/d\kappa(0, \kappa_T)$ is the energy density of the confined phase at the point T. Note that to leading order $f_c(h, \kappa)$ is independent of h because $\langle\Phi\rangle = 0$ in the confined phase at $h = 0$. On the other hand, for the deconfined phase one obtains

$$f_d(h, \kappa) = f_{d,T} + e_{d,T}(\kappa - \kappa_T) - h\langle\Phi\rangle_T, \tag{6.3}$$

where $\langle\Phi\rangle_T$ is the value of the Polyakov loop at the point T in the deconfined phase that is favored at $h > 0$. Using the condition $f_{c,T} = f_{d,T}$ for the deconfinement phase transition at $h = 0$, one finds

$$\kappa_t(h) = \kappa_T - \frac{\langle\Phi\rangle_T}{e_{c,T} - e_{d,T}} h = \kappa_T - \frac{h}{r}. \tag{6.4}$$

The Monte Carlo data of [82] and [83] imply $r = 0.41(1)$. Our data are consistent with the first order transition line being a straight line. Fitting the values of $\kappa_t(h)$ obtained from the infinite volume extrapolation described below yields $r = 0.430(6)$ in reasonable agreement with the number from above. Similarly, one can determine the angle at which the third transition line leaves the point T in the direction of negative h. A similar argument can be applied to the Potts model with real action that was studied in [77]. Also in that case the first order phase transition line is consistent with a straight line and again the predicted position for the transition line agrees with the numerical data. Interestingly, for the Potts model with both real and complex action, information at $h = 0$ is sufficient to predict the position of the transition line for $h > 0$. This is because the transition at $h = 0$ is rather weak and the line ends already at small values of h. If the transition would extend deep into the (h, κ)-plane one would expect deviations from a straight line that would be hard to predict based on data at $h = 0$.

To determine the location of the transition line numerically we perform for given values of h and the volume V simulations at 3 to 5 different values of κ. These simulations are then combined with Ferrenberg Swendsen multi-histogram reweighting [84]. To estimate the position of the transition line we use the specific heat

$$C = \frac{1}{V}\left(\langle(S[\Phi] - h\sum_x \Phi_x)^2\rangle - \langle(S[\Phi] - h\sum_x \Phi_x)\rangle^2\right) \tag{6.5}$$

and determine the position of its maximum $\kappa_t(h, V)$ for a given h and V. The

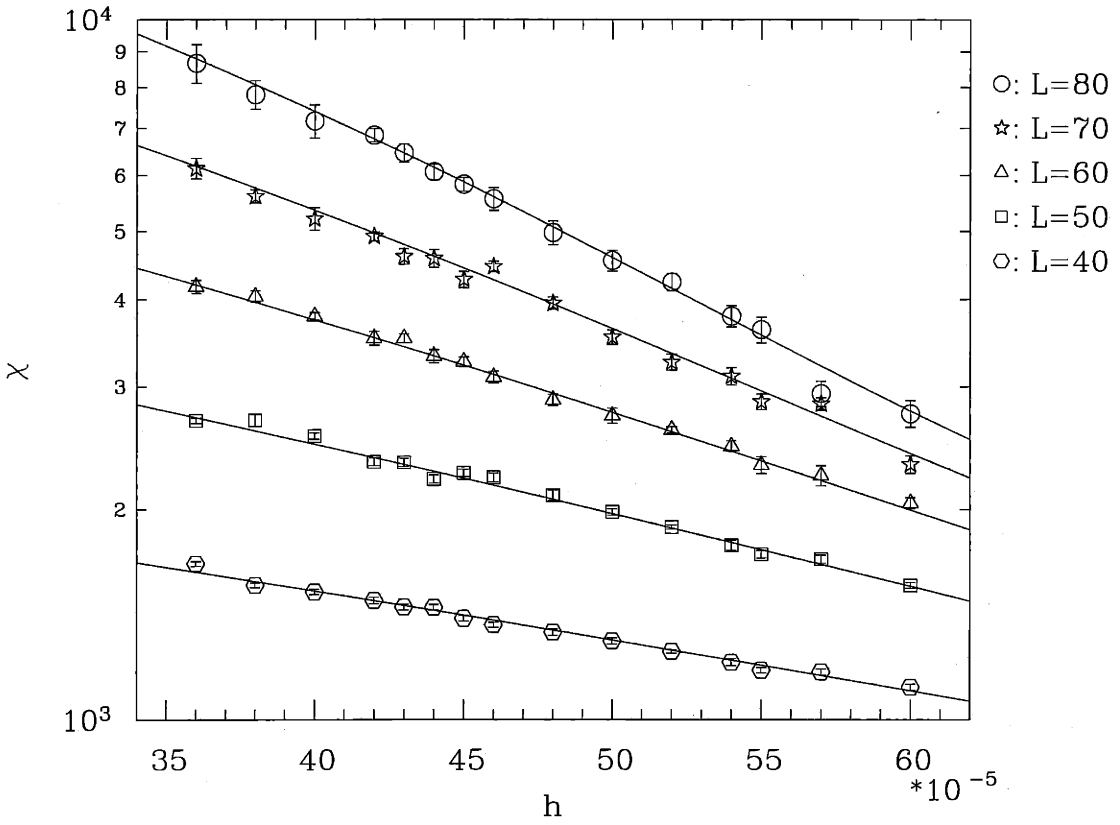

Figure 6-1: *The susceptibility χ along the transition line plotted as a function of h for five different volumes.*

transition point $\kappa_t(h)$ is determined in the infinite volume limit using

$$\kappa_t(h, V) = \kappa_t(h) + \frac{A(h)}{V} \tag{6.6}$$

where $\kappa_t(h) = \kappa_t(h, V = \infty)$. This ansatz is used successfully in the whole h-range, i.e. for the first order region as well as in the crossover region. The values for $\kappa_t(h)$ are plotted with errorbars into the phase diagram (figure 3-1). On the first order transition line they are consistent with a straight line which intersects the κ axis exactly at the point T. The crossover line has a slight curvature.

After we have determined the tangent to the first order transition line close to the endpoint we still have to find the exact location of the endpoint on that line. Also we

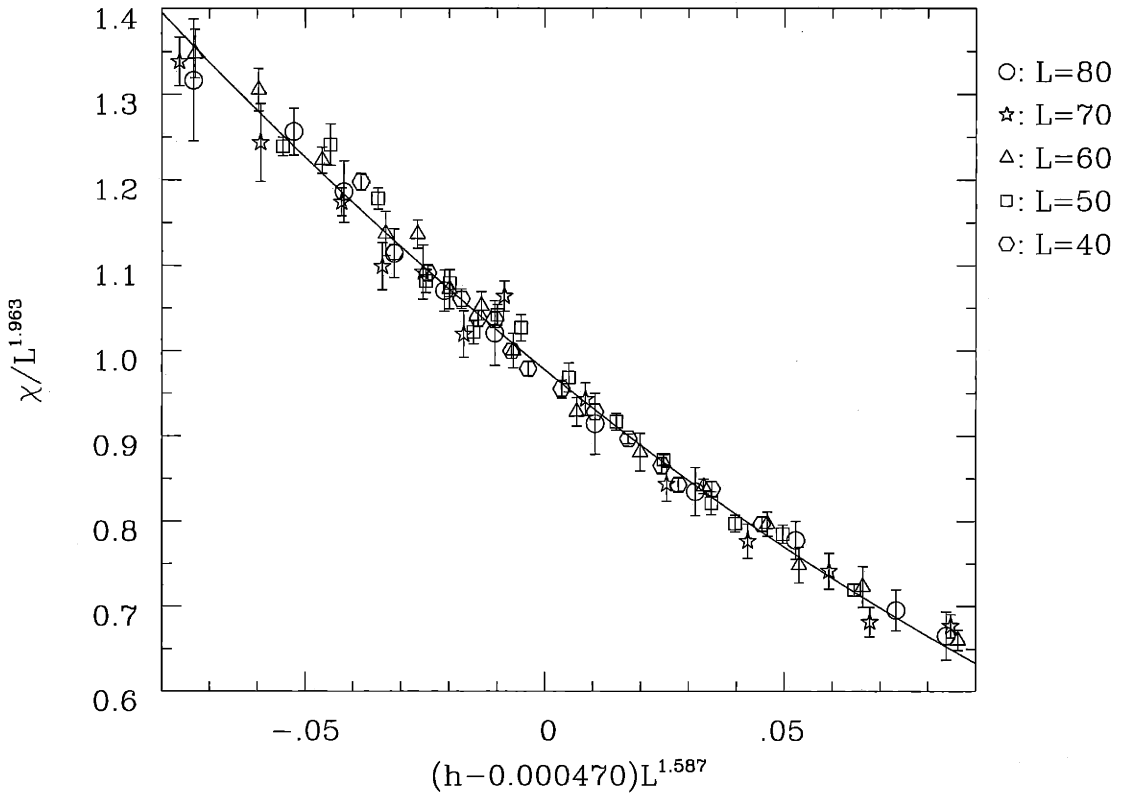

Figure 6-2: *The scaling function* $f(x)$.

want to extract critical exponents. For that purpose we consider the Polyakov loop susceptibility

$$\chi = \frac{1}{V}\left(\langle(\sum_x \Phi_x)^2\rangle - \langle\sum_x \Phi_x\rangle^2\right) \tag{6.7}$$

along the transition line, i.e. at the points $(\kappa_t(h), h)$. One could consider a "rotated susceptibility" instead, where an admixture of the kinetic energy term is added to the Polyakov loop to diagonalize the fluctuation matrix. Nevertheless, this is not necessary, since the "magnetic field direction" is the dominant one. We explicitly checked that the results do not depend on the admixture we chose, unless one comes close to the linear combination where the discontinuities of the Polyakov loop and the kinetic energy cancel. This linear combination would correspond to the kinetic energy term in the Ising model. Of course, if one would be interested in observables

related to the kinetic energy of the Ising model, one would have to exactly choose the linear combination that corresponds to the kinetic energy direction.

Close to the critical point the following scaling ansatz describes the susceptibility (see e.g. [85])

$$\chi = L^{\gamma/\nu} f(x), \quad x = (h - h_c) L^{1/\nu}. \tag{6.8}$$

For the fit, the function $f(x)$ is expanded in a Taylor series around $x = 0$ up to second order, $f(x) = f_0 + f_1 x + f_2 x^2/2$. We perform two fits:

- Six parameter fit: It results in $1/\nu = 1.532(57)$, $\gamma/\nu = 2.064(70)$, $h_c = 0.000445(18)$, $f_0 = 0.70(16)$, $f_1 = -3.99(95)$, and $f_2 = 16.4(60)$ with $\chi^2/\text{d.o.f.} = 1.33$. The results for the exponents agree with the estimates for the 3-d Ising universality class $1/\nu = 1.587(2)$ and $\gamma/\nu = 1.963(3)$ [85] almost within error-bars.

- Four parameter fit: The critical exponents are fixed to the Ising model values. The result is $h_c = 0.000470(2)$, $f_0 = 0.9775(46)$, $f_1 = -4.567(55)$, and $f_2 = 16.5(17)$ with $\chi^2/\text{d.o.f.} = 1.35$. The good value for χ^2 supports again the universality class of the 3-d Ising model.

The susceptibility and the four parameter fit are shown in Figure 6-1. Figure 6-2 shows the function $f(x)$.

Chapter 7

Chiral phase transition in a staggered fermion model

We now turn to the purely fermionic aspect of the sign problem and examine a model of staggered lattice fermions with a four-fermion interaction and $\mathbf{Z}(2)$ chiral symmetry using the Hamiltonian formulation in (3+1) and (2+1) dimensions. These models cannot be simulated with standard fermion algorithms because those suffer from a very severe sign problem. We use the meron-cluster algorithm technique to solve the sign problem and we obtain high-precision numerical data. The finite temperature chiral phase transition is investigated and it is verified to be in the universality class of the dimensionally reduced Ising model using finite-size scaling. The chapter is organized as follows. In section 7.1 we introduce the staggered fermion Hamiltonian, derive the path integral representation of the partition function, and discuss the fermion sign as well as relevant observables. Section 7.2 contains the description of the meron-cluster algorithm and the corresponding improved estimators. In section 7.3, we present the results of numerical simulations in (3+1) dimensions respectively and we extract the critical behavior from the finite-size scaling of the chiral susceptibility. In section 7.4 the numerical results for the (2+1) dimensional model are presented. Here we also consider the Binder cumulant to extract the critical behaviour.

7.1 The staggered fermion model

Let us consider staggered fermions hopping on a 3-d cubic spatial lattice with $V = L^3$ sites x (L even) and with periodic or antiperiodic spatial boundary conditions. (The (2+1)D case is analogous.) We start in the Hamiltonian formulation and then derive a path integral on a (3+1)-d Euclidean space-time lattice. The fermions are described by creation and annihilation operators Ψ_x^+ and Ψ_x with standard anticommutation relations

$$\{\Psi_x^+, \Psi_y^+\} = \{\Psi_x, \Psi_y\} = 0, \; \{\Psi_x^+, \Psi_y\} = \delta_{xy}. \tag{7.1}$$

The staggered fermion Hamilton operator takes the form

$$H = \sum_{x,i} h_{x,i} + m \sum_x (-1)^{x_1+x_2+x_3} \Psi_x^+ \Psi_x, \tag{7.2}$$

that is a sum of nearest-neighbor couplings $h_{x,i}$ and a mass term $m\overline{\chi}\chi$. In the following we work directly in the chiral limit, $m = 0$, and only use $\overline{\chi}\chi$ as an observable. The term $h_{x,i}$ couples the fermion operators at the lattice sites x and $x + \hat{i}$, where $\hat{i}$ is a unit-vector in the i-direction, and

$$h_{x,i} = \frac{1}{2}\eta_{x,i}(\Psi_x^+ \Psi_{x+\hat{i}} + \Psi_{x+\hat{i}}^+ \Psi_x) + G(\Psi_x^+ \Psi_x - \frac{1}{2})(\Psi_{x+\hat{i}}^+ \Psi_{x+\hat{i}} - \frac{1}{2}). \tag{7.3}$$

Here $\eta_{x,1} = 1$, $\eta_{x,2} = (-1)^{x_1}$ and $\eta_{x,3} = (-1)^{x_1+x_2}$ are the standard staggered fermion sign factors, and G is a four-fermion coupling constant. The system has a conserved fermion number

$$N = \sum_x \Psi_x^+ \Psi_x, \tag{7.4}$$

because $[H, N] = 0$. Besides the $U(1)$ fermion number symmetry, the model has a $\mathbf{Z}(2)$ chiral symmetry, which (up to a phase) simply shifts Ψ_x^+ and Ψ_x by one lattice spacing in all three directions. This changes the sign of $\overline{\chi}\chi$ but leaves the $m = 0$ Hamiltonian invariant. There are also other $\mathbf{Z}(2)$ symmetries which correspond

to discrete flavor transformations. For a detailed discussion of the symmetries of staggered fermions in the Hamiltonian formulation we refer to [72].

To construct a path integral for the partition function, we decompose the Hamilton operator into six terms $H = H_1 + H_2 + ... + H_6$, with

$$H_i = \sum_{\substack{x=(x_1,x_2,x_3) \\ x_i even}} h_{x,i}, \; H_{i+3} = \sum_{\substack{x=(x_1,x_2,x_3) \\ x_i odd}} h_{x,i}. \tag{7.5}$$

The individual contributions to a given H_i commute with each other, but two different H_i do not commute. Using the Suzuki-Trotter formula we express the fermionic partition function at inverse temperature β as

$$Z_f = \mathrm{Tr}[\exp(-\beta H)] = \lim_{M\to\infty} \mathrm{Tr}[\exp(-\epsilon H_1)\exp(-\epsilon H_2)...\exp(-\epsilon H_6)]^M. \tag{7.6}$$

We have introduced $6M$ Euclidean time slices with $\epsilon = \beta/M$ being the lattice spacing in the Euclidean time direction. Following Jordan and Wigner [86] we represent the fermion operators by Pauli matrices

$$\Psi_x^+ = \sigma_1^3\sigma_2^3...\sigma_{l-1}^3\sigma_l^+, \; \Psi_x = \sigma_1^3\sigma_2^3...\sigma_{l-1}^3\sigma_l^-, \; n_x = \Psi_x^+\Psi_x = \frac{1}{2}(\sigma_l^3 + 1), \tag{7.7}$$

with

$$\sigma_l^\pm = \frac{1}{2}(\sigma_l^1 \pm i\sigma_l^2), \; [\sigma_l^i, \sigma_m^j] = 2i\delta_{lm}\epsilon_{ijk}\sigma_l^k. \tag{7.8}$$

Here l labels the lattice point x. The Jordan-Wigner representation requires an ordering of the lattice points. For example, one can label the point $x = (x_1, x_2, x_3)$ (with $x_i = 0, 1, ..., L-1$) by $l = 1 + x_1 + x_2 L + x_3 L^2$. It should be pointed out that the Jordan-Wigner representation works in any dimension. In one dimension the lattice points are, of course, naturally ordered, but even in higher dimensions the physics is completely independent of the arbitrary ordering. We now insert complete sets of fermion Fock states between the factors $\exp(-\epsilon H_i)$. Each site is either empty

or occupied, i.e. n_x has eigenvalue 0 or 1. In the Pauli matrix representation this corresponds to eigenstates $|0\rangle$ and $|1\rangle$ of σ_l^3 with $\sigma_l^3|0\rangle = -|0\rangle$ and $\sigma_l^3|1\rangle = |1\rangle$. The transfer matrix is a product of factors

$$\exp(-\epsilon h_{x,i}) = \exp(\frac{\epsilon G}{4}) \begin{pmatrix} \exp(-\frac{\epsilon G}{2}) & 0 & 0 & 0 \\ 0 & \cosh\frac{\epsilon}{2} & \Sigma\sinh\frac{\epsilon}{2} & 0 \\ 0 & \Sigma\sinh\frac{\epsilon}{2} & \cosh\frac{\epsilon}{2} & 0 \\ 0 & 0 & 0 & \exp(-\frac{\epsilon G}{2}) \end{pmatrix}, \tag{7.9}$$

which is a 4×4 matrix in the Fock space basis $|00\rangle$, $|01\rangle$, $|10\rangle$ and $|11\rangle$ of two sites x and $x + \hat{i}$. Here $\Sigma = \eta_{x,i}\sigma_{l+1}^3\sigma_{l+2}^3 ... \sigma_{m-1}^3$ includes the local sign $\eta_{x,i}$ as well as a non-local string of Pauli matrices running over consecutive labels between l and m, where l labels the lattice point x and m labels $x + \hat{i}$. Note that Σ is diagonal in the occupation number basis.

The partition function is now expressed as a path integral

$$Z_f = \sum_n \text{Sign}[n] \exp(-S[n]), \tag{7.10}$$

over configurations of occupation numbers $n(x,t) = 0, 1$ on a $(3+1)$-d space-time lattice of points (x,t). The Boltzmann factor

$$\begin{aligned} \exp(-S[n]) \;=\; & \prod_{\substack{x=(x_1,x_2,x_3) \\ x_1 even, t=6m}} \exp\{-s[n(x,t), n(x+\hat{1},t), n(x,t+1), n(x+\hat{1},t+1)]\} \\ & \times \prod_{\substack{x=(x_1,x_2,x_3) \\ x_2 even, t=6m+1}} \exp\{-s[n(x,t), n(x+\hat{2},t), n(x,t+1), n(x+\hat{2},t+1)]\} \\ & \times \prod_{\substack{x=(x_1,x_2,x_3) \\ x_3 even, t=6m+2}} \exp\{-s[n(x,t), n(x+\hat{3},t), n(x,t+1), n(x+\hat{3},t+1)]\} \\ & \times \prod_{\substack{x=(x_1,x_2,x_3) \\ x_1 odd, t=6m+3)}} \exp\{-s[n(x,t), n(x+\hat{1},t), n(x,t+1), n(x+\hat{1},t+1)]\} \end{aligned}$$

$$\times \prod_{\substack{x=(x_1,x_2,x_3) \\ x_2 odd, t=6m+4}} \exp\{-s[n(x,t), n(x+\hat{2},t), n(x,t+1), n(x+\hat{2},t+1)]\}$$
$$\times \prod_{\substack{x=(x_1,x_2,x_3) \\ x_3 odd, t=6m+5}} \exp\{-s[n(x,t), n(x+\hat{3},t), n(x,t+1), n(x+\hat{3},t+1)]\}, \tag{7.11}$$

(with $m = 0, 1, ..., M-1$) is a product of space-time plaquette contributions with

$$\begin{aligned} \exp(-s[0,0,0,0]) &= \exp(-s[1,1,1,1]) = \exp(-\frac{\epsilon G}{2}), \\ \exp(-s[0,1,0,1]) &= \exp(-s[1,0,1,0]) = \cosh\frac{\epsilon}{2}, \\ \exp(-s[0,1,1,0]) &= \exp(-s[1,0,0,1]) = \sinh\frac{\epsilon}{2}. \end{aligned} \tag{7.12}$$

All the other Boltzmann weights are zero, which implies several constraints on allowed configurations. Note that here we have dropped the trivial overall factor $\exp(\epsilon G/4)$ that appeared in eq.(7.9).

The sign of a configuration, Sign$[n]$, also is a product of space-time plaquette contributions sign$[n(x,t), n(x+\hat{i},t), n(x,t+1), n(x+\hat{i},t+1)]$ with

$$\begin{aligned} &\text{sign}[0,0,0,0]) = \text{sign}[0,1,0,1]) = \text{sign}[1,0,1,0]) = \text{sign}[1,1,1,1]) = 1, \\ &\text{sign}[0,1,1,0]) = \text{sign}[1,0,0,1]) = \Sigma. \end{aligned} \tag{7.13}$$

It should be noted that Σ gets contributions from all lattice points with labels between l and m. This seems to make an evaluation of the fermion sign rather tedious. Also, it is not a priori obvious that Sign$[n]$ is independent of the arbitrarily chosen order of the lattice points. Fortunately, there is a simple way to compute Sign$[n]$, which is directly related to the Pauli exclusion principle and which is manifestly order-independent. In fact, Sign$[n]$ has a topological meaning. The occupied lattice sites define fermion world-lines which are closed around the Euclidean time direction. Of course, during their Euclidean time evolution fermions can interchange their

positions, and the fermion world-lines define a permutation of particles. The Pauli exclusion principle dictates that the fermion sign is just the sign of that permutation. If we work with antiperiodic spatial boundary conditions, Sign$[n]$ receives an extra minus-sign for every fermion world-line that crosses a spatial boundary. Figure 7-1 shows two configurations of fermion occupation numbers in $(1+1)$ dimensions. The first configuration corresponds to two fermions at rest and has Sign$[n] = 1$. In the second configuration two fermions interchange their positions with one fermion stepping over the spatial boundary. If one uses periodic spatial boundary conditions this configuration has Sign$[n] = -1$. Note that the same configuration would have Sign$[n] = 1$ when antiperiodic boundary conditions are used.

To be specific about the sign of a configuration, we discuss the contribution of each plaquette to Sign$[n]$ for the case of periodic spatial boundary conditions in figure 7-1. The left configuration is trivial, because only diagonal elements of the transfer matrix (7.9) appear, which all contribute factors $+1$ to Sign$[n]$. For the right configuration we have to choose an order of the spatial lattice points. As the example is in one spatial dimension, the points have a natural order as indicated by the numbers below the right configuration. Only the four non-diagonal plaquettes in the second and third row can contribute to Sign$[n]$, and for those we have to evaluate the string of Pauli-matrices Σ running over the labels between the two spatial points belonging to the plaquette. (Note that $\eta_{x,i} = 1$ in one spatial dimension.) For the three leftmost non-diagonal plaquettes, there are no sites labeled between the two interacting sites, so again the contribution is $+1$. The only plaquette contributing a factor -1 is the remaining plaquette indicated by a minus sign. For this plaquette we have to evaluate $\Sigma = \sigma_2^3 \sigma_3^3$, and as one of those sites is empty and the other occupied we get a contribution -1. These tedious considerations give, as expected, the same result as the evaluation of the sign of the permutation.

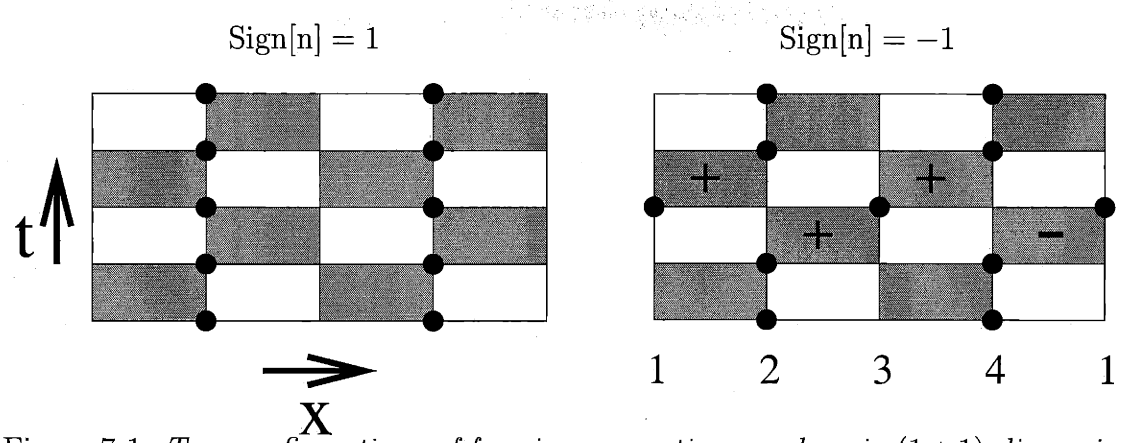

Figure 7-1: *Two configurations of fermion occupation numbers in* $(1+1)$ *dimensions. The shaded plaquettes carry the interaction. The dots represent occupied sites. In the second configuration two fermions interchange their positions. With periodic spatial boundary conditions this configuration has Sign*$[n] = -1$.

The expectation value of a fermionic observable $O[n]$ is given by

$$\langle O \rangle_f = \frac{1}{Z_f} \sum_n O[n] \text{Sign}[n] \exp(-S[n]). \tag{7.14}$$

Quantities of physical interest are the chiral condensate

$$\overline{\chi}\chi[n] = \frac{\epsilon}{6} \sum_{x,t} (-1)^{x_1+x_2+x_3} (n(x,t) - \frac{1}{2}), \tag{7.15}$$

and the corresponding chiral susceptibility

$$\chi = \frac{1}{\beta V} \langle (\overline{\Psi}\Psi)^2 \rangle_f. \tag{7.16}$$

Up to now we have derived a path integral representation for the fermion system in terms of bosonic occupation numbers and a fermion sign factor that encodes Fermi statistics. The system without the sign factor is bosonic and is characterized by the positive Boltzmann factor $\exp(-S[n])$. Here the bosonic model is a quantum spin

system with the Hamiltonian

$$H = \sum_{x,i} (S_x^1 S_{x+\hat{i}}^1 + S_x^2 S_{x+\hat{i}}^2 + G S_x^3 S_{x+\hat{i}}^3), \tag{7.17}$$

where $S_x^i = \frac{1}{2}\sigma_l^i$ is a spin 1/2 operator associated with the lattice site x that was labeled by l. The case $G = 1$ corresponds to the isotropic antiferromagnetic quantum Heisenberg model, $G = 0$ represents the quantum XY-model, and $G = -1$ corresponds to an isotropic ferromagnet. In the latter case a unitary transformation of the spin operators, which takes $S_x^1 \longrightarrow -S_x^1, S_x^2 \longrightarrow -S_x^2$ and $S_x^3 \longrightarrow S_x^3$ on even sites, and is the identity on odd sites, transforms (7.17) into the isotropic ferromagnet. In the language of the spin model, the chiral condensate turns into the staggered magnetization

$$\overline{\chi}\chi = \frac{\epsilon}{6} \sum_{x,t} (-1)^{x_1+x_2+x_3} S_x^3. \tag{7.18}$$

For sufficiently large G, for example in an antiferromagnet with $G = 1$, the staggered magnetization gets a non-zero expectation value at sufficiently low temperature, thus breaking the bosonic analog of chiral symmetry. It will turn out that the fermion sign does not change this behavior, and indeed chiral symmetry is spontaneously broken in the fermionic model as well.

7.2 The meron-cluster algorithm

Let us first discuss the nature of the fermion sign problem. The fermionic path integral $Z_f = \sum_n \mathrm{Sign}[n] \exp(-S[n])$ includes the fermion sign factor $\mathrm{Sign}[n] = \pm 1$ as well as a positive Boltzmann factor $\exp(-S[n])$ that contains the action $S[n]$ of the corresponding bosonic model with partition function $Z_b = \sum_n \exp(-S[n])$. This is a special case of the case discussed in section 4.1 where the Boltzmann factor was complex. Therefore the result carries over that even in an ideal simulation of the bosonic ensemble which generates N completely uncorrelated configurations, the

relative statistical error of the sign is

$$\frac{\Delta\text{Sign}}{\langle\text{Sign}\rangle} = \frac{\sqrt{\langle\text{Sign}^2\rangle - \langle\text{Sign}\rangle^2}}{\sqrt{N}\langle\text{Sign}\rangle} = \frac{\exp(\beta V \Delta f)}{\sqrt{N}}. \tag{7.19}$$

To determine the average sign with sufficient accuracy one needs to generate on the order of $N = \exp(2\beta V \Delta f)$ configurations. For large volumes and small temperatures this is impossible in practice. It is in the case of a sign problem possible to solve one half of the problem if one can match any contribution -1 with another contribution 1 to give 0, such that only a few unmatched contributions 1 remain. Then effectively $\text{Sign} = 0, 1$ and hence $\text{Sign}^2 = \text{Sign}$. This reduces the relative error to

$$\frac{\Delta\text{Sign}}{\langle\text{Sign}\rangle} = \frac{\sqrt{\langle\text{Sign}\rangle - \langle\text{Sign}\rangle^2}}{\sqrt{N'}\langle\text{Sign}\rangle} = \frac{\exp(\beta V \Delta f/2)}{\sqrt{N'}}. \tag{7.20}$$

One gains an exponential factor in statistics, but one still needs to generate $N' = \sqrt{N} = \exp(\beta V \Delta f)$ independent configurations in order to accurately determine the average sign. This is because one generates exponentially many vanishing contributions before one encounters a contribution 1. As explained below, in our cluster algorithm an explicit matching of contributions -1 and 1 is achieved using an improved estimator. This solves one half of the sign problem. In a second step involving a Metropolis decision, our algorithm ensures that contributions 0 and 1 occur with similar probabilities. This saves another exponential factor in statistics and solves the other half of the sign problem.

The meron-cluster fermion algorithm is based on a cluster algorithm for the corresponding bosonic model without the sign factor. Bosonic quantum spin systems can be simulated very efficiently with cluster algorithms [87, 88, 89]. The first cluster algorithm for lattice fermions was described in [90]. These algorithms can be implemented directly in the Euclidean time continuum [91], i.e. the Suzuki-Trotter discretization is not even necessary. The same is true for the meron-cluster algorithm. Here we discuss the algorithm for discrete time. The idea behind the algorithm is

to decompose a configuration into clusters which can be flipped independently. Each lattice site belongs to exactly one cluster. When the cluster is flipped, the occupation number of all the sites on the cluster is changed from $n(x,t)$ to $1-n(x,t)$, i.e. a cluster flip turns occupied into empty sites and vice versa. The decomposition of the lattice into clusters results from connecting neighboring sites on each individual space-time interaction plaquette following probabilistic cluster rules. A sequence of connected sites defines a cluster. In this case the clusters are sets of closed loops. The cluster rules are constructed to obey detailed balance. To show this we first write the plaquette Boltzmann factors as

$$\begin{aligned}
&\exp(-s[n(x,t),n(x+\hat{i},t),n(x,t+1),n(x+\hat{i},t+1)]) = \\
&A\delta_{n(x,t),n(x,t+1)}\delta_{n(x+\hat{i},t),n(x+\hat{i},t+1)} + B\delta_{n(x,t),1-n(x+\hat{i},t)}\delta_{n(x,t+1),1-n(x+\hat{i},t+1)} + \\
&C\delta_{n(x,t),n(x,t+1)}\delta_{n(x+\hat{i},t),n(x+\hat{i},t+1)}\delta_{n(x,t),1-n(x+\hat{i},t)} + D\delta_{n(x,t),n(x+\hat{i},t+1)}\delta_{n(x+\hat{i},t),n(x,t+1)} + \\
&E\delta_{n(x,t),n(x,t+1)}\delta_{n(x+\hat{i},t),n(x+\hat{i},t+1)}\delta_{n(x,t),n(x+\hat{i},t)}. \qquad (7.21)
\end{aligned}$$

The various δ-functions specify which sites are connected and thus belong to the same cluster. The quantities $A, B, ..., E$ determine the relative probabilities for different cluster break-ups of an interaction plaquette. We only allow break-ups which generate legal configurations under cluster flips. For example, A determines the probability with which sites are connected with their time-like neighbors, while B and D determine the probabilities for connections with space-like or diagonal neighbors, respectively. The quantities C and E determine the probabilities to put all four sites of a plaquette into the same cluster. This is possible for plaquette configurations $[0,1,0,1]$ or $[1,0,1,0]$ with a probability proportional to C and for configurations $[0,0,0,0]$ or $[1,1,1,1]$ with a probability proportional to E. The cluster rules are illustrated in table 7.1.

weight	configuration	break-ups
$\exp\left(-\frac{\epsilon G}{2}\right)$		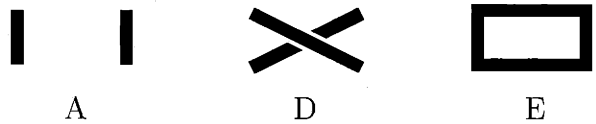 A D E
$\cosh\left(\frac{\epsilon}{2}\right)$	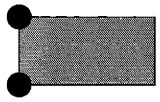	 A B C
$\sinh\left(\frac{\epsilon}{2}\right)$		 B D

Table 7.1: *Cluster break-ups of various plaquette configurations together with their relative probabilities $A, B, ..., E$. The dots represent occupied sites and the fat lines are the cluster connections.*

Inserting the expressions from eq.(7.12) one finds

$$\begin{aligned}
\exp(-s[0,0,0,0]) = \exp(-s[1,1,1,1]) = \exp(-\frac{\epsilon G}{2}) = A + D + E, \\
\exp(-s[0,1,0,1]) = \exp(-s[1,0,1,0]) = \cosh\frac{\epsilon}{2} = A + B + C, \\
\exp(-s[0,1,1,0]) = \exp(-s[1,0,0,1]) = \sinh\frac{\epsilon}{2} = B + D. \qquad (7.22)
\end{aligned}$$

For example, the probability to connect the sites with their time-like neighbors on a plaquette with configuration $[0,0,0,0]$ or $[1,1,1,1]$ is $A/(A+D+E)$, while the probability for a connection with their diagonal neighbor is $D/(A+D+E)$. All sites on such a plaquette are put into the same cluster with probability $E/(A+D+E)$. Similarly, the probability for connecting space-like neighbors on a plaquette with configuration $[0,1,1,0]$ or $[1,0,0,1]$ is $B/(B+D)$ and the probability for diagonal connections is $D/(B+D)$.

Eq.(7.21) can be viewed as a representation of the original model as a random

cluster model. The cluster algorithm operates in two steps. First, a cluster break-up is chosen for each space-time interaction plaquette according to the above probabilities. This effectively replaces the original Boltzmann weight of a plaquette configuration with a set of constraints represented by the δ-functions associated with the chosen break-up. The constraints imply that occupation numbers of connected sites can only be changed together. In the second step of the algorithm every cluster is flipped with probability 1/2. When a cluster is flipped the occupation numbers of all sites that belong to the cluster are changed. Eq.(7.22) ensures that the cluster algorithm obeys detailed balance. To determine $A, B, ..., E$ we distinguish three cases. For $G \geq 1$ we solve eq.(7.22) by

$$A = \exp(-\frac{\epsilon G}{2}),\ B = \sinh\frac{\epsilon}{2},\ C = \exp(-\frac{\epsilon}{2}) - \exp(-\frac{\epsilon G}{2}),\ D = E = 0. \tag{7.23}$$

For $-1 \leq G \leq 1$ we use

$$\begin{aligned} A &= \frac{1}{2}[\exp(-\frac{\epsilon G}{2}) + \exp(-\frac{\epsilon}{2})],\ B = \frac{1}{2}[\exp(\frac{\epsilon}{2}) - \exp(-\frac{\epsilon G}{2})],\ C = 0, \\ D &= \frac{1}{2}[\exp(-\frac{\epsilon G}{2}) - \exp(-\frac{\epsilon}{2})],\ E = 0, \end{aligned} \tag{7.24}$$

and, finally, for $G \leq -1$

$$A = \cosh\frac{\epsilon}{2},\ B = C = 0,\ D = \sinh\frac{\epsilon}{2},\ E = \exp(-\frac{\epsilon G}{2}) - \exp(\frac{\epsilon}{2}). \tag{7.25}$$

As an example, let us consider the antiferromagnetic quantum Heisenberg model, i.e. $G = 1$, and hence

$$A = \exp(-\frac{\epsilon}{2}),\ B = \sinh\frac{\epsilon}{2},\ C = D = E = 0. \tag{7.26}$$

Consequently, on plaquette configurations $[0,0,0,0]$ or $[1,1,1,1]$ one always chooses time-like connections between sites, and for configurations $[0,1,1,0]$ or $[1,0,0,1]$ one

always chooses space-like connections. For configurations $[0,1,0,1]$ or $[1,0,1,0]$ one chooses time-like connections with probability $p = A/(A+B) = 2/[1+\exp(\epsilon)]$ and space-like connections with probability $1-p = B/(A+B)$. Indeed, this is the algorithm that was used in [92]. It is extremely efficient, has almost no detectable autocorrelations, and its dynamical exponent for critical slowing down is compatible with zero.

Let us now consider the effect of a cluster flip on the fermion sign. It is obvious that the flip of a cluster can either change the sign of the configuration or leave it unchanged. In general, the effect of the flip of a specific cluster on the fermion sign can depend on the orientation of the spins in the other clusters. For example, a cluster whose flip does not change the sign for a given orientation of spins in the other clusters, may very well change the sign after other clusters have been flipped. In other words, the clusters affect each other in their effect on the fermion sign. This makes it very difficult to understand the effect of the various cluster flips on the topology of the fermion world-lines and thus on Sign$[n]$. As a consequence, for most models described above, it was unclear how to solve the fermion sign problem. However recently, a formula for the sign change due to the flip of a particular cluster in a fixed orientation of spins on the other clusters has been found [21]. The case of loop clusters, i.e. $C = E = 0$, is considered. Let N_w be the temporal winding of a loop, N_h the number of hops the loop makes from an occupied site to an empty site, N_D the number of D break-ups such that all the four sites are empty or occupied and are simultaneously part of the loop, and N'_D the number of D break-ups such that exactly two sites connected by a bond are part of the loop with the additional constraint that the other two sites are occupied. Then the flip of that loop changes the sign of the configuration if $(N_w + N_h + N_D + N'_D)$ is even and leaves it unchanged otherwise. This formula shows that the effect of cluster flips on Sign$[n]$ is dependent on the orientation of the spins in the other clusters through N'_D. Thus, if we ensure that $N'_D = 0$ the clusters have a definite effect on Sign$[n]$ when flipped, irrespective

of the orientations of the spins in the other clusters. This property is needed for an efficient improved estimator. It is possible to determine the sign of those clusters from their own internal structure, without examining spins from other clusters. A simple way to ensure the independence of clusters in their effect on Sign$[n]$ is to limit ourselves to models which have $D = 0$. According to eq.(7.23) this is possible for $G \geq 1$.

Once we forbid diagonal cluster break-ups, i.e. when $D = 0$, the clusters have a remarkable property with far reaching consequences: each cluster can then be characterized by its effect on the fermion sign independent of the orientation of all the other clusters. We refer to clusters whose flip changes Sign$[n]$ as merons, while clusters whose flip leaves Sign$[n]$ unchanged are called non-merons. The flip of a meron-cluster permutes the fermions and changes the topology of the fermion world-lines. The term meron has been used before to denote half-instantons. For example, the meron-clusters in the algorithm for the 2-d $O(3)$ model at non-zero vacuum angle θ are indeed half-instantons [14]. A configuration with an odd permutation of fermions has Sign$[n] = -1$ and can be viewed as an instanton, while a configuration with an even permutation of fermions is topologically trivial and has Sign$[n] = 1$. The flip of a meron-cluster changes an instanton into a topologically trivial configuration and therefore is a half-instanton. In $(2 + 1)$ dimensions particles can have any statistics. The anyon statistics is characterized by a phase factor $\exp(i\theta H)$, where H is the integer-valued Hopf number. In that case, the flip of a meron-cluster changes the Hopf number by one, and the meron is indeed a half-Hopf-instanton. The number of merons in a configuration is always even. This follows when one considers flipping all clusters, and thus changing the occupation of all lattice sites, which leaves the fermion sign unchanged. If the number of merons would be odd, flipping all clusters would change the fermion sign, which implies that the number of merons must be even. An example of a meron-cluster is given in figure 7-2, which contains the same fermion configurations as figure 7-1. When the meron-cluster is flipped the first configuration

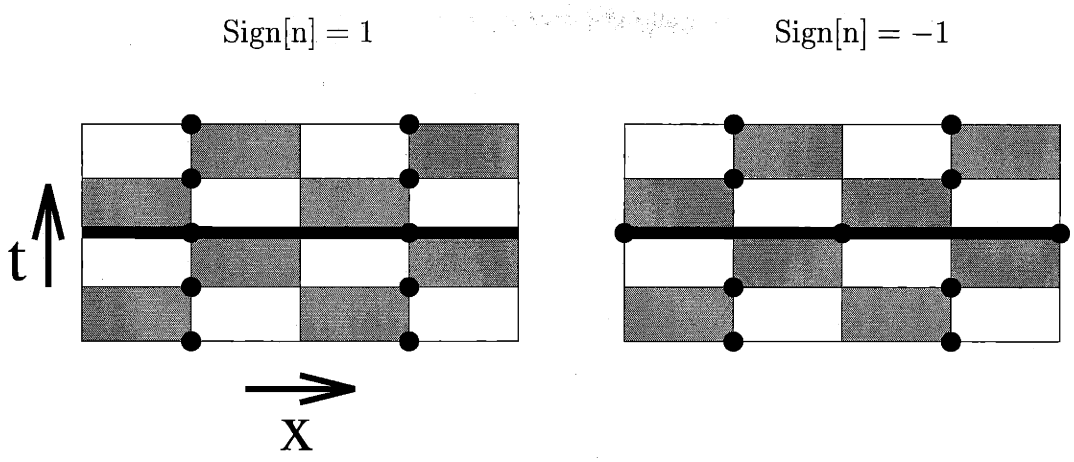

Figure 7-2: *The same fermion configurations as in figure 7-1 together with a meron-cluster represented by the fat line. The other clusters are not shown. Flipping the meron-cluster changes one configuration into the other and changes the fermion sign.*

with Sign$[n] = 1$ turns into the second configuration with Sign$[n] = -1$.

The meron concept alone allows us to gain an exponential factor in statistics. Since all clusters can be flipped independently, one can construct an improved estimator for Sign$[n]$ by averaging analytically over the 2^{N_C} configurations obtained by flipping the N_C clusters in the configuration in all possible ways. For configurations that contain merons the average Sign$[n]$ is zero because flipping a single meron leads to a cancellation of contributions ± 1. Hence, only the configurations without merons contribute to Sign$[n]$. The vast majority of configurations contains merons and now contributes an exact 0 to Sign$[n]$ instead of a statistical average of contributions ± 1. In this way the improved estimator leads to an exponential gain in statistics.

Still, as it stands it is not guaranteed that the contributions from the zero-meron sector will always be positive. With no merons in the configuration it is clear that the fermion sign remains unchanged under cluster flip, but one could still have Sign$[n] = -1$. Fortunately, there is a way to guarantee that Sign$[n] = 1$ in the zero-meron sector. In that case the contributions to Sign$[n]$ are 0 from configurations containing meron-clusters and 1 from configurations without merons. According to the previous

discussion, this solves one half of the fermion sign problem. Let us describe how one can make sure that a configuration without merons always has Sign$[n] = 1$. This is possible when one does not allow the cluster break-ups characterized by the amplitudes D and E in eq.(7.21). This again limits us to models with $G \geq 1$, for which we have $D = E = 0$ according to eq.(7.23). The remaining cluster break-ups with amplitudes A, B, C have a very important property. They guarantee that sites inside a cluster obey a pattern of staggered occupation, i.e. either the even sites (with $x_1 + x_2 + x_3$ even) within the cluster are all occupied and the odd sites are all empty, or the even sites are all empty and the odd sites are all occupied. This guarantees that the clusters can be flipped such that one reaches the totally staggered reference configuration in which at all times all even sites are occupied and all odd sites are empty. In the corresponding antiferromagnet this configuration represents a completely ordered state with a staggered magnetization. In the half-occupied reference configuration (which is the first configuration in figure 7-1) all fermions are at rest, no fermions are permuted during the Euclidean time evolution, and thus Sign$[n] = 1$. Since any configuration can be turned into the reference configuration by appropriate cluster flips, this is particularly true for configurations without merons. Since the totally staggered configuration has Sign$[n] = 1$ and the fermion sign remains unchanged when a non-meron-cluster is flipped, all configurations without merons have Sign$[n] = 1$. Instead of a sequence of ± 1 for Sign$[n]$, we now have contributions 0 and 1. As discussed before, this only solves one half of the fermion sign problem. Before we can solve the other half of the problem we must discuss improved estimators for the physical observables.

Let us consider an improved estimator for $(\overline{\chi}\chi[n])^2$Sign$[n]$ which is needed to determine the chiral susceptibility χ. The total chiral condensate, $\overline{\chi}\chi[n] = \sum_C \overline{\chi}\chi_C$, is a sum of cluster contributions

$$\overline{\chi}\chi_C = \frac{\epsilon}{6} \sum_{(x,t)\in C} (-1)^{x_1+x_2+x_3} (n(x,t) - \frac{1}{2}). \tag{7.27}$$

When a cluster is flipped, its condensate contribution changes sign. In a configuration without merons, where $\mathrm{Sign}[n] = 1$ for all relative cluster flips, the average of $(\overline{\chi}\chi[n])^2\mathrm{Sign}[n]$ over all 2^{N_C} configurations is $\sum_C |\overline{\chi}\chi_C|^2$. For configurations with two merons the average is $2|\overline{\chi}\chi_{C_1}||\overline{\chi}\chi_{C_2}|$ where C_1 and C_2 are the two meron-clusters. Configurations with more than two merons do not contribute to $(\overline{\chi}\chi[n])^2\mathrm{Sign}[n]$. The improved estimator for the susceptibility is hence given by

$$\chi = \frac{\langle \sum_C |\overline{\chi}\chi_C|^2 \delta_{N,0} + 2|\overline{\chi}\chi_{C_1}||\overline{\chi}\chi_{C_2}|\delta_{N,2}\rangle}{V\beta\langle\delta_{N,0}\rangle}, \tag{7.28}$$

where N is the number of meron-clusters in a configuration. Thus, to determine χ one must only sample the zero- and two-meron sectors.

The probability to find a configuration without merons is exponentially small in the space-time volume since it is equal to $\langle\mathrm{Sign}\rangle$. Thus, although we have increased the statistics tremendously with the improved estimators, without a second step one would still need an exponentially large statistics to accurately determine χ. Fortunately, the numerator in equation (7.28) receives contributions from the zero- and two-meron sectors only, while the denominator gets contributions only from the zero-meron sector. One can hence restrict oneself to the zero- and two-meron sectors and never generate configurations with more than two merons. This enhances both the numerator and the denominator by a factor that is exponentially large in the volume, but leaves the ratio of the two invariant. One purpose of the second step of the meron-cluster algorithm is to eliminate all configurations with more than two merons. To achieve this, we start with an initial configuration with zero or two merons. For example, a completely occupied configuration has no merons. We then visit all plaquette interactions one after the other and choose new pair connections between the four sites according to the above cluster rules. If the new connection increases the number of merons beyond two, it is not accepted and the old connection is kept for that plaquette. This procedure obeys detailed balance because configurations with

more than two merons do not contribute to the observable we consider. This simple reject step eliminates almost all configurations with weight 0 and is the essential step to solve the other half of the fermion sign problem.

Assuming a dilute gas of meron and non-meron-clusters of typical space-time volume $|C|$ one finds a ratio $p(0)/p(2) \propto (|C|/V\beta)^2$ of the probabilities $p(0)$ and $p(2)$ to have zero or two merons. Hence, as long as the cluster size does not grow with the space-time volume, most configurations would have two merons and therefore would still have weight 0. Without further improvements, one would still need statistics quadratic (but no longer exponential) in the space-time volume to get an accurate average sign. The remaining problem can be solved with a reweighting technique similar to the one used in [14]. To enhance the zero-meron configurations in a controlled way, we introduce trial probabilities $p_t(0)$ and $p_t(2)$ which determine the relative weight of the zero- and two-meron sector. The trial distribution $p_t(N)$ for $N > 2$ is set to infinity. The distribution $p_t(N)$ is used in a Metropolis accept-reject step for the newly proposed pair connection on a specific plaquette interaction. A new pair connection that changes the meron number from N to N' is accepted with probability $p = \min[1, p_t(N)/p_t(N')]$. In particular, configurations with $N' > 2$ are never generated because then $p_t(N') = \infty$ and $p = 0$. After visiting all plaquette interactions, each cluster is flipped with probability $1/2$ which completes one update sweep. After reweighting, the zero- and two-meron configurations appear with similar probabilities. This completes the second step in our solution of the fermion sign problem. The reweighting of the zero- and two-meron configurations is taken into account in the final expression for the chiral susceptibility as

$$\chi = \frac{\langle \sum_C |\overline{\chi}\chi_C|^2 \delta_{N,0}\, p_t(0) + 2|\overline{\chi}\chi_{C_1}||\overline{\chi}\chi_{C_2}|\delta_{N,2}\, p_t(2)\rangle}{V\beta\langle \delta_{N,0}\, p_t(0)\rangle}. \tag{7.29}$$

The optimal ratio $p_t(0)/p_t(2)$, which minimizes the statistical error of χ, can be estimated by gradually increasing the volume and the inverse temperature to their

L	β	$\langle \text{Sign} \rangle$	$p_t(0)/p_t(2)$	$\langle \text{Sign} \rangle_r$	χ
4	0.6	0.838(1)	0.5/0.5	0.845(1)	0.554(1)
4	0.7	0.710(3)	0.5/0.5	0.726(2)	0.936(2)
4	0.8	0.534(4)	0.5/0.5	0.566(2)	1.678(5)
4	0.9	0.357(3)	0.5/0.5	0.405(2)	3.13(1)
4	0.948	0.282(2)	0.3/0.7	0.537(3)	4.22(2)
6	0.948	0.0556(7)	0.2/0.8	0.398(3)	9.83(8)
8	0.948	0.0020(4)	0.1/0.9	0.361(8)	16.6(5)
10	0.948	—	0.1/0.9	0.178(3)	26.5(8)
12	0.948	—	0.05/0.95	0.17(1)	37(1)
14	0.948	—	0.02/0.98	0.20(1)	51(1)
16	0.948	—	0.01/0.99	0.22(2)	65(2)

Table 7.2: *Numerical results for the non-reweighted $\langle Sign \rangle$, the reweighted $\langle Sign \rangle_r$ and χ obtained with a reweighting factor $p_t(0)/p_t(2)$ on lattices of spatial size L at inverse temperature β. For the larger volumes the non-reweighted $\langle Sign \rangle$ is too small to be measured.*

desired values.

7.3 Numerical results in (3+1)D

We have simulated the staggered fermion model with $G = 1$ on antiperiodic spatial volumes L^3 with $L = 4, 6, ..., 16$ and at various inverse temperatures $\beta \in [0.5, 1.2]$ which includes the critical point. In the Euclidean time direction we have used $M = 4$, i.e. 24 time-slices. In all cases, we have performed at least 1000 thermalization sweeps followed by 10000 measurements. One sweep consists of a new choice of the cluster connections on each interaction plaquette and a flip of each cluster with probability 1/2. To estimate an optimal ratio $p_t(0)/p_t(2)$ of the reweighting probabilities, we have first performed runs without reweighting. The observed relative probabilities of the zero- and two-meron sectors were used as an estimate for $p_t(0)/p_t(2)$ in production runs. Especially for the larger volumes, reweighting is necessary in order to obtain accurate results.

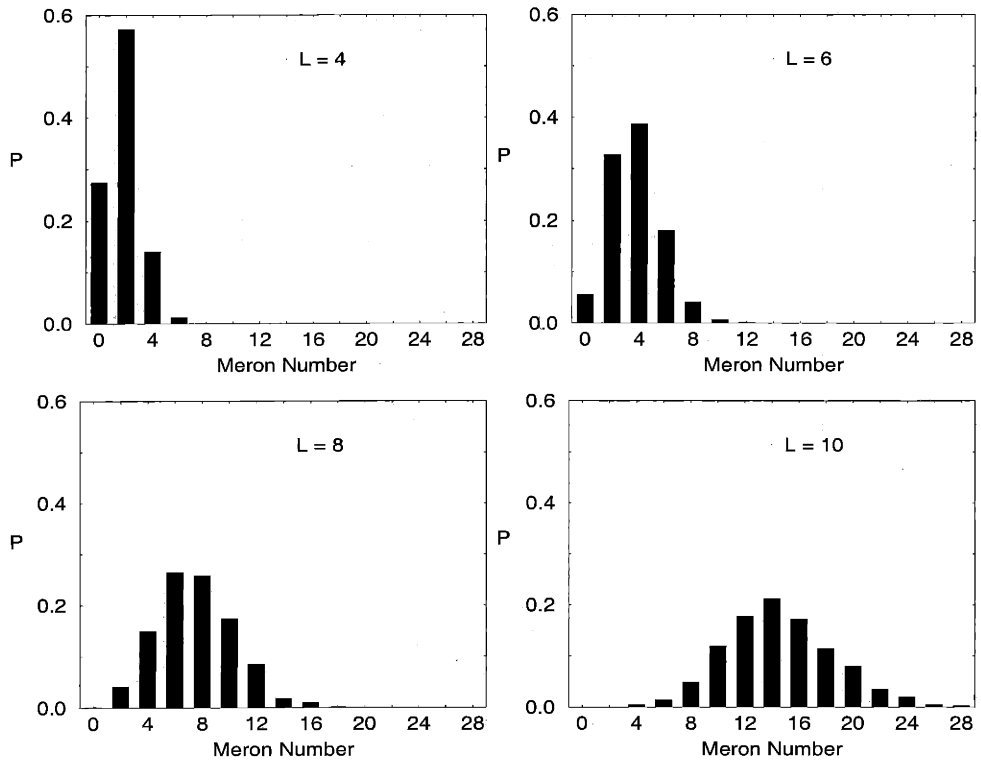

Figure 7-3: *The probability of having a certain number of merons for various spatial sizes* $L = 4, 6, 8$ *and* 10 *at* $\beta = 0.948$.

Some of our data for the chiral susceptibility χ are contained in table 7.2. The table also includes the non-reweighted $\langle \text{Sign} \rangle$, the value of the used reweighting factor $p_t(0)/p_t(2)$ as well as the reweighted $\langle \text{Sign} \rangle_r$. Note that $\langle \text{Sign} \rangle_r$ is the fraction of zero-meron configurations that the algorithm generates by sampling the zero- and two-meron sectors only. This quantity is typically a lot bigger than the original non-reweighted $\langle \text{Sign} \rangle$, which is the fraction of zero-meron configurations in the space of all configurations including those with many merons. In particular, in large space-time volumes the staggered fermion model suffers from a very severe sign problem.

Figure 7-3 shows the probability to have a certain number of merons in an algorithm that samples all meron-sectors without reweighting. For small volumes the zero-meron sector and hence $\langle \text{Sign} \rangle$ are relatively large, while multi-meron configura-

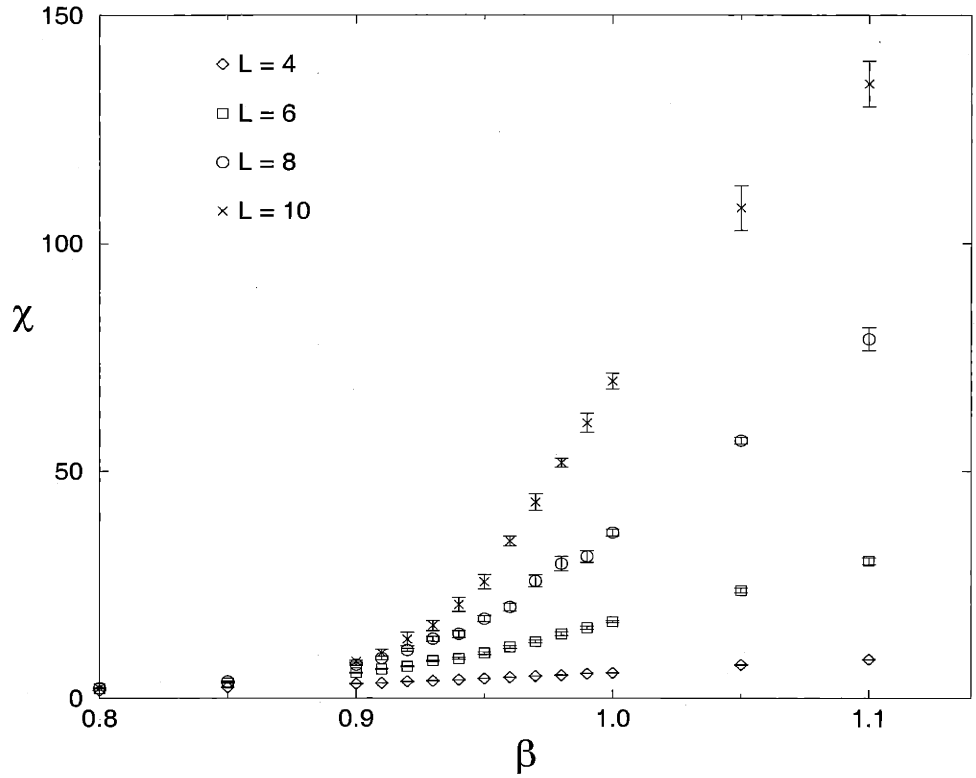

Figure 7-4: *The chiral susceptibility χ as a function of the inverse temperature β for various spatial sizes $L = 4, 6, 8$ and 10.*

tions are rare. On the other hand, in larger volumes the vast majority of configurations has a large number of merons and hence $\langle \text{Sign} \rangle$ is exponentially small. For example, an extrapolation from smaller volumes gives a rough estimate for the non-reweighted $\langle \text{Sign} \rangle \approx 10^{-20}$ on the 16^3 lattice at $\beta = 0.948$, while the reweighted $\langle \text{Sign} \rangle_r = 0.22(2)$. Hence, to achieve a similar accuracy without the meron-cluster algorithm one would have to increase the statistics by a factor 10^{40}, which is obviously impossible in practice. In fact, at present there is no other method that can be used to simulate this model.

Figure 7-4 shows the chiral susceptibility χ as a function of β for various spatial sizes L. At high temperatures (small β) χ is almost independent of the volume, indicating that chiral symmetry is unbroken. On the other hand, at low temperatures

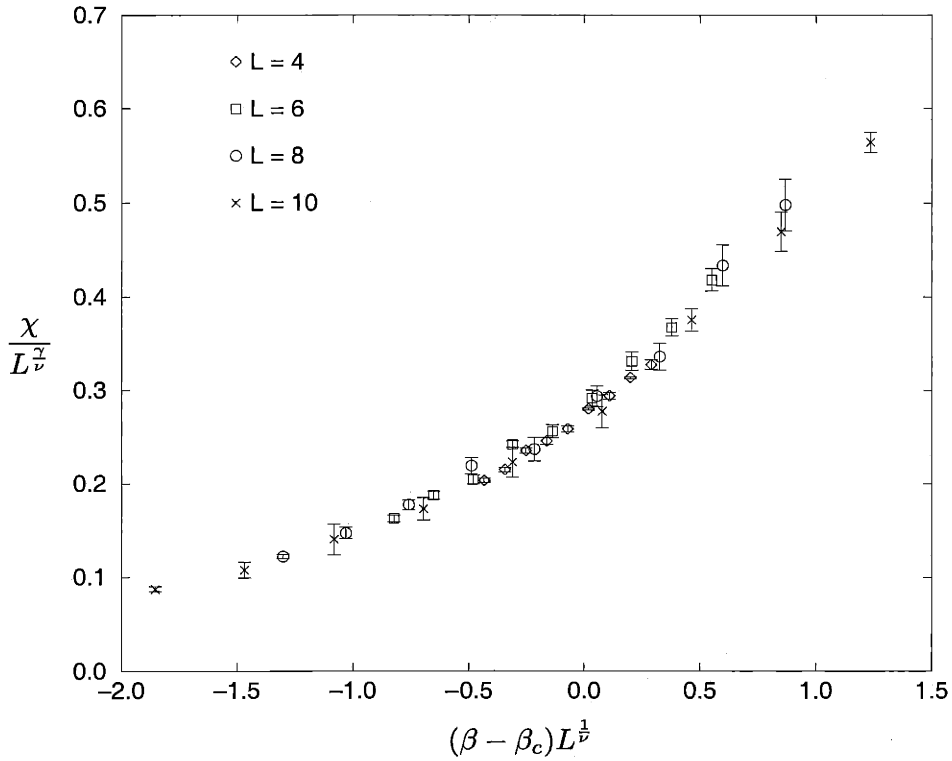

Figure 7-5: *Finite-size scaling behavior of the chiral susceptibility* χ. *The data for various spatial sizes* $L = 4, 6, 8$ *and* 10 *fall on one universal curve.*

χ increases with the volume, which implies that chiral symmetry is spontaneously broken. To study the critical behavior in detail, we have performed a finite-size scaling analysis for χ focusing on a narrow range $\beta \in [0.9, 0.98]$ around the critical point. Since a $\mathbf{Z}(2)$ chiral symmetry gets spontaneously broken at finite temperature in this (3+1)-d model, one expects to find the critical behavior of the 3-d Ising model. The corresponding finite-size scaling formula valid close to β_c is [85]

$$\begin{aligned} &\chi(L,\beta) = a(x) + b(y)L^{\gamma/\nu}, \\ &a(x) = a_0 + a_1 x + a_2 x^2 + ..., \ x = \beta - \beta_c, \\ &b(y) = b_0 + b_1 y + b_2 y^2 + ..., \ y = (\beta - \beta_c)L^{1/\nu}. \end{aligned} \tag{7.30}$$

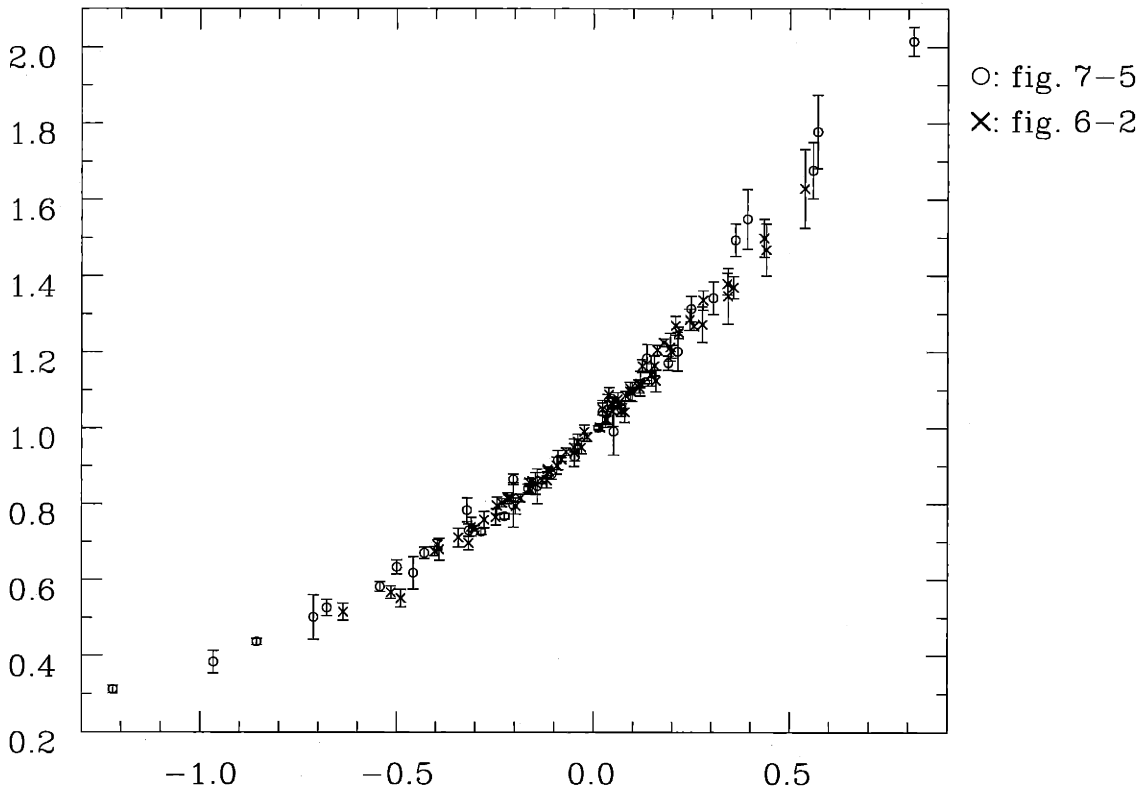

Figure 7-6: *The data from figures 6-2 and 7-5 appropriately rescaled to have* $f(0) = f'(0) = 1$.

For the 3-d Ising model the critical exponents are given by $\nu = 0.630(1)$ and $\gamma/\nu = 1.963(3)$ [85]. Fitting our data, we find $\nu = 0.63(4)$ and $\gamma/\nu = 1.98(2)$, which indicates that the chiral transition of the staggered fermion model is indeed in the 3-d Ising universality class. The fit gives $\beta_c = 0.948(3)$. In figure 7-5 we have taken the values of the critical exponents from the 3-d Ising model, and we have plotted $\chi/L^{\gamma/\nu}$ as a function of $y = (\beta - \beta_c)L^{1/\nu}$. For large enough L one can neglect the term $a(x)$ in eq.(7.30) and one obtains $\chi/L^{\gamma/\nu} = b(y)$. We have varied the value of β_c and found that indeed all data can be collapsed on one universal curve. The resulting critical inverse temperature is $\beta_c = 0.948(3)$ in agreement with the previous fit. The curve looks different from the analogous curve for the Potts model in figure

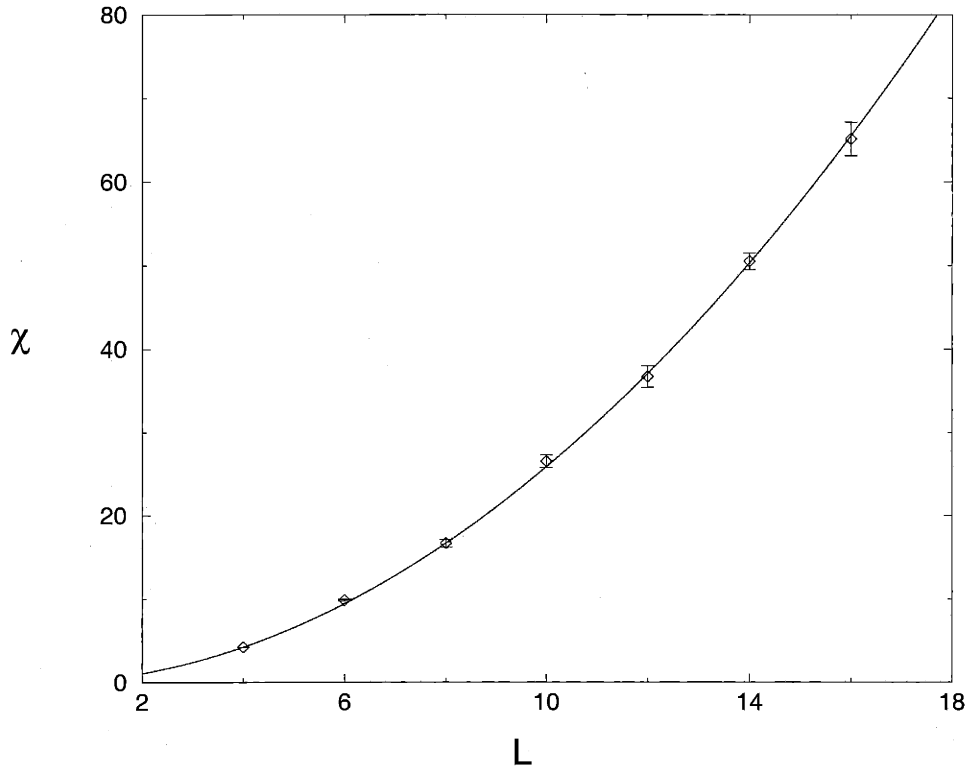

Figure 7-7: *Finite-size scaling behavior of the chiral susceptibility χ as a function of the spatial size L at the estimated critical inverse temperature $\beta_c = 0.948$. A fit of the volume-dependence (solid line) gives the critical exponent $\gamma/\nu = 1.98(2)$ of the 3-d Ising model.*

6-2, because there are two nonuniversal rescaling parameters between two different models in the same universality class. In particular one curve is increasing and the other is decreasing, because in one case the broken phase corresponds to positive arguments and in the other case it corresponds to negative arguments. In figure 7-6, the data from figures 7-5 and 6-2 are plotted after rescaling them appropriately to insure that the value and the first dervative of the function at $x = 0$ are both 1. We see excellent agreement between the two data sets. At the estimated value of β_c, we have performed simulations on larger spatial volumes up to 16^3. The results for χ are shown in figure 7-7 together with a fit that gives an independent estimate of $\gamma/\nu = 1.98(2)$. All of this supports the claim that the chiral transition in our model

is Ising-like.

7.4 Numerical results in (2+1)D

Now we apply the meron-cluster algorithm developed for the staggered fermion model in section 7.2 to the same model in 2+1 dimensions with $N = 1$ flavor. Various features of the model and the Meron-Cluster algorithm are identical to the case of 3 spatial dimensions. It has a severe sign problem too and cannot be explored using standard algorithms. We find that the $\mathbf{Z}(2)$ chiral symmetry of this model is spontaneously broken at low temperatures and that the finite-temperature chiral phase transition is in the universality class of the 2-d Ising model, as expected. Here we also construct and measure an observable that requires the exploration of the four-meron sector, namely the fourth order Binder cumulant. In [34] it has been verified that the chiral phase transition in a $(2+1)$-d four-fermion interaction model with $N = 4$ flavors and $\mathbf{Z}(2)$ chiral symmetry is in the universality class of the 2-d Ising model. Due to the fermion sign problem, standard fermion simulation methods often do not work in models with too small a number of flavors. The work presented here shows that the same universal behavior holds for $N = 1$ flavor. The quantities of physical interest which we measure are the chiral condensate $\overline{\chi}\chi$, the chiral susceptibility χ and a Binder cumulant U of the chiral condensate, respectively. U is given by

$$U = 1 - \frac{\langle(\overline{\chi}\chi)^4\rangle_f}{3[\langle(\overline{\chi}\chi)^2\rangle_f]^2}, \tag{7.31}$$

$$\text{where} \qquad \overline{\chi}\chi[n] = \frac{\epsilon}{4}\sum_{x,t}(-1)^{x_1+x_2}(n(x,t) - \frac{1}{2}).$$

We construct improved estimators for the Binder cumulant U now. For the Binder cumulant, we need to measure $\langle(\overline{\chi}\chi)^4\rangle_f$ and hence

$$\langle \text{Sign}(\overline{\chi}\chi)^4\rangle = \langle \text{Sign} \sum_{C_i,C_j,C_k,C_l} \overline{\chi}\chi_{C_i}\overline{\chi}\chi_{C_j}\overline{\chi}\chi_{C_k}\overline{\chi}\chi_{C_l}\rangle. \tag{7.32}$$

A cluster's condensate contribution $\overline{\chi}\chi_C$ changes sign when the cluster is flipped. When a meron-cluster is flipped, Sign is changed. The non-zero terms in $\langle \mathrm{Sign}(\overline{\chi}\chi)^4 \rangle$ do not change sign if any cluster in the configuration is flipped. These non-zero terms must contain odd powers of $\overline{\chi}\chi_C$ for all merons C in the configuration and even powers of $\overline{\chi}\chi_{C'}$ for all non-merons C'. The average over the ensemble of 2^{N_C} configurations is

$$\begin{aligned}\langle \mathrm{Sign}(\overline{\chi}\chi)^4 \rangle_{2^{N_C}} &= \delta_{N,0}\left[\sum_C |\overline{\chi}\chi_C|^4 + 6\sum_{C,C'} |\overline{\chi}\chi_C|^2 |\overline{\chi}\chi_{C'}|^2\right] \\ &+\delta_{N,2}\left[4|\overline{\chi}\chi_{C_1}|^3|\overline{\chi}\chi_{C_2}| + 4|\overline{\chi}\chi_{C_2}|^3|\overline{\chi}\chi_{C_1}| + 12\sum_C |\overline{\chi}\chi_C|^2|\overline{\chi}\chi_{C_1}||\overline{\chi}\chi_{C_2}|\right] \\ &+\delta_{N,4}\left[24|\overline{\chi}\chi_{C_1}||\overline{\chi}\chi_{C_2}||\overline{\chi}\chi_{C_3}||\overline{\chi}\chi_{C_4}|\right],\end{aligned} \tag{7.33}$$

where N is the number of merons in the configurations, C_1, C_2, C_3 and C_4 are the merons and all sums in eq.(7.33) are over non-meron clusters. This average only gets contributions from the zero-, two- and four-meron sectors and so we need only explore this sub-space. We average this quantity over the complete bosonic ensemble to measure $\langle \mathrm{Sign}(\overline{\chi}\chi)^4 \rangle$ and hence U.

We have performed simulations on lattices with antiperiodic spatial boundary conditions from $L = 4$ up to $L = 30$ at inverse temperatures in the range $\beta \in [1.0, 3.0]$, which includes the critical temperature where the chiral symmetry is spontaneously broken. We have made separate runs with either a fixed number of time slices (typically $M = 10$, i.e. 40 time slices) or with fixed lattice spacing in the time direction ($\epsilon = 0.1$). In each simulation, we have made at least 1000 thermalization sweeps followed by 10000 measurements, with these numbers increased by a factor of 10 for $L \leq 10$. In one sweep of the lattice, a new cluster connection is proposed on each interaction plaquette and each cluster is flipped with probability 1/2. To find the optimal reweighting probabilities $p_t(N)$ which minimize the statistical error, we proceed as in the (3+1)D case. We first make a sample run without reweighting, only

L	β	$\langle \text{Sign} \rangle$	χ	$p_t(0)/p_t(2)$	$\langle \text{Sign} \rangle_r$	χ_r
8	1.0	0.804(5)	0.829(3)	0.5/0.5	0.820(7)	0.826(6)
8	1.5	0.465(9)	2.84(3)	0.5/0.5	0.52(1)	2.84(4)
8	2.0	0.214(6)	9.2(2)	0.3/0.7	0.474(9)	9.0(1)
8	2.4	0.140(4)	16.6(3)	0.2/0.8	0.501(9)	16.4(3)
10	2.4	0.057(3)	24.8(6)	0.2/0.8	0.369(8)	24.2(5)
12	2.4	0.0203(8)	33(1)	0.1/0.9	0.443(7)	34.0(7)
14	2.4	0.0052(6)	41(4)	0.1/0.9	0.338(8)	44(1)
16	2.4	0.0005(2)	80(40)	0.075/0.925	0.314(4)	57(1)
20	2.4	—	—	0.03/0.97	0.355(9)	82(3)
24	2.4	—	—	0.01/0.99	0.46(1)	120(5)
28	2.4	—	—	0.01/0.99	0.329(9)	156(8)

Table 7.3: *Numerical results for the non-reweighted $\langle Sign \rangle$ and susceptibility χ measured over all meron sectors, and the reweighted $\langle Sign \rangle_r$ and χ_r measured over the zero- and two-meron sectors only with a reweighting factor $p_t(0)/p_t(2)$. For the larger volumes, $\langle Sign \rangle$ and χ cannot be measured.*

exploring the relevant meron-sectors. The observed relative weights are then used in production runs, where the sectors appear with equal probability. The major part of the sign problem is removed by the improved estimators, but reweighting is necessary for accurate measurements in large volumes.

A sample of the data measured is given in Table 7.3. The Table contains $\langle \text{Sign} \rangle$ and the susceptibility χ measured over all meron-sectors, and the reweighted $\langle \text{Sign} \rangle_r$ and χ_r measured over the zero- and two-meron sectors only with the reweighting factor $p_t(0)/p_t(2)$. (In these runs we have restricted the simulation to the zero- and two-meron sectors. In later simulations where we measure the Binder cumulant, we also include the four-meron sector.) All of these data are produced with 1000 thermalization sweeps and 10000 measurements. As all of the contributions to χ come from the zero- and two-meron sectors, χ and χ_r should be identical. Note that $\langle \text{Sign} \rangle_r$, the fraction of zero-meron configurations generated by sampling the zero- and two-meron sectors only, is typically a lot bigger than $\langle \text{Sign} \rangle$, the fraction of zero-meron configurations generated over all meron sectors. In small space-time volumes, χ can

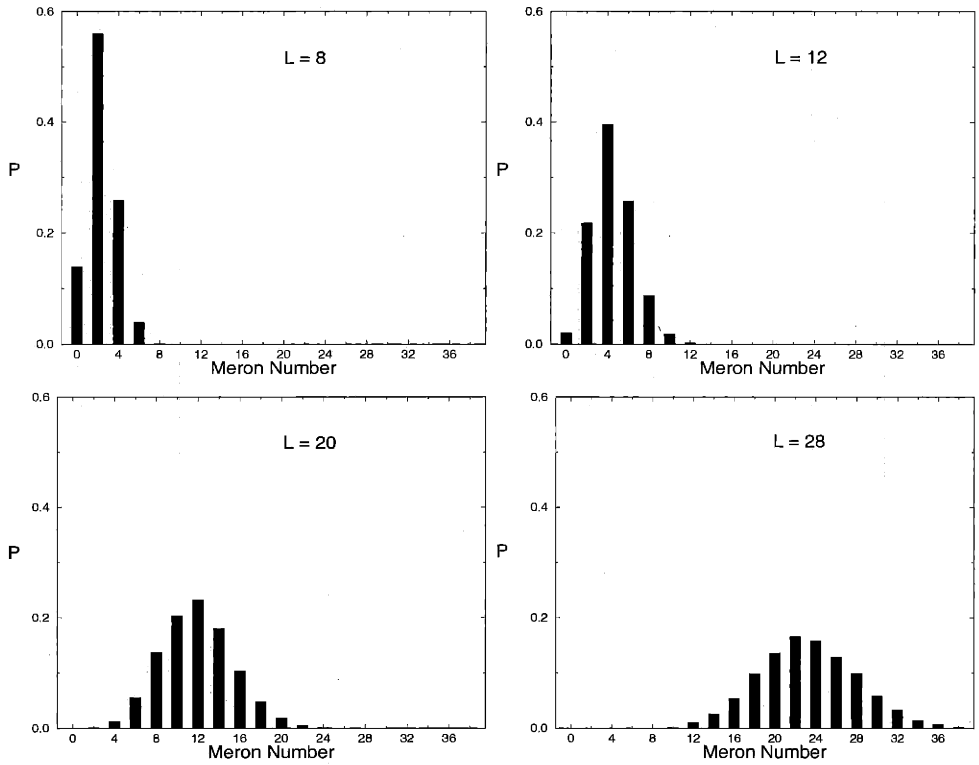

Figure 7-8: *The meron number probability distribution for various spatial sizes* $L = 8, 12, 20$ *and* 28 *at* $\beta = 2.4$.

be accurately measured even when sampling all meron sectors. However, in large space-time volumes, $\langle \text{Sign} \rangle$ is too small to be measured and we can only determine the susceptibility by restricting ourselves to the zero- and two-meron sectors. The (2+1)D staggered fermion model suffers from a very severe sign problem, just as the (3+1)D model, which is solved by the Meron-Cluster algorithm.

Figure 7-8 shows the meron number probability distribution in an algorithm that samples all meron sectors without reweighting. Again we observe the same situation as in the (3+1)D case: For small volumes the zero-meron sector and hence $\langle \text{Sign} \rangle$ are relatively large, while multi-meron configurations are rare. On the other hand, in larger volumes the vast majority of configurations has a large number of merons and hence $\langle \text{Sign} \rangle$ is exponentially small. For example, an extrapolation from smaller

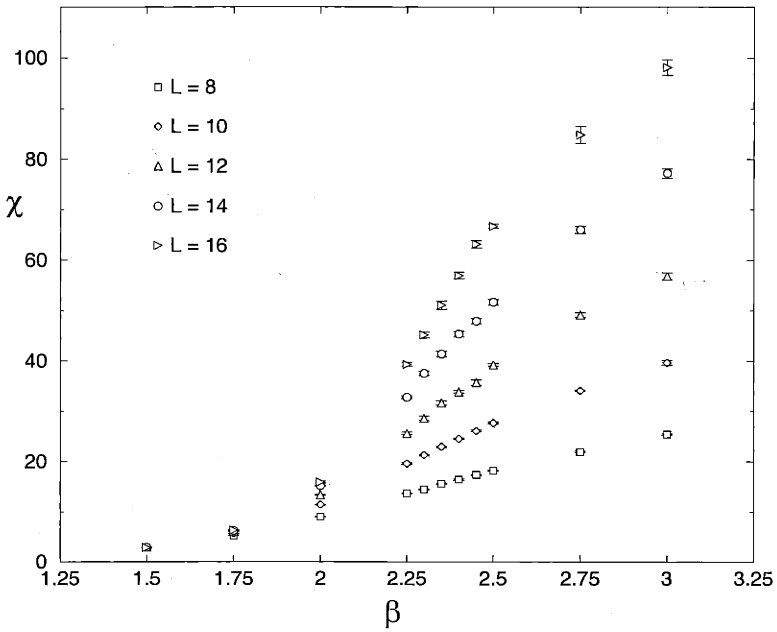

Figure 7-9: *The chiral susceptibility χ as a function of the inverse temperature β for various spatial sizes $L = 8, 10, 12, 14$ and 16 on lattices with 40 time slices. The chiral symmetry is intact at small β and spontaneously broken at large β.*

volumes gives a rough estimate for the non-reweighted $\langle \text{Sign} \rangle \approx 10^{-9}$ on the $L = 28$ lattice at $\beta = 2.4.$, while the reweighted $\langle \text{Sign} \rangle_r = 0.329(9)$. Even if the configurations are entirely uncorrelated, to achieve a similar accuracy without the meron-cluster algorithm one would have to increase the statistics by a factor 10^{18}, which is obviously impossible. In fact, at present there is no other method that can be used to simulate this model.

Figure 7-9 shows the chiral susceptibility χ as a function of β for various spatial sizes L. At high temperatures (small β) χ is almost independent of the volume, indicating that chiral symmetry is intact. On the other hand, at low temperatures (large β) χ increases with the volume, which implies that chiral symmetry is spontaneously broken. To study the critical behavior in detail, we have performed a finite-size scaling analysis for χ focusing on the range $\beta \in [2.2, 2.6]$ around the critical point. Since a $\mathbf{Z}(2)$ chiral symmetry is spontaneously broken at finite temperature in this

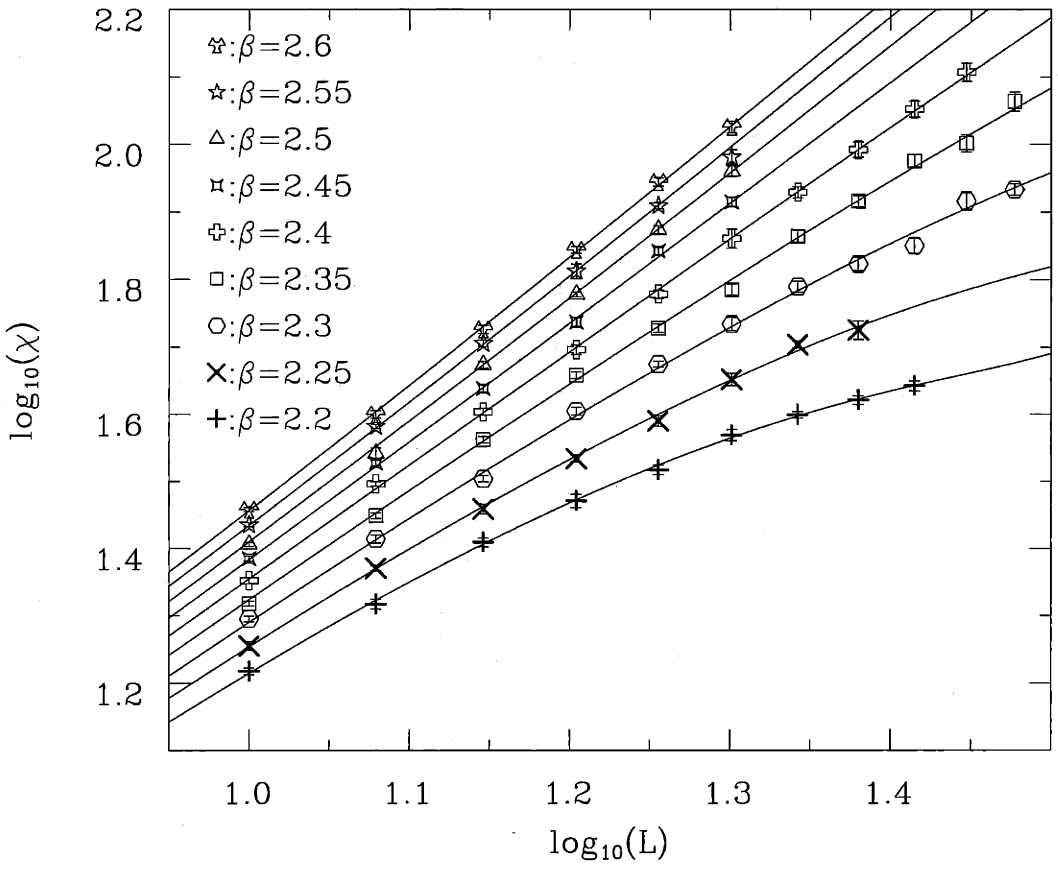

Figure 7-10: *The chiral susceptibility plotted against L for various values of β computed with $\epsilon = 0.1$. The fit is to the finite-size scaling formula (7.34) with $a(x)$ expanded to first order and $b(y)$ expanded to third order. The exponents are set to the 2-d Ising model values. All curves are obtained from one fit. The χ^2 per degree of freedom is 0.84 indicating a good agreement of our data with the finite-size scaling ansatz and 2-d Ising model critical exponents.*

$(2+1)$-d model, one expects to find the critical behavior of the 2-d Ising model. The corresponding finite-size scaling formula valid close to β_c is [85]

$$\begin{aligned} &\chi(L,\beta) = a(x) + b(y)L^{\gamma/\nu}, \\ &a(x) = a_0 + a_1 x + a_2 x^2 + ..., \ x = \beta - \beta_c, \\ &b(y) = b_0 + b_1 y + b_2 y^2 + ..., \ y = (\beta - \beta_c)L^{1/\nu}. \end{aligned} \tag{7.34}$$

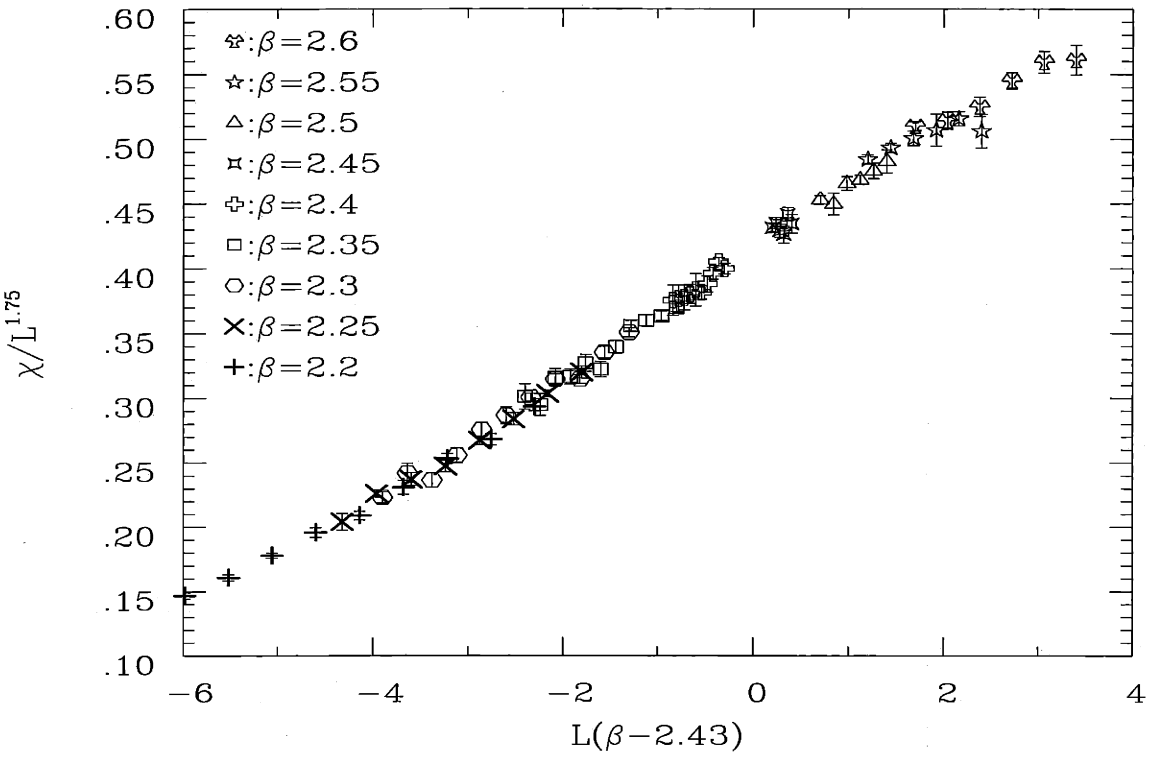

Figure 7-11: *Finite-size scaling behavior of the chiral susceptibility χ. The data for various spatial sizes L and inverse temperatures β fall on one universal curve.*

For the 2-d Ising model the critical exponents are given by $\nu = 1$ and $\gamma/\nu = 7/4$. Assuming these values for the exponents, we obtain $\beta_c = 2.43(1)$ for fixed $\epsilon = 0.1$ from the finite-size scaling fit, with a chi squared per degree of freedom of 0.84. The fit of the data is plotted in Figure 7-10. The value of β_c is slightly dependent on ϵ.

In the finite-size scaling equation (7.34), for large enough L one can neglect the term $a(x)$. Then $\chi/L^{\gamma/\nu}$ is a function of $y = (\beta - \beta_c)L^{1/\nu}$ alone, i.e. the susceptibility data in various volumes at various β can be described by one universal function. We have varied the value β_c to find if all the data can be collapsed onto one universal curve. In Figure 7-11, the universal curve is plotted obtained by taking $\beta_c = 2.43$. The excellent agreement over a large range of spatial volumes L and inverse temperatures β is an indication of the quality of the finite-size scaling fit. In principle it should be

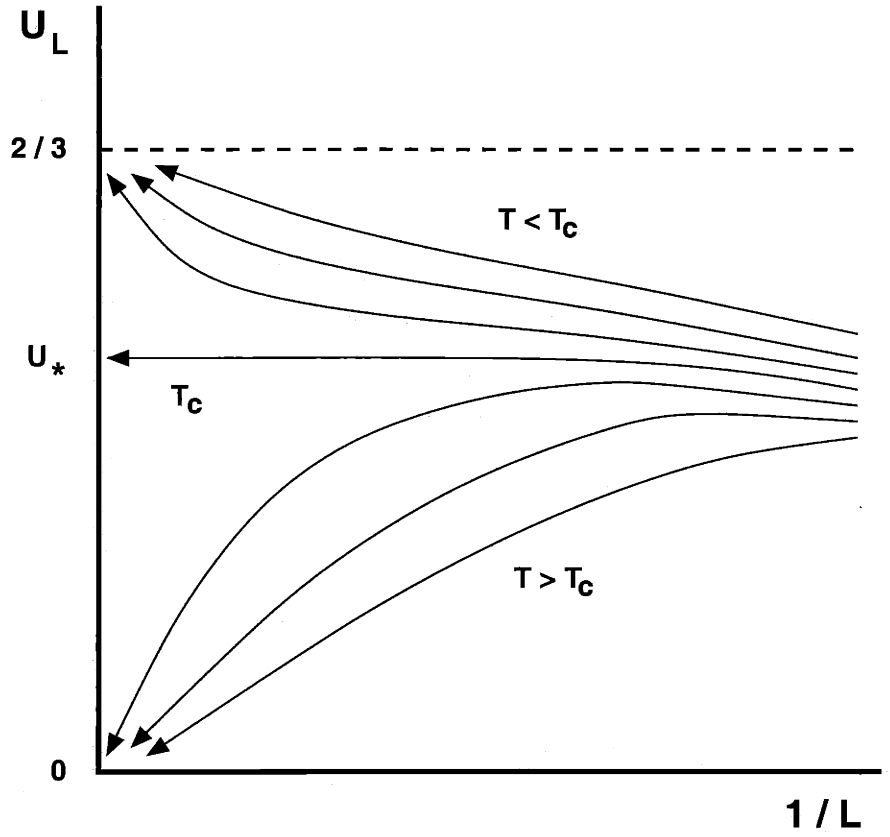

Figure 7-12: *The expected flow of U_L as a function of $1/L$. On each curve the temperature is constant.*

possible to calculate the curve in figure 7-11 analytically from the exact solution of the Ising model on finite lattices. However, the analytical expressions for the correlation functions found in the literature are quite complicated.

We also measure U_L, the Binder cumulant in volumes of extent L. In figure 7-12, the expected behavior of U_L as L increases for different temperatures is plotted. For $T > T_c$, the chiral symmetry is intact and U_L flows into the $T = \infty$ fixed point $U = 0$. For $T < T_c$, the chiral symmetry is spontaneously broken and U_L flows into the $T = 0$ fixed point $U = 2/3$. If the universality class has a non-trivial fixed point $U = U_*$, then U_L flows into this value at $T = T_c$. By measuring U_L in various volumes at many different temperatures, we determine this flow numerically. We have measured the

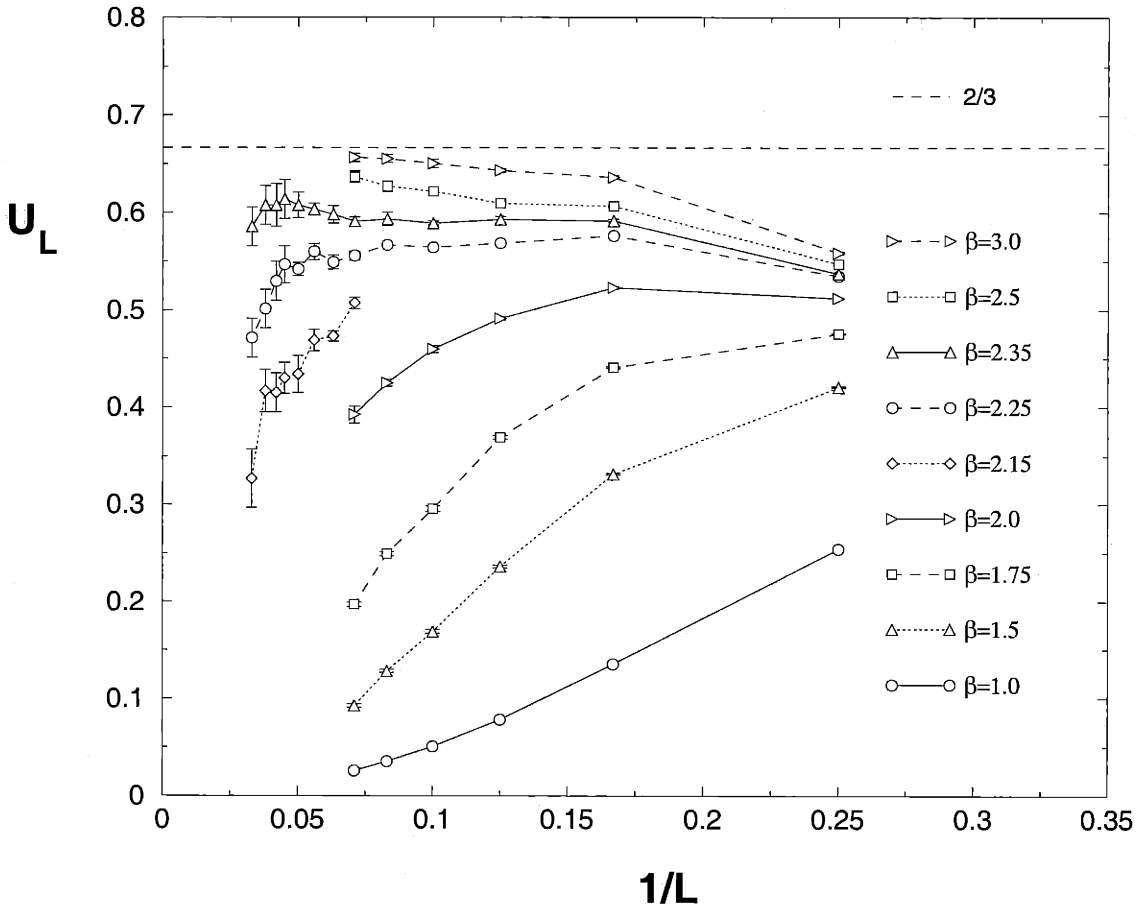

Figure 7-13: *Measured values of U_L plotted versus $1/L$ for various β in volumes with 40 time slices. Near $\beta = 2.35$, the values appear to flow into the non-trivial fixed point $U_* = 0.60(1)$.*

Binder cumulant values in volumes up to $L = 30$ and we plot some of these values as a function of $1/L$ in figure 7-13. These measurements are made with the number of time slices fixed at 40. Each curve in the figure represents some fixed temperature. In figure 7-13, for small β (i.e. high temperatures), U_L clearly flows into the infinite temperature fixed point $U = 0$, while for β large (low temperatures), U_L flows into the zero temperature fixed point $U = 2/3$. For β close to β_c, we have to go to larger volumes to see this behavior. Near $\beta = 2.35$, the cumulant values appear to flow into a non-trivial fixed point U_*. Examining this region closely, we estimate the

critical inverse temperature as $\beta_c = 2.36(2)$ and the fixed point value $U_* = 0.60(1)$. The finite-size scaling fit of χ measured at this $\epsilon \approx 0.24$ gives the same value of β_c. Note that this deviates slightly from the critical temperature measured at $\epsilon = 0.1$. The universal fixed point value for the 2-d Ising model is estimated as $U_* \sim 0.58$ [97]. This is further evidence that the chiral phase transition belongs to the 2-d Ising universality class.

Chapter 8

Summary and conclusions

Potts model for dense QCD

A cluster algorithm was used to solve the notorious complex action problem in the Potts model approximation to QCD with heavy quarks at large chemical potential. We use a simple analytically constructed improved estimator that gives an exponential reduction in the required statistics. Since the improved estimator is real and positive, importance sampling techniques that fail for complex actions then become applicable. This makes it possible to study the whole $h > 0$ parameter range of the Potts model, not just the $h = 0$ axis. (Recall that h corresponds to $\exp(\beta(\mu - M))$ in QCD in the limit $M, \mu \to \infty$ at any given $\mu - M$).

The cluster algorithm was compared with a flux model reformulation, and with the reweighted Monte Carlo algorithm. It was found that the cluster algorithm was more efficient than using the flux model reformulation. In the large volume limit the cluster algorithm will always be superior to Monte Carlo reweighting. However, at very small h it is sufficient to use reweighting techniques to obtain physically relevant results. This turned out to be the case for the endpoint of the first order line, which occurs at a very small h because the 3-d 3-state Potts model phase transition is rather weak at $h = 0$. We therefore used reweighted Monte Carlo to locate the first-order

line and its endpoint. However, one should emphasize that as computer power rises, and the maximum attainable volume becomes bigger, the meron-cluster algorithm will eventually become superior at any $h > 0$. We confirm that the critical endpoint is in the 3-d Ising universality class.

We also calculated quark-quark, quark-antiquark, and antiquark-antiquark potentials, in the confined and deconfined regions of the phase diagram. We found the expected behavior: the background density of heavy quarks screens color fields, so that all potentials reach plateaux at long distances, whose values are simply related to the free energies of external static quarks and antiquarks.

Chiral phase transition with staggered fermions

We have applied a new fermion simulation technique — the meron-cluster algorithm — to a model of staggered fermions. In contrast to standard methods which integrate out the fermions and are left with a non-local bosonic action, we describe the fermions in a Fock state occupation number basis and thus keep a local bosonic action. The fermion permutation sign arises due to the Pauli exclusion principle as a non-local factor associated with non-trivial topology of the fermion world-lines. The sign leads to severe cancellations which makes standard simulation techniques impossible to use. The decomposition of a configuration into clusters allows us to disentangle the complicated topology of the fermion world-lines. In particular, a meron-cluster identifies a pair of configurations with equal weight and opposite sign. This results in an explicit cancellation of two contributions ± 1 to the path integral, such that only the zero-meron sector contributes to the partition function. Observables like the chiral susceptibility χ receive contributions only from the zero- and two-meron sectors. To measure χ one can hence eliminate all sectors with more than two merons, which leads to an exponential gain in statistics and to a complete solution of the fermion sign problem.

The meron-cluster algorithm allowed us to simulate a staggered fermion model for which standard fermion methods suffer from a severe sign problem. The model has two flavors and a $\mathbf{Z}(2)$ chiral symmetry which is spontaneously broken at low temperatures. Applying finite-size scaling methods to the high-precision numerical data for the chiral susceptibility, we extracted critical exponents compatible with those of the 3-d Ising model. This is the expected behavior based on universality arguments and dimensional reduction. We also applied our method to $(2+1)$ dimensions. The $N = 4$ flavor case was studied in [34] and it was verified that the model is in the 2-d Ising universality class. The standard fermion algorithm that was used in that study does not work for $N < 4$ due to the fermion sign problem. The meron-cluster algorithm solves the sign problem and we were able to simulate the $N = 1$ case and we verified that it belongs to the 2-d Ising universality class, too.

One should keep in mind that the meron-cluster algorithm is not always applicable. For example, the meron concept applies only when the clusters are independent in their effect on the fermion sign. In addition, it must always be possible to flip the clusters such that one reaches a reference configuration with a positive sign. Otherwise, some contributions from the zero-meron sector could be negative. For example, in our model these restrictions led to $G \geq 1$, i.e. to a sufficiently strong four-fermion coupling.

Outlook

The algorithms that we have developed for the Potts model and for the staggered fermion model belong to the class of meron-cluster algorithms that has recently been used to solve a large variety of sign and complex action problems. Of course, the ultimate goal is to construct a similar algorithm for QCD at non-zero chemical potential and investigate the phase structure of QCD at $\mu \neq 0$ from first principles. The complex action problem in full QCD is more complicated than the one in the

two toy models considered in this thesis. So far, meron-cluster algorithms have led to solutions of fermion sign problems as well as complex action problems in bosonic theories, but have not yet solved complex action problems in theories with fermions. This may ultimately become possible when one uses the D-theory formulation of QCD [16, 17, 18].

Bibliography

[1] P. M. Zerwas and H. A. Kastrup, "QCD - 20 years later. Proceedings, Workshop, Aachen, Germany, June 9-13, 1992. Vol. 1, 2," *Singapore: World Scientific (1993).*

[2] K. G. Wilson, Phys. Rev. D **10** (1974) 2445.

[3] G. S. Bali and K. Schilling, Phys. Rev. D **46** (1992) 2636.

[4] G. S. Bali, K. Schilling, A. Hulsebos, A. C. Irving, C. Michael and P. W. Stephenson [UKQCD Collaboration], Phys. Lett. **B309** (1993) 378.

[5] F. Karsch, Nucl. Phys. Proc. Suppl. **83** (2000) 14.

[6] S. Aoki *et al.* [CP-PACS Collaboration], Phys. Rev. Lett. **84** (2000) 238.

[7] S. Hashimoto, Nucl. Phys. Proc. Suppl. **83** (2000) 3.

[8] A. Di Giacomo, B. Lucini, L. Montesi and G. Paffuti, Nucl. Phys. Proc. Suppl. **74** (1999) 405.

[9] J. W. Negele, Nucl. Phys. Proc. Suppl. **73** (1999) 92.

[10] I. M. Barbour, S. E. Morrison, E. G. Klepfish, J. B. Kogut and M. Lombardo, Nucl. Phys. Proc. Suppl. **60A** (1998) 220.

[11] M. Alford, A. Kapustin and F. Wilczek, Phys. Rev. D **59** (1999) 054502.

[12] S. R. White et al., Phys. Rev. **40** (1989) 506.

[13] E. Dagotto et al., Phys. Rev. **B41** (1990) 811.

[14] W. Bietenholz, A. Pochinsky and U.-J. Wiese, Phys. Rev. Lett. **75** (1995) 4524.

[15] S. Chandrasekharan and U.-J. Wiese, Nucl. Phys. **B492** (1997) 455.

[16] B. B. Beard, R. C. Brower, S. Chandrasekharan, D. Chen, A. Tsapalis and U.-J. Wiese, Nucl. Phys. Proc. Suppl. **63** (1998) 775.

[17] U.-J. Wiese, Nucl. Phys. Proc. Suppl. **73** (1999) 146.

[18] R. Brower, S. Chandrasekharan and U.-J. Wiese, Phys. Rev. D **60** (1999) 094502.

[19] J. Cox, C. Gattringer, K. Holland, B. Scarlet and U.-J. Wiese, Nucl. Phys. Proc. Suppl. **83** (2000) 777.

[20] S. Chandrasekharan and U.-J. Wiese, Phys. Rev. Lett. **83** (1999) 3116.

[21] S. Chandrasekharan, Nucl. Phys. Proc. Suppl. **83** (2000) 774.

[22] S. Chandrasekharan, J. Cox, K. Holland and U.-J. Wiese, Nucl. Phys. **B576** (2000) 481.

[23] J. Cox and K. Holland, Nucl. Phys. **B583** (2000) 331.

[24] S. Chandrasekharan and J. C. Osborn, Phys. Lett. **B496** (2000) 122.

[25] J. C. Osborn, hep-lat/0010097.

[26] S. Chandrasekharan, B. Scarlet and U.-J. Wiese, cond-mat/9909451.

[27] S. Chandrasekharan and J. C. Osborn, Springer Proc. Phys. **86** (2000) 28.

[28] S. Chandrasekharan, hep-lat/0011022.

[29] T. C. Blum, J. E. Hetrick and D. Toussaint, Phys. Rev. Lett. **76** (1996) 1019.

[30] J. Engels, O. Kaczmarek, F. Karsch and E. Laermann, Nucl. Phys. **B558** (1999) 307; Nucl. Phys. Proc. Suppl. **83** (2000) 369.

[31] P. Hasenfratz, F. Karsch and I.O. Stamatescu, Phys. Lett. **133B** (1983) 221

[32] T. A. DeGrand and C. E. DeTar Nucl. Phys. **B225** (1983) 590.

[33] J. B. Kogut, M. A. Stephanov and C. G. Strouthos, Phys. Rev. D **58** (1998) 096001.

[34] J. B. Kogut and C. G. Strouthos, Phys. Rev. D **63** (2001) 054502.

[35] M. Alford, S. Chandrasekharan, J. Cox and U.-J. Wiese, hep-lat/0101012, to be published in Nucl. Phys. B.

[36] M. Crawford and D. N. Schramm, Nature **298** (1982) 538.

[37] E. Witten, Phys. Rev. D **30** (1984) 272.

[38] N. K. Glendenning and F. Weber, astro-ph/0003426.

[39] D. Blaschke, H. Grigorian and G. Poghosian, astro-ph/0008005.

[40] S. A. Bass, M. Gyulassy, H. Stocker and W. Greiner, J. Phys. G**G25** (1999) R1.

[41] J. I. Kapusta, "Finite Temperature Field Theory," *Cambridge Univ. Pr. (1989) (Cambridge monographs on mathematical physics).*

[42] L. D. Faddeev and V. N. Popov, Phys. Lett. **B25** (1967) 29.

[43] K. Rajagopal and F. Wilczek, hep-ph/0011333.

[44] F. R. Brown *et al.*, Phys. Rev. Lett. **65** (1990) 2491.

[45] R. D. Pisarski and F. Wilczek, Phys. Rev. D **29** (1984) 338.

[46] B. Svetitsky and L. G. Yaffe, Nucl. Phys. B **210** (1982) 423.

[47] J. Kogut, M. Stone, H. W. Wyld, J. Shigemitsu, S. H. Shenker and D. K. Sinclair, Phys. Rev. Lett. **48** (1982) 1140.

[48] J. Kogut, M. Stone, H. W. Wyld, W. R. Gibbs, J. Shigemitsu, S. H. Shenker and D. K. Sinclair, Phys. Rev. Lett. **50** (1983) 393.

[49] J. Kogut, H. Matsuoka, M. Stone, H. W. Wyld, S. Shenker, J. Shigemitsu and D. K. Sinclair, Phys. Rev. Lett. **51** (1983) 869.

[50] F. Wilczek, Int. J. Mod. Phys. **A7** (1992) 3911.

[51] K. Rajagopal and F. Wilczek, Nucl. Phys. **B399** (1993) 395.

[52] J. Berges and K. Rajagopal, Nucl. Phys. **B538** (1999) 215.

[53] B. C. Barrois, Nucl. Phys. **B129** (1977) 390.

[54] D. Bailin and A. Love, Phys. Rept. **107** (1984) 325.

[55] M. Alford, K. Rajagopal and F. Wilczek, Phys. Lett. **B422** (1998) 247.

[56] R. Rapp, T. Schafer, E. V. Shuryak and M. Velkovsky, Phys. Rev. Lett. **81** (1998) 53.

[57] E. Laermann, Nucl. Phys. Proc. Suppl. **63** (1998) 114.

[58] A. Ukawa, Nucl. Phys. Proc. Suppl. **53** (1997) 106.

[59] A. Ali Khan *et al.* [CP-PACS Collaboration], Phys. Rev. D **63** (2001) 034502.

[60] M. Alford, K. Rajagopal and F. Wilczek, Nucl. Phys. **B537** (1999) 443.

[61] M. Creutz, "Quarks, Gluons And Lattices," *Cambridge Univ. Pr. (1983) (Cambridge Monographs On Mathematical Physics).*

[62] H. J. Rothe, "Lattice gauge theories: An Introduction," *Singapore: World Scientific (1992).*

[63] I. Montvay and G. Münster, "Quantum fields on a lattice," *Cambridge Univ. Pr. (1994) (Cambridge monographs on mathematical physics).*

[64] K. Symanzik, Nucl. Phys. **B226** (1983) 187, 205.

[65] M. Lüscher and P. Weisz, Commun. Math. Phys. **97** (1985) 59.

[66] P. Hasenfratz and F. Niedermayer, Nucl. Phys. **B414** (1994) 785.

[67] W. Bietenholz and U.-J. Wiese, Nucl. Phys. **B464** (1996) 319.

[68] A. Chodos and J. B. Healy, Nucl. Phys. **B127** (1977) 426.

[69] K. G. Wilson, "Quarks And Strings On A Lattice," *New Phenomena In Subnuclear Physics, ed. A. Zichichi, Plenum Press, New York, 1977, p. 69.*

[70] J. Kogut and L. Susskind, Phys. Rev. D **11** (1975) 395.

[71] T. Banks, L. Susskind and J. Kogut, Phys. Rev. D **13** (1976) 1043.

[72] L. Susskind, Phys. Rev. D **16** (1977) 3031.

[73] M. Creutz, hep-lat/0007032.

[74] A. Kocic and J. Kogut, Phys. Rev. Lett. **74** (1995) 3109.

[75] A. Kocic and J. Kogut, Nucl. Phys. B **455** (1995) 229 [hep-lat/9507012].

[76] J. Condella and C. E. DeTar, Phys. Rev. D **61** (2000) 074023.

[77] F. Karsch and S. Stickan, Phys. Lett. **B488** (2000) 319.

[78] E. Hilf and L. Polley, Phys. Lett. **B131** (1983) 412.

[79] R. H. Swendsen and J. Wang, Phys. Rev. Lett. **58** (1987) 86.

[80] K. Rummukainen, Nucl. Phys. **B390** (1993) 621.

[81] B. A. Berg and T. Neuhaus, Phys. Lett. **B267** (1991) 249; Phys. Rev. Lett. **68** (1992) 9.

[82] W. Janke and R. Villanova, Nucl. Phys. **B489** (1997) 679.

[83] R. V. Gavai, F. Karsch and B. Petersson, Nucl. Phys. **B322** (1989) 738.

[84] A. M. Ferrenberg and R. H. Swendsen, Phys. Rev. Lett. **61** (1988) 2635; Phys. Rev. Lett. **63** (1989) 1195.

[85] H. W. J. Blöte, E. Luijten and J. R. Heringa, J. Phys. A: Math. Gen. **28** (1995) 6289

[86] P. Jordan and E. Wigner, Z. Phys. **47** (1928) 631.

[87] U.-J. Wiese and H.-P. Ying, Phys. Lett. **A168** (1992) 143.

[88] H. G. Evertz, G. Lana and M. Marcu, Phys. Rev. Lett. **70** (1993) 875.

[89] H. G. Evertz, The loop algorithm, in Numerical Methods for Lattice Quantum Many-Body Problems, ed. D. J. Scalapino, Addison-Wesley Longman, Frontiers in Physics

[90] U.-J. Wiese, Phys. Lett. **B311** (1993) 235.

[91] B. B. Beard and U.-J. Wiese, Phys. Rev. Lett. **77** (1996) 5130.

[92] U.-J. Wiese and H.-P. Ying, Z. Phys. **B93** (1994) 147.

[93] J. Hubbard, Proc. Roy. Soc. **A276** (1963) 238.

[94] J. Kanamori, Proc. Theor. Phys. **30** (1963) 275.

[95] M. C. Gutzwiller, Phys. Rev. Lett. **10** (1963) 159.

[96] D. J. Scalapino, Phys. Rep. **250** (1995) 329.

[97] K. Binder, Phys. Rev. Lett. **47** (1981) 693.

Index